Geodynamic Modeling of Mars Constrained by InSight

Josh P. Murphy

Dissertation submitted to the Faculty of the
Virginia Polytechnic Institute and State University
in partial fulfillment of the requirements for the degree of

Doctor of Philosophy
in
Geosciences

Scott D. King, Chair
Mark Caddick
D. Sarah Stamps
Robert Weiss

August 10, 2023
Blacksburg, Virginia

Keywords: Mars, mantle convection, volcanism, numerical modeling

Geodynamic Modeling of Mars Constrained by InSight

Josh P. Murphy

(ABSTRACT)

Through geodynamic modeling, I investigate how Mars could have produced the extensive volcanism required to form the Tharsis rise early in its history, as well as continue to produce small amounts of melt up to present-day, in order to account for the evidence of limited geologically recent volcanism. InSight is the first interplanetary mission dedicated primarily to the study of a planet's deep interior, and has provided useful constraints for the present structure and interior temperature of Mars. I use the results from InSight and other spacecraft missions to more accurately model Mars, and evaluate the results of my geodynamic models, so as to constrain the properties that are necessary for or consistent with both the InSight results and the volcanic history reflected on the surface. This modeling has required extensive modification to the CitcomS geodynamic code I use, the bulk of that effort being in implementing and testing the melting calculations. One of the useful constraints that would have been provided by InSight would have been ground truthing the heat flow from the interior at the landing site, and this required determining, among other quantities, the thermal conductivity of the regolith into which the heat flow probe (mole) was placed. While the mole could not penetrate to its designed depth, thus disallowing the complete heat flow measurement, the team were able to obtain the necessary data determine the thermal conductivity, and how it varies seasonally. My rapid analytical method of estimating thermal conductivity produces results that agree surprisingly well with those of the team's complex numerical model, despite the mole not meeting the assumption of a sufficiently high length to width ratio.

Geodynamic Modeling of Mars Constrained by InSight

Josh P. Murphy

(GENERAL AUDIENCE ABSTRACT)

I investigate how Mars could have produced the extensive volcanism required to form the Tharsis rise early in its history, as well as continue to produce small amounts of melt up to present-day, in order to account for the evidence of limited geologically recent volcanism. I use 3D computer models of the mantle–the solid, but slowly flowing layer that makes up the bulk of rocky planets like Earth and Mars. InSight is the first interplanetary mission dedicated to the study of a planet's deep interior, and has provided useful constraints for the present structure and interior temperature of Mars. I use the results from InSight and other spacecraft missions to more accurately model Mars, and evaluate the results of my models, so as to constrain the properties that are necessary for or consistent with both the InSight results and the volcanic history reflected on the surface. This modeling has required extensive modification to the modeling code I use, the bulk of that effort being in implementing and testing the melting calculations. One of the useful constraints that would have been provided by InSight would have been ground truthing the heat flow from the interior at the landing site, and this required determining, among other quantities, the thermal conductivity of the soil into which the heat flow probe (mole) was placed. While the mole could not penetrate to its designed depth, thus disallowing the complete heat flow measurement, the team were able to obtain the necessary data determine the thermal conductivity, and how it varies seasonally. My rapid analytical method of estimating thermal conductivity produces results that agree surprisingly well with those of the team's complex numerical model, despite the mole not meeting the assumption of a sufficiently high length to width ratio.

Dedication

To my parents, for all the love, support, and sacrifices that have enabled me to pursue my education.

Contents

List of Figures viii

List of Tables xiv

1 Introduction 1

1.1 Mars . . . 1

1.1.1 Structure and composition . . . 2

1.1.2 Major surface features and volcanic history . . . 4

1.2 Geodynamic Modeling . . . 6

1.2.1 History of geodynamic modeling . . . 7

1.2.2 Melting . . . 9

1.3 Outline of Chapters . . . 11

2 Analytic Solution to Thermal Conductivity for Mars InSight HP3 15

2.1 Introduction . . . 15

2.2 Methods . . . 17

2.3 Results and Discussion . . . 21

2.4 Conclusions . . . 23

3 Mars Mantle Convection **29**

3.1 Introduction . . . 29

3.2 Methods . . . 34

3.2.1 Melt production . . . 36

3.2.2 Model cases . . . 38

3.3 Results . . . 40

3.3.1 Mantle temperature and geotherms . . . 41

3.3.2 Geoids . . . 43

3.3.3 3D Mantle Structure Evolution . . . 43

3.3.4 Melting . . . 44

3.4 Discussion . . . 46

3.4.1 Effects of adding the dichotomy . . . 50

3.5 Conclusions . . . 51

4 The Mantle Melting Algorithm **60**

4.1 Introduction . . . 60

4.2 Melt Fraction . . . 62

4.3 Melt Production . . . 66

4.4 Latent Heat . . . 69

4.5 Extended Boussinesq Approximation Models . . . 73

4.5.1 Methods 73

4.5.2 Preliminary Results 75

4.5.3 Discussion and Initial Conclusions 75

5 Looking Forward **80**

Appendix A A More Realistic Dichotomy **84**

Bibliography **87**

List of Figures

1.1 Scaled comparison of the interior structures of Earth and Mars. In this schematic, Earth's crustal thickness is generalized to that of its oceanic crust, as this covers the majority of the planet and is more analogous to Mars' basaltic crust. 14

1.2 Topographic map of Mars, showing the dichotomy boundary (dashed where uncertain), the Tharsis and Elysium rises, Cerberus Fossae, and the InSight landing site. 14

2.1 (a) Final position of the mole, as imaged on Sol 775, buried in the backfilled pit with just the back cap exposed $\sim$ 3 cm below the surrounding surface. Credit: NASA/JPL-Caltech (`https://mars.nasa.gov/raw_images/890722/`). (b) Schematic of mole tilt and position within the layers of the regolith. Modified from Grott et al. [26]. 24

2.2 Self heating curves for all six TEM-A experiments for Grott et al. [26], plotted with a log scale for time to show the linear trend. The bold parts of the lines are the window with the highest R^2, as used to obtain the values of thermal conductivity reported in Table 2.1. 25

2.3 Seasonal variation in regolith thermal conductivity (K) due to atmospheric pressure changes, as measured at the InSight landing site. My K values corresponding to the highest R^2 values, as reported in the supplement to Grott et al. [26], are in black. The numerical results of Grott et al. [26] with their 1-σ error bars are plotted in red. Plot (a) shows the mean K (solid blue line) across the range of window start times and lengths tested, with 1-σ error bars. Plot (b) is identical, except the mean is replaced by the median k value (dashed blue line), with the error bars extending between the 15.9 and 84.1 percentiles. This would correspond to 1-σ if the regression-determined K values for a given sol were normally distributed–which they are not (c.f. the histograms in Figure 2.5). 26

2.4 Shaded contour plots of the R^2 values greater than 0.99980, as a function of regression window length vs. start time, for each of the six active heating experiments. The points corresponding with the maximum R^2 are marked with a star. These plots indicate a very good linear fit across a wide range of those two parameters, not just where R^2 is greatest. 27

2.5 Histograms of the thermal conductivity value calculated from the regression slope, when varying the window length from 10 to 180 time steps (approximately 14–259 minutes) and varying the window start time after the beginning of active heating from 10 to 250 time steps (approximately 14–360 minutes). The R^2_{max} is the thermal conductivity value I reported in Grott et al. [26]. Also shown are the mean, median, and mode values of R, as well as the mean ±1 standard deviations. The shaded range, with vertical dotted red lines at either end, shows the region between the 15.1 and 84.9 percentiles, which would correspond to mean ±1 standard deviation if the thermal conductivities were normally distributed. 28

3.1 Crustal thickness map adapted from Zuber et al. [111]. The locations and approximate extent of Tharsis and Elysium are marked. The red line marks the dichotomy boundary. The line is dashed where the boundary is uncertain, in particular beneath Tharsis. 53

3.2 Comparison of the Katz et al. [38] solidus for dry peridotite with the Mars solidus of Duncan et al. [21] over the applicable depth range of Katz et al. [38]. The liquidus of Katz et al. [38] is also plotted. Melting in our models is confined to a narrow range of pressures between 2.6 and 4 GPa, or approximately 200–300 km depth. 54

3.3 a-c: Present-day geotherms, including the InSight derived mid-mantle temperature estimate of 1605 ± 100 K by Huang et al. [34] (vertical magenta lines), as well as the range of possible geotherms from Smrekar et al. [81] (shaded). 55

3.4 Geoid power spectra compared to Mars without Tharsis coefficients from Zuber and Smith (1997). Begins at l=2. 56

3.5 3D plots of selected model cases with potential temperature (yellow) and melt (red) isosurfaces for all three (reference n=3, reference n=1, and dichotomy n=1) cases with 10x enrichment and initial T_{CMB} of 1.1 ΔT = 1870 K. The isotherms and melt fractions plotted for each case are: (a) T = 1650 K, melt fraction = 10%; (b) T = 1770 K, melt fraction = 25%; (c) T = 1755 K, melt fraction = 25%; (d) T = 1500 K, melt fraction = 0.01%; (e) T = 1710 K, melt fraction = 0.1%; (f) T = 1710 K, melt fraction = 1%; (g) T = 1380 K, no melt present; (h) T = 1680 K, melt fraction = 0.01%; and (i) T = 1680 K, melt fraction = 1%. The southern hemisphere, with the initially thicker lithosphere, is darker in all dichotomy plots (c, f, i). For the remaining plots, north is approximately up, but some rotation has been done to better show the thermal structure and melt. 57

3.6 Melt and melt production over time. The bulk melt fraction is the fraction of the total mantle (out of 1.0) that is molten at a given time. This is shown here both on a linear and logarithmic scale. Cumulative melt is the integral of the mantle melt production rate over time. On the cumulative melt plots (g–i), approximate amount of melt (1–33 $\times 10^8$ km^3) required to produce Tharsis is shaded in lighter gray. However, only a fraction of the melt (here assumed to be 10%) produced in the mantle is extracted to and erupted on the surface. The darker gray shading on these same plots is the required melt volume multiplied by ten (1–3 $\times 10^9$ km^3) to account for this. 58

3.7 Color-coded summary of all 27 model cases and whether each one meet our constraints for geotherms, melt, and the geoid. Red indicates the constraint is not met. Blue indicates the constraint is met: geotherm consistent with Huang et al. [34]; melt at present-day; sufficient cumulative melt production to produce Tharsis (accounting for 10% melt extraction); or a geoid that agrees with the "Mars without Tharsis" geoid of Zuber and Smith [110]. Purple indicates an intermediate result: no melt at present, but within the past 200 Myr; sufficient melt for Tharsis allowing >10% melt extraction; or a geoid that either agrees with Zuber and Smith [110] only in the lowest degrees ($l \leq 6$) or falls between the red and blue geoids. 59

4.1 Comparison of the Katz et al. [38] dry solidus with the Duncan et al. [21] solidus, which are both parameterized with respect to pressure (in GPa). Approximate corresponding depths and the Katz et al. [38] liquidus are also included. 78

4.2 Comparisons of temperature and cumulative melt production, varying the disputation number (Di), for the Boussinesq approximation (Di=0.0) and extended Boussinesq approximation (EBA) models. The plots in the left column are for a constant non-dimensional radiogenic heating of Q=25 ($4.09 \times 10^{-12}\,\mathrm{J\,kg^{-1}}$), which is close to the present-day value. The plots in the right column use the decaying heating based on the back-projected Dreibus and Wanke [20] composition, the same as the models in Chapter 3: initial Q=144 ($2.36 \times 10^{-11}\,\mathrm{J\,kg^{-1}}$). 240 km depth is near the middle of the melting depth range (e.g., Figure 4.1). For the decaying, higher radiogenic heating models, varying Di has a negligible effect on temperature and melt, and the four curves are indistinct. 79

A.1 Schematic based on the one in Banerdt [6]), where ρ_c is crustal density, δc is the isostatic root thickness, w is the downward displacement due to flexure, C is the uniform crustal plate thickness, ρ_m is mantle density, $\delta\rho$ is the mantle density anomaly, M is the thickness of mantle density anomaly, H is the surface topography, and L is the elastic lithosphere thickness. H, w, $\delta\rho$ and δc are represented by spherical harmonic coefficients, so they can vary across the planet. 86

A.2 Pre-Tharsis dichotomy to spherical harmonic degree 40, using the method of Andrews-Hanna et al. [4] and Banerdt [6]. Tharsis would be centered around 100°W near the equator. The northward extension of the southern highlands east of Tharsis, around 60°W, is Tempe Terra. The large "hole" in the southern highlands in the lower left (75°E, 45°S) is associated with the Hellas basin, and the smaller one in the lower right (40°W, 50°S) is the Argyre basin. Both of these are large and ancient impact basins. 86

List of Tables

2.1 Regolith thermal conductivity at the InSight landing site as measured at different sols (Mars days), with their corresponding solar longitude (indicating time of year) L_s. The analytical thermal conductivity (K) is my value determined by the regression slope of the mole self-heating curve over the time window with the highest R^2 (see text). The numerical K values are those reported in the main text of Grott et al. [26], as determined from the self-heating curve using numerical models. 22

3.1 Summary of parameters and initial conditions used in our models. 35

3.2 Model time and age of last melt production. The reference cases are taken to start at 4.5 Ga, while Dichotomy cases are taken start 400 Myr later, at 4.1 Ga. 47

4.1 Summary of melt fraction parameterization parameters. See text for explanation of their use. The solidus parameters A_1, A_2, and A_3 are for the portion of the Duncan et al. [21] solidus up to 10 GPa. All other values are those of Katz et al. [38] for dry peridotite. Note that the A_1, B_1, and C_1 terms have been converted from °C in their respective publications to kelvins, in order to remain consistent with my use of absolute temperature for melting. 64

List of Abbreviations

CMB Core Mantle Boundary

cpx Clinopyroxene

EBA Extended Boussinesq Approximation

HP3 Heat Flow and Physical Properties Package

HPE Heat Producing Elements

opx Orthopyroxene

SEIS Seismic Experiment for Interior Structure

TEM-A Thermal Excitation and Measurement–Active

TEM-P Thermal Excitation and Measurement–Passive

Chapter 1

Introduction

1.1 Mars

Among the seven other planets in our solar system, Mars has received the greatest attention. Mercury is extremely difficult to reach, and while possessing a tantalizing intrinsic magnetic field, it is small and devoid of current tectonic or volcanic activity. Venus, while closest in size, mass, and distance from the Sun–and arguably in geodynamic history–to Earth, is eternally shrouded by opaque clouds within a crushing atmosphere hot enough at the surface to melt lead. Mars is little farther than Venus, and while by all appearance devoid of extant life and liquid water, Mars bears abundant evidence of a wetter and more dynamic past.

The geologic history of Mars is divided into four periods: the pre-Noachian (up to 4.1 Ga), Noachian (4.1–3.7 Ga), Hesperian (3.7–3.0 Ga), and the Amazonian (3.0 Ga–present) [14]. These and all other ages provided for events and features on Mars are merely approximate and will vary between sources, as they are derived from crater counting, with cratering rates as determined from radiometric dating of returned lunar samples extrapolated from the Moon to Mars. The Noachian, and to a lesser extent the Hesperian, were the times of relatively abundant liquid surface water and hydrous weathering [14]. This time period, and extending into the early Amazonian, was also a time of greater, more widespread volcanic activity [14]. Smaller volumes of more localized volcanism have occurred sporadically through the later Amazonian, including within the past 10-100 Ma [69, 74], and possibly as recently as the

past 2.4 Ma [63]. Therefore, Mars is still potentially volcanically active in the longer term. In addition, InSight has detected limited, ongoing seismic activity, especially in the Cerberus Fossae region, and this seismic activity may be linked to geologically recent volcanic activity in that region [12, 44, 68, 87].

1.1.1 Structure and composition

Broadly similar to Earth, Mars is a terrestrial planet comprised of an iron-rich metallic core surrounded by a mantle and crust composed of silicate rock (Figure 1.1). Various spectroscopic methods by orbiters, landers, and rovers have enabled us to characterize the surface material. Dreibus and Wanke [20] and Bertka and Fei [8] infer the composition and mineralogy of the Martian mantle from that of meteorites recovered on Earth, themselves ejected from Mars by impacts, and found the Martian mantle to be more iron-rich than Earth's mantle. (Dreibus and Wanke [20] find the Martian mantle to be 17.90 weight percent iron, as compared to 8.10% for Earth [92].) This SNC group of Mars meteorites (so named for the three classes of shergottites, nakhlites and chassignites) was determined to originate from Mars because the noble gas isotopic composition of inclusions within them matched measurements of Mars' atmosphere by the Viking landers [10, 96].

The radius of Mars is roughly half that of Earth (6,371 km), or 3389.5 km on average. Before InSight, the size of the core and thickness of the crust, and so the thickness of the mantle, were poorly constrained. By combining records of seismic reflections off the core-mantle boundary (CMB) collected by InSight with geodetic data from orbiting spacecraft, Stähler et al. [86] constrained the radius of the Martian core to be 1830 $\pm$ 40 km, with a mean density of 5700–6300 $\mathrm{kg\,m^{-3}}$. With additional data and modeling, Irving et al. [35] favor a slightly smaller and denser core (1780–1810 km in radius and 6200–6300 $\mathrm{kg\,m^{-3}}$). (See

Figure 1.1.) Both of these overlapping ranges put the core at the large, low-density end of the pre-mission estimate [81], and consequently the core must have a relatively high light element (e.g., sulfur, oxygen, hydrogen, and carbon) concentration of 20–22%, including a near-eutectic (∼10–15%) sulfur content [35, 86]. Stähler et al. [86] and Irving et al. [35] also find no evidence of a solid inner core, which is consistent with the low solidus of the near-eutectic iron-sulfur composition. The absence of a present-day core dynamo, which is estimated to have shut off ∼3.7 Ga [59]–indicative of a low heat flux of <5–19 $\mathrm{mW\,m^{-2}}$ from the core into the mantle since it shut off [65]–combined with the confirmation of a fully molten core, further constrain models of the interior evolution of Mars.

In addition to the core size and composition, InSight has also provided new information on mantle temperatures and the structure of the mantle and crust. The large size of the core precludes the existence of a bottom layer of bridgmanite (which comprises Earth's lower mantle, below 660 km depth to the D" layer near the CMB) in the mantle (Figure 1.1). Huang et al. [34] do find evidence of a mid-mantle seismic discontinuity at 1006 ± 40 km depth, which they interpret as the transition of olivine to a higher-pressure polymorph, most likely ringwoodite. Between this depth and that of the CMB (∼1550-1600 km) therefore corresponds to a truncated version of Earth's transition zone. From the depth of the 1006 ± 40 km phase transition, Huang et al. [34] infer a mantle potential temperature of 1605 ± 100 K, and thus a sluggish mantle with a viscosity of 10^{20}–10^{22} Pa s. This is very much on the cooler side of the range of pre-mission estimates modeled by Smrekar et al. [81]; 1605 K is close to their minimum temperature at that depth, and 1705 K is still below their mean temperature. At the InSight landing site, the thermal lithosphere is ∼400-600 km thick [40]. This is much thicker than Earth's lithosphere, although similar to Earth, Khan et al. [40] identify a structure consistent with a low-velocity zone beneath the Martian lithosphere. The local Moho corresponds with one of two seismic interfaces, either the one at 20 ± 5 km

or the one at 39 ± 8 km depth [49]. Combining this new information with global gravity and shape measurements, the mean crustal thickness is therefore estimated to be between 24 and 72 km [49].

1.1.2 Major surface features and volcanic history

Zooming out and looking at the global topography of Mars, the largest scale feature is the hemispheric dichotomy between the lowlands dominating the northern hemisphere and highlands dominating the southern hemisphere (Figure 1.2). This is also referred to as the crustal dichotomy, and the topographic dichotomy boundary approximately follows the boundary between thicker southern crust and thinner northern crust [63, 111]. The origin of the dichotomy, likely in the pre-Noachian [14] period, remains somewhat unclear. It may be of internal origin, as a result of spherical harmonic degree-1 pattern of mantle convection, as associated with a single large plume [76, 77, 106], or the overturn of a magma ocean [22, 77]. Degree-1 convection means that one hemisphere is dominated by upwelling, and the other by downwelling. In recent years, the giant impact origin described by Andrews-Hanna et al. [4], Kiefer [42] and Marinova et al. [55] has gained favor. Still, a combined origin from degree-1 mantle convection caused by this giant impact has also been put forward as an explanation for the dichotomy [18].

Other large scale surface features of note include large impact basins such as Utopia, Hellas, and Argyre, as well as major volcanic regions and features. Chief among these volcanic regions is the Tharsis rise, or Tharsis bulge as it is sometimes termed (Figure 1.2). This broad dome, constructed of basaltic lava, is ∼8000 km in diameter and up to 10 km high, and contains several large shield volcanoes, including Olympus Mons and the line of three Tharsis Montes [37]. The rise itself was built up by the end of the Noachian, with the major

volcanic shields growing over the following Hesperian and into the early Amazonian, and localized volcanic activity continued into geologically recent times, perhaps as recently as 2.4 Ma [14, 63, 69, 74].

Tharsis and its large volcanoes are typically attributed to a single long-lived mantle plume [13, 30], or several associated plumes feeding the different volcanoes [41, 43, 53]. The single plume case would be another example of degree-1 convection. In earlier geodynamic modeling, the existence of a thin bridgmanite layer and the associated endothermic phase transition in the Martian lower mantle has been shown to favor the development of degree-1 convection [28, 29, 30]. The absence of a bridgmanite layer, as confirmed by InSight, precludes this mechanism for generating degree-1 convection. However, as Roberts and Zhong [76] and my testing to replicate their results show, models with effectively no bridgmanite layer, but including a sufficiently large jump in viscosity ($\geq$10x) in the mid-mantle corresponding with the top of the transition zone (and, in retrospect, the $\sim$1000 km discontinuity identified by Huang et al. [34] can still produce and sustain degree-1 convection.

The Tharsis rise is superposed over, and approximately centered on, part of the dichotomy boundary [64]. This has led many to propose a causal link between the existence of the dichotomy and the subsequent development of Tharsis and its long lived volcanism [48, 77, 85, 98, 99, 103, 106]. For example, King and Redmond [48] propose that Tharsis is the result of small-scale edge driven convection at the dichotomy boundary, caused by the step in crustal thickness, or the possible associated step in lithospheric thickness. However, my modeling with a simplified equatorial dichotomy has not shown a tendency to develop small-scale convection with a realistically sized step in lithospheric thickness, and even an unrealistically large step smooths out well before present-day.

Another major volcanic region is Elysium. The Elysium rise (Figure 1.2) appears to essentially be a much smaller version of Tharsis, albeit still comparable in size to the largest

igneous provinces on Earth. While also very long-lived, the Elysium rise itself and its volcanic shields went extinct sooner than Olympus Mons and the Tharsis Montes, with a steep decline after a peak ∼1 Ga [70, 90]. However, the greater Elysium region shows evidence of more recent activity to the southeast of the rise, including volcanism within the past 0.2-20 Myr in Elysium Planitia (the region where InSight landed), and in particular Cerberus Fossae ((see Figure 1.2)) [7, 33, 36, 90, 100]. Based on findings from InSight, Broquet and Andrews-Hanna [12] and Kiefer et al. [44] suggest there may be an active mantle plume beneath Elysium. Between Tharsis and Elysium lies the vast lava plain of Amazonis Planitia, produced by lava flows of the late, eponymous, Amazonian Period. Other, much older, volcanic regions of significance include the Syrtis Major province, as well parts of the Southern Highlands such as Tyrrhenus Mons and Hadriacus Mons [32, 61].

To summarize, volcanic activity on Mars was extensive and voluminous for the first 1-1.5 Gyr, but declined rapidly after the end of the Hesperian ∼3 Ga, with most of the limited activity occurring in the pre-existing Tharsis and greater Elysium regions [14]. Otherwise, Martian geology has since been dominated by impact cratering, a thick global cryosphere, and very infrequent flooding and fluvial erosion from groundwater and melting ice [14]. Nevertheless, occasional localized volcanism has continued almost to present-day [63, 69, 74], and the recent discovery of active seismicity at Cerberus Fossae [12, 68, 87] indicates a surprisingly high, if localized, level of present geodynamic activity.

1.2 Geodynamic Modeling

We can only directly observe the surfaces of planets–and in select locations on our own planet, up to a few kilometers below the surface. Yet the thousands of kilometers beneath the surface, comprising the immense volumes of planets, remain inaccessible to direct study. For the

purpose of studying planetary interiors, starting on Earth well over a century ago, geophysical methods such as seismology, and gravity and magnetic surveys, have been devised. The former enabled the discovery an demarcation of the layers within our planet such as the inner core [51], outer core [52], and the crust and mantle [60]. Like Earth's mantle, the mantle of Mars accounts for the majority of the planet's mass and volume. The mantles of rocky planets, while overwhelmingly solid, slowly flow and convect below their respective lithospheres, driven in large part by heat leftover from planetary formation flowing up from the core and through the mantle, as well as by radioactive decay within the mantle rock [62]. These motions drive processes such as volcanism, and–on Earth, not Mars–plate tectonics, which we see evidence of on the surface. With geodynamic modeling codes such as CitcomS [93, 108, 109], we can model this flow of heat and mass over geologic time, by solving the equations for the conservation of mass, momentum, and energy. Additional processes, such as melt production, can be modeled as well.

1.2.1 History of geodynamic modeling

The history of geodynamic modeling began with 2D Cartesian geometries [16, 17, 57, 101], including the development of codes such as ConMan [46]. By the mid-1990s, advances in computing power enabled the development of codes to model global 3D spherical shell geometries. Initially, these were relatively course and were used to model the basic global patterns of one (degree-1 convection) or more plumes arising in the mantles of Earth and other planets [28, 29, 30, 76, 107]. Other geodynamic codes have employed the middle ground of a 2D axisymmetric annular geometry [39, 41]. Even in more recent years, parameterized 2D models such as the axisymmetric mode of the 3D code StagYY [91] continue to find use in more rapidly modeling mantle convection and testing more parameters [105]. Full 3D spherical shell codes have been further developed as the state of the art of geodynamic

modeling in the early 21st century, resulting in more modern codes such as CitcomS [93, 108, 109], the aforementioned StagYY [91], and more recently ASPECT [31, 50].

There have been a number of additions to geodynamic codes to increase model fidelity, which have become common practice over the past decade. These are not a part of the standard CitcomS distribution, but I have added them to my version of the code. Earlier geodynamic modeling relied on setting a constant heating rate, which is not physically realistic. We now consider decaying radiogenic heating, accounting for the fact that as the heat producing elements (HPE), chiefly uranium, thorium, and potassium-40, decay in order to produce this heating term, and thus their concentration declines exponentially. (Including decaying radiogenic heating over time has also allowed some studies to account for the heating from short lived isotopes aluminum-26 and iron-60, which produced significant amounts of heat in rocky bodies in the early solar system, particularly for smaller bodies.) Related to this development is accounting for the enrichment of HPE in the crust, and the corresponding depletion in the mantle. Earlier geodynamic modeling was also typified by a constant CMB temperature as the bottom boundary condition. In actuality, the CMB temperature changes over geologic time, generally decreasing as heat from the core escapes through the mantle, and furthermore there is a coupling between the flow of heat within the core and within the mantle. Consequently, the initially fully molten core of a planet can cool and begin to freeze out, growing an inner core, as Earth has done, releasing more heat via the rising of light elements (ultimately gravitational potential energy) and latent heat of fusion. To account for this cooling and the potentiality of inner core nucleation, we use the 1D model of Stevenson et al. [89].

1.2.2 Melting

The consideration of mantle melting and incorporation of these calculations within the geodynamic codes is another major thread in the evolution of geodynamic models, and indispensable for my research. (My own implementation of melting calculations within CitcomS, used for the work presented in Chapter 3, is discussed in great detail in Chapter 4.) For Earth, as with the broader case of geodynamic modeling, this started with 2D Cartesian geometries, such as the work of McKenzie and Bickle [57] and Watson and McKenzie [101]. The earlier geodynamic modeling of melt production in the Martian mantle performed by Kiefer [41] in 2D axisymmetric geometry calculated the melt fraction as a linear function of the difference between the solidus (in the case of Kiefer [41], the dry solidus of Bertka and Holloway [9]) and a hypothetical liquidus 200 K above the solidus. It later became common practice in geodynamics to use the experimentally derived parameterized melting model of Katz et al. [38] to calculate the melt fraction as a function of temperature and pressure, and this is incorporated into the standard version of ASPECT. The utility of Katz et al. [38] is that it includes a solidus, a liquidus, and a relatively straightforward nonlinear way to calculate melt fraction. However, Katz et al. [38] specifically applies to the peridotite composition of Earth's upper mantle, and Mars's mantle has a different composition. While Šrámek and Zhong [85] and Kiefer and Li [43] do consider the Katz et al. [38] solidus to be in good agreement with then-available solidi for Mars ([2, 9, 56], I found it to be different enough from the more recent Mars solidus of Duncan et al. [21] to significantly alter melt production. Therefore, I use the Duncan et al. [21] Mars solidus, which is a fit to the results of high pressure experiments done on the simplified Dreibus and Wanke [20] composition of Bertka and Fei [8], in place of the Katz et al. [38] solidus in my melting algorithm. Unfortunately, a comparable Mars liquidus, let alone hypothetical "lherzolite liquidus" (see Chapter

4 and Katz et al. [38]), are not available for the Martian mantle, so I retain those of Katz et al. [38].

Melt production can be estimated by post-processing the temperature and velocity data. Yet the post-processing approach has a number of drawbacks. For one, while the direct melt-reducing effect of the temperature drop from the latent heat of melting may be approximated by reducing the post-processed temperatures as Kiefer [41] does, this does not permit the latent heat of melting (or freezing) to be included in the energy equation. Even if one is not considering latent heat, the melting calculations being an integral part of the code allow the melt to be dealt with dynamically, for example advecting it through the mantle, extracting some portion of it, or addressing compositional changes. There is also the practical problem that replicating in post-processing the temporal resolution easily afforded by melting calculations within the geodynamic code requires the full temperature and velocity fields to be output every step. With my models taking on the order of 100,000 time steps to complete, this is simply not feasible, so performing melting calculations in the geodynamic code itself allows much more precise tracking of melting over time.

Acceptable geodynamic modeling of melt production should not only satisfy the InSight constraints for a present-day cool mantle and thick lithosphere, but also the general volcanic history of Mars. The models should produce sufficiently large volumes of melt over the first 1-1.5 Gyr to account for the Tharsis rise, followed by a steep decline in melt production, and the ensuing ∼3-3.5 Gyr of either comparatively little melting, or generally no melt with occasional small pulses of melt production.

Spacecraft, lander, and rover missions have provided us with a wealth of information on the nature and conditions of other planets such as Mars, as well as give us new questions to answer. Aside from the inferences drawn from surface features and composition, much of what we know about planetary interiors has been inferred from magnetometers and, in particular,

gravity measurements enabled by tracking the motions of orbiting spacecraft. While most missions focus on the surface or atmosphere, Mars InSight is the first interplanetary mission dedicated primarily to the study of a planet's deep interior. By itself, the data provided by InSight informs us directly about the present structure and seismic activity of Mars. But the degree to which these data alone can explain the evolution of Mars (and, by extension, terrestrial planets in general) is limited. Geodynamic modeling can be used to glean information how and why planetary interiors evolved the way they have, and infer how they started out. Yet, all models are limited in their explanatory capacity by the assumptions that go into them. The additional data and constraints provided by missions such as InSight can improve our ability to model the interior of Mars and investigate how features such as Tharsis and Olympus Mons came to be.

1.3 Outline of Chapters

In Chapter 2, I apply an analytic heat flow solution from Carslaw and Jaeger [15] to the data obtained from the Mars InSight mission's HP3 heat flow probe–affectionately known as the mole–in order to determine the thermal conductivity of the regolith at the InSight landing site. While this analytic solution is based on an infinite cylinder, and therefore should require a length to diameter ratio much greater than that of the mole, comparing my results with those of the complex numerical models used by the InSight team in Grott et al. [25] and Grott et al. [26] is a useful check on the complex numerical solution. Though the mole was unable to penetrate to the necessary depth to complete the heat flow experiment as planned, the InSight team did decide to perform several heating experiments over the Martian year to investigate the seasonal variation in regolith thermal conductivity. In spite of the low length to diameter ratio of the mole, my analytical method found the same seasonal trend

in thermal conductivity–albeit with values systematically 10-20% higher–as the numerical results reported in Grott et al. [26]. A highly condensed version of the work in this chapter was published as a supplement to Grott et al. [26].

In Chapter 3, I investigate mantle convection and melt production within Mars, informed by the results and constraints provided by the InSight mission. I overview how I implement melting calculations in the models, which is treated in greater detail in Chapter 4. I describe how I systematically test different rheologies (low activation energy vs. high activation energy); 5x, 10x, and 15x crustal HPE enrichments; three initial Core-Mantle Boundary (CMB) temperatures; and the inclusion of a hemispheric dichotomy. The models with the high activation energy produce geotherms consistent with InSight results, such as those reported in Huang et al. [34]. The warmer cases can produce small amounts of melt up to present-day, as desired based on evidence of geologically recent volcanism on Mars. However, it is very difficult to both produce sufficient melt to account for both the early emplacement of the Tharsis rise, and the limited extraction of mantle melt to the surface. This chapter is being prepared for publication in *Journal of Geophysical Research: Planets*.

In Chapter 4, I go into much greater detail about the how I calculate melting. I include an overview of the premeditation of Katz et al. [38] that I use to determine the melt fraction at a given temperature and pressure, which is just the first step. I then explain the equations that use this melt fraction, and the temperatures and velocities computed by a geodynamic model such as CitcomS, to calculate the resulting rate and volume of melt production. Latent heat–of melting or otherwise-is not appropriate to include in the Boussinesq approximation used in the models of Chapter 3. However, I do derive the inclusion of latent heat of melting in the conservation of energy equation. Along with this I review how latent heat has proved difficult to implement, and why it makes sense to include in compressible convection models, but not in a purely Boussinesq approximation. I follow with my recent results testing the effects

of compressible convection with an extended Boussinesq approximation, albeit still without latent heat of melting. These preliminary results suggest that compressible convection does not have a significant impact on melting for Mars, at least in the early part of its history when Tharsis formed. Further development of this work will be the basis for a second mantle convection publication.

Lastly, In Appendix A, I detail how I implemented and adapted the method of Banerdt [6] and Andrews-Hanna et al. [4] to use measurements of Mars' shape and gravity to determine a more realistic pre-Tharsis hemispheric dichotomy, and incorporate this into CitcomS. While I have not yet had the chance to systematically test models with this more realistic dichotomy, as I have with the simple equatorial/degree-1 dichotomy I opted for in Chapter 3, this more complex and realistic dichotomy geometry provides an avenue to expand on the results presented in Chapter 3.

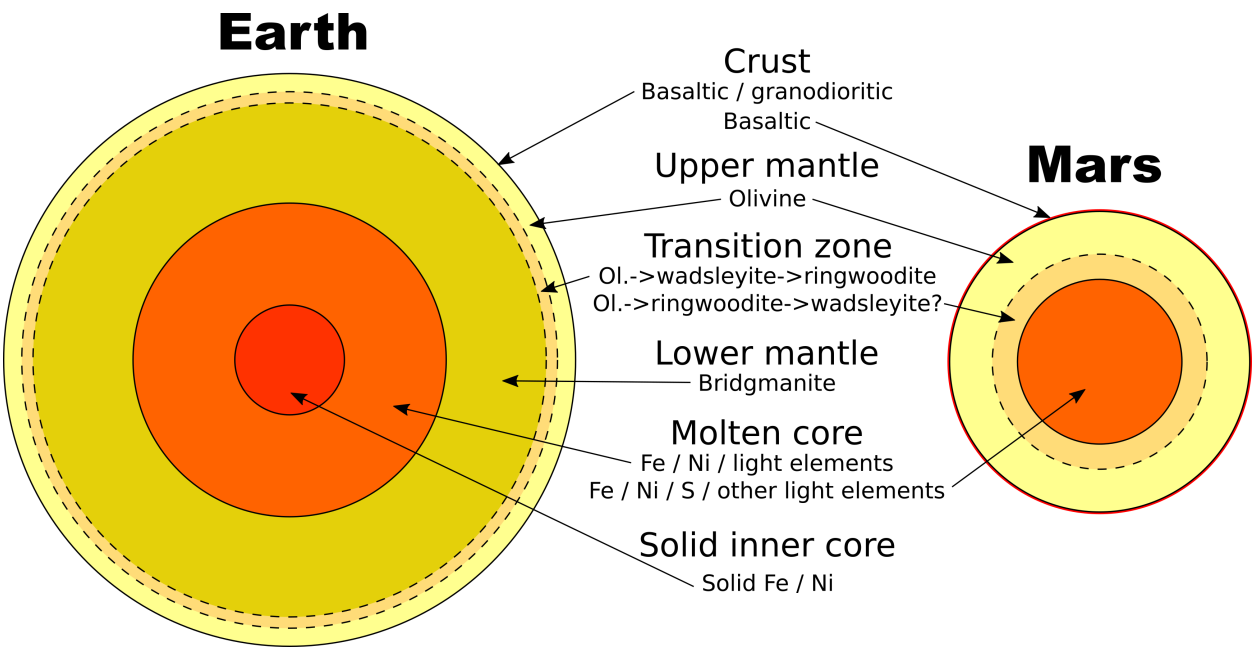

Figure 1.1: Scaled comparison of the interior structures of Earth and Mars. In this schematic, Earth's crustal thickness is generalized to that of its oceanic crust, as this covers the majority of the planet and is more analogous to Mars' basaltic crust.

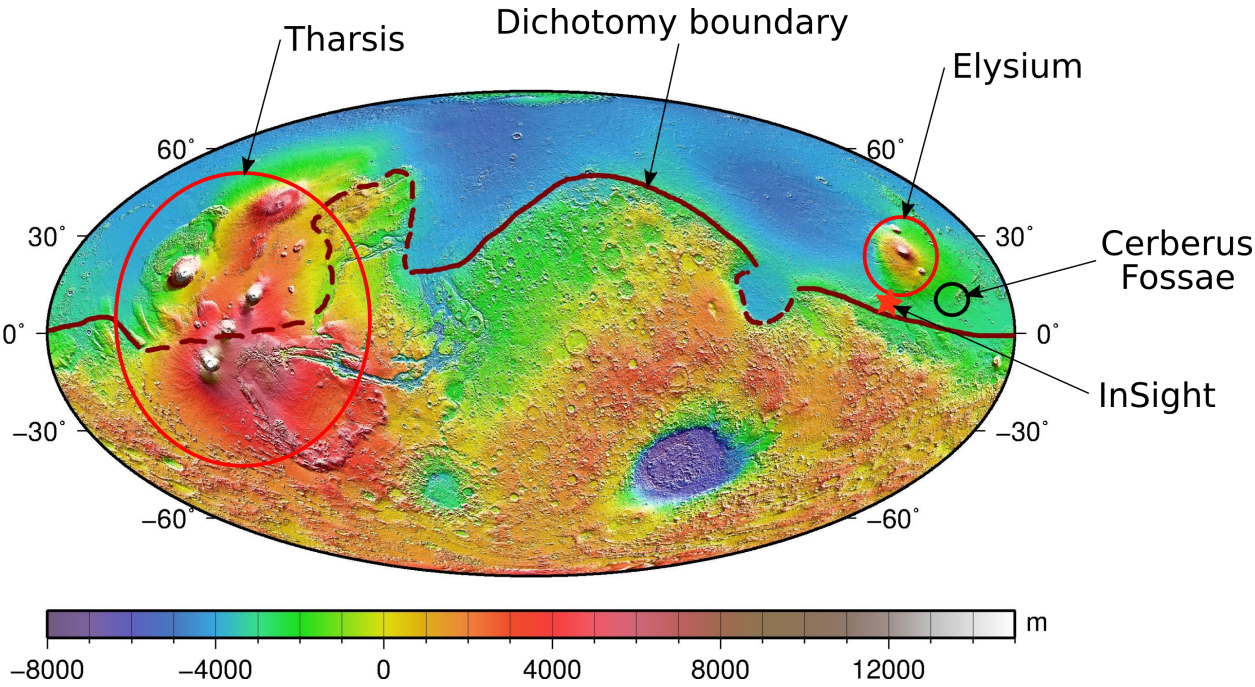

Figure 1.2: Topographic map of Mars, showing the dichotomy boundary (dashed where uncertain), the Tharsis and Elysium rises, Cerberus Fossae, and the InSight landing site.

Chapter 2

Analytic Solution to Thermal Conductivity for Mars InSight HP3

A condensed form of the work in this chapter has been published in Geophysical Research Letters as part of a supplement to Grott et al. [26] "Seasonal variations of soil thermal conductivity at the InSight landing site". The results reported here were used to confirm the numerical models. Josh Murphy implemented the analytical formulation from Carslaw and Jaeger [15] and used this to estimate thermal conductivity from the HP3 heating experiment time series data provided by the HP3 co-PI Matthias Grott.

2.1 Introduction

The InSight lander's Heat Flow and Physical Properties Package (HP^3) (see Figure 2.1) was designed to measure the heat flow at the landing site in the Elysium Planitia. HP3 was carried on the lander deck, along with the seismometer package, the Seismic Experiment for Interior Structure (SEIS). These instruments were deployed by the Instrument Deployment Arm (IDA) over the weeks following November 26, 2018 landing of InSight. The major components of HP^3 include a surface-based radiometer (RAD); the Thermal Excitation and Measurement–Passive (TEM-P), a tether outfitted at increments with temperature sensors; and the heat flow probe itself, better known as the mole. The mole, which is 2.7 cm wide

and 40 cm long, was intended to mechanically hammer itself between three and five meters deep into the regolith, dragging the TEM-P with it. The mole also contains the Thermal Excitation and Measurement–Active (TEM-A), the heating foils used for active heating and measuring the self-heating curve of the mole in order to determine the thermal conductivity of the regolith. The TEM-P was intended to measure the temperature gradient within the regolith from the surface to at least 3 m depth.

Unfortunately, the mole could not penetrate as intended, due to insufficient friction with the regolith to resist the recoil force generated by the self-hammering ([83, 84]. The robotic arm was used to remove the support structure and pin the mole in place, and this allowed some further penetration, such that the back cap reached 3 cm below the surface. The arm was also used to fill in and tamp down the enlarged hole left by the mole and its tilting, so as to ensure it was fully buried and in direct contact with the regolith. No further progress could be made (the final hammering occurring on Sol 754), and the combined attempts to get it to penetrate further left the mole tilted approximately 30° to the vertical. From this final position, as depicted in Figure 2.1, tilted and buried just below the surface, all six of the TEM-A heating experiments reported on below were conducted.

Geodynamic models, such as the work of Plesa et al. [72] for Mars, can predict or estimate the magnitude and global variation of heat flow from the Martian interior. Even a single point of data, such as that which HP3 would have provided had the mole and tether been able to get to depth, would greatly aid in constraining the actual heat flow out of Mars. The thermal conductivity of the regolith in which the mole buried itself is a necessary component for the determination of the heat flow. While unfortunately the mole did not work as planned, the InSight team was still able to determine the thermal conductivity of the regolith, and through multiple measurements track how it varies over the Martian year. This informs

us about the properties of the surface material (i.e., regolith) on Mars, and extends and confirms our understanding of seasonal change on Mars.

2.2 Methods

In Chapter 13 of Carslaw and Jaeger [15], Section 13.7 describes the solutions of heat conduction in a system consisting of an infinite medium bounded internally by a perfectly conductive circular cylinder of radius a. A cylinder of sufficient length, such that length $\gg$ radius, can be approximated as a cylinder of infinite length. Consider a cylinder of infinite length that is placed within a medium (i.e., the regolith) with thermal diffusivity κ and thermal conductivity K, and then heated along its z-axis. If the initial and boundary conditions are independent of the z and θ coordinates, then the temperature v as a function of radius r is given by

$$\frac{\partial v}{\partial t} = \kappa \left(\frac{\partial^2 v}{\partial r^2} + \frac{1}{r} \frac{\partial v}{\partial r} \right) \tag{2.1}$$

The authors use the method of Laplace transforms to derive their solutions in Chapter 13. Problem II in Section 13.7 considers the case in which the cylinder, initially at zero temperature, is supplied heating power at a rate Q per unit length (W/m) for non-dimensional time $\tau > 0$. (Dimensional time t is non-dimensionalized as $\tau = \kappa t / a^2$, where a is the radius of the cylinder.) The temperature increase V of the cylinder is given by equation (8) in Carslaw and Jaeger [15] section 13.7

$$V = \frac{2Q\alpha^2}{\pi^3 K} \int_0^\infty \frac{1 - \exp(-\tau u^2)}{u^3 \Delta(u)} du \tag{2.2}$$

where the non-dimensional parameter α is defined using the cylinder radius a, the regolith density ρ, the regolith heat capacity c_p, and the heat capacity of the cylinder per unit length (in J K^{-1} m^{-1}) S as

$$\alpha = \frac{2\pi a^2 \rho c_p}{S} \tag{2.3}$$

and $\Delta(u)$ is calculated from the Bessel functions as follows

$$\Delta(u) = (uJ_0(u) - \alpha J_1(u))^2 + (uY_0(u) - \alpha Y_1(u))^2 \tag{2.4}$$

where J_a and Y_a are the Bessel functions of the first and second kind, respectively [1].

Problem 13.7.IV in Carslaw and Jaeger [15] considers a situation like 13.7.II where there is contact resistance R between the cylinder and the medium, which along with K determines the value of the non-dimensional parameter $h = 2\pi RK$. The true value of R between the mole and regolith is unknown, but my results show the modeled mole (cylinder) temperature is insensitive to it over the range of plausible R values ($10^{-5}/L$ to $10^{-4}/L$ m W^{-1} for probe length L = 0.4 m). Regardless, it turns out that using this method to determine K–derived by taking the limit to the following series as $t \to \infty$ such that the terms with h (and thus R) drop out–does not require one to actually know the value of R. For large non-dimensional times $\tau = \kappa t/a^2$, the temperature of the cylinder is approximated by the truncated series from equation (18) in Carslaw and Jaeger [15] section 13.7

$$V = \frac{Q}{4\pi K}\left(2h + ln\left(\frac{4\tau}{C}\right) - \frac{4h-\alpha}{2\alpha\tau} + \frac{\alpha-2}{2\alpha\tau} ln\left(\frac{4\tau}{C}\right)\right) \tag{2.5}$$

The simpler form of equation 2.5 makes it possible to derive a simple formula for the thermal conductivity, which can the be calculated using temperature vs. time data and the heating rate. The slope of V vs. $\ln(t)$, $dV/d\ln(t)$, or equivalently using the chain rule $t \cdot dV/dt$, can be derived analytically from equation 2.5 (recall τ is just t times a constant), and takes the form

$$\frac{dV}{d\ln(t)} = \frac{dV}{dt}\left(\frac{d\ln(t)}{dt}\right)^{-1} = t \cdot \frac{dV}{dt} = \frac{Q}{4\pi K}\left(1 + (c_1 + c_2)t^{-1} - \frac{c_2 \ln(c_3 t)}{t}\right) \tag{2.6}$$

$$K \approx \frac{Q}{4\pi}\,[slope]^{-1} \tag{2.7}$$

where $c_1 = (4h - \alpha)a^2/2\alpha\kappa$, $c_2 = (\alpha - 2)a^2/2\alpha\kappa$, and $c_3 = 4\kappa/\alpha^2 C$. The limit of equation (2.6) above as $t \to \infty$ is $Q/4\pi K$. Thus at large t (or τ), the curve V vs. $\ln(t)$ approaches a line of slope $Q/4\pi K$. The thermal conductivity K can, in principle, be quickly determined using equation (2.7) with the slope of the data over an interval of time where the plot is linear (i.e., by least squares regression). The calculated thermal conductivity is only dependent on that data and the known Q, but no other parameters such as the diffusivity.

We iterate over all combinations of window start time (11 to 251 data points, or 14.41 to 360.4 min.) and window length (11 to 181 data points, or 14.41 to 259.5 min.). The regression with the highest correlation coefficient R^2 (i.e., closest to 1), and therefore the greatest linearity, is taken as the optimal result from which K should be calculated. However, as reflected in Figure 2.5, the choice of start time or window length does not greatly impact the thermal conductivity value, particularly for data taken on or after Sol 874.

Once the calibrated InSight mole data is available, the first step is subtracting the diurnal temperature cycle from the temperature vs. time data. (This processing step not done by

me, but rather the subtracted data were provided to the InSight Team by Matthias Grott, so everyone was working with the same data.) Temperature is recorded for one or two sols prior to beginning active heating, and the temperature cycle does not vary significantly from one sol to the next. After removing the diurnal trend, the temperature vs. ln(time) curve becomes approximately linear after approximately exp(9) seconds, or just over 2 hours, from the start of active heating. Thermal conductivity can be calculated with the above analytical method using a subset of the data after this point. Here, I use the regression slope from the two hour window with the best linear fit (highest R^2 value). Recall that R^2, or the coefficient of determination is the quantity one minus the quotient of the residual sum of squares divided by the total sum of squares, or

$$R^2 = 1 - \frac{\sum_i (y_i - \hat{y}_i)^2}{\sum_i (y_i - \bar{y})^2} \tag{2.8}$$

where y_i is the ith data point (measured temperature at time t_i), $\hat{y}_i$ is the temperature 'predicted' by the linear fit, and $\bar{y}$ is the overall mean of the measured data (temperatures).

Seasonal trend in thermal conductivity

I have applied my method to more recent InSight TEM-A data from sols 827, 874, and 1070. In combination with the measurements from sol 798, these data should, in theory, be better quality than earlier (pre-sol-798) measurements from when the mole was less buried. The trend observed in my calculated thermal conductivities (see Table 2.1 and Figure 2.3) is consistent with the trend found by the numerical and statistical method of Grott et al. [25] and Grott et al. [26], which in turn follows the expected trend based on predictions of the effect of seasonal pressure changes.

The regolith thermal conductivity, being dominated by conduction of heat through the thin air in pore spaces, does change over the Martian year as the temperature and pressure vary. The main factor is air pressure, to which thermal conductivity is positively correlated. On Mars, the air pressure peaks in the spring and autumn. At those times of the year, solid CO_2 (dry ice) coating the polar water ice cap of the hemisphere experiencing winter, sublimates into the atmosphere. This CO2 deposits on the opposite ice cap after the following solstice, which in turn leads to a pressure minimum. Therefore there is a clear semi-annual variation in both air pressure and regolith thermal conductivity. Although, due to additional factors such as the eccentric orbit of Mars, the northern summer trough and autumn peak are more extreme than their winter/spring counterparts.

2.3 Results and Discussion

My analytically determined values of thermal conductivity, as calcualted from the linear regression window with the highest R^2 value, for the six active heating experiments where the mole was in its final position are listed in Table 2.1. Plotting these analytically determined thermal conductivities, as in Figure 2.3 shows they parallel the values obtained by the numerical models of Grott et al. [26].

The most glaring issue with applying analytical solutions, such as the one detailed herein, to the mole is the assumption of infinite length of the heat source, which in practice requires the length to width ratio to be high (e.g., greater than 20–30). At 40 cm long and 2.7 cm wide, the ratio for the mole is less than 15, so the analytical solutions were not expected to be adequate and a numerical approach was decided on instead ([25, 82]). Nevertheless, my results, as well as those of Paul Morgan (also published in the supplement to Grott et al. [26]), show analytical solutions work surprisingly well with the mole.

Table 2.1: Regolith thermal conductivity at the InSight landing site as measured at different sols (Mars days), with their corresponding solar longitude (indicating time of year) L_s. The analytical thermal conductivity (K) is my value determined by the regression slope of the mole self-heating curve over the time window with the highest R^2 (see text). The numerical K values are those reported in the main text of Grott et al. [26], as determined from the self-heating curve using numerical models.

Sol	**L$_S$** (°)	**Analytical K** (W m^{-1} K^{-1})	**Numerical K** (W m^{-1} K^{-1})	**Window start time** (minutes)	**Window length** (minutes)
798	8.0	0.0458	0.0383	142.7	33.15
827	22.0	0.0458	0.0395	129.7	47.57
874	44.2	0.0445	0.0397	233.5	111.0
1070	135.3	0.0417	0.0366	178.7	90.81
1160	184.0	0.0431	0.0371	271.0	222.0
1204	210.0	0.0441	0.0390	190.3	249.4

I expand on the results published in the supplement of Grott et al. [26] by examining the sensitivity of the R^2 value and the estimated thermal conductivity to varying the length and start time of the regression window, as opposed to merely accepting that which yields the best linear fit (highest R^2). As indicated in Figure 2.4, R^2 is very high, for example greater than 0.9998, over most of the parameter space of window start times and window lengths. The histograms in 2.5 show the density of thermal conductivity values across the parameter space of regression window start time and window length. The distributions are all non-normal, with distinct right tails, and while some may appear log-normal, they are not. That each histogram has one or two close peaks with distinct tails increases my confidence that, despite the very high R^2 for a wide range of regression windows, the best estimate for thermal conductivity using my method is captured within the selected range of start times and window lengths, and the value with the maximum R^2 is close to the optimum. That said, the bimodal distribution of the earlier sols does somewhat disrupt this. For example, for sol 827, the maximum R^2 method returns a K value near the secondary peak, while the mean and median are close to primary peak at a lower value of K.

The histogram peaks appear to steadily get tighter over time. It is not clear why this is the case–perhaps a result of the mole and surrounding regolith settling. However, this apparent large reduction in spread is not reflected in the standard deviations or the differences between the percentiles. The errors bars, as plotted in these two ways in Figure 2.3, therefore remain about the same size–roughly twice as wide as the 1-σ error of the numerical results of Grott et al. [26]. For all six cases, the K value as determined from the maximum R^2 falls within 1σ of the histogram mean, and between the 15.9 and 84.1 percentiles (which would correspond to 1σ from the median–and the equivalent mean–if the K values were normally distributed, as the numerical results of Grott et al. [26] approximately are, but my histograms are not. Again, this increases my confidence that the analytical K values in 2.1 are generally representative of the results this regression method can provide.

2.4 Conclusions

The analytically derived thermal conductivities generally follow the the same expected seasonal pattern–a correlation with air pressure–as the numerical results of Grott et al. [26]. Comparing the individual values, my results are within 10-20% of those obtained by much more complex numerical methods, albeit consistently biased high. Given the low length to diameter aspect ratio of the mole, this degree of agreement with the numerical results is surprising.

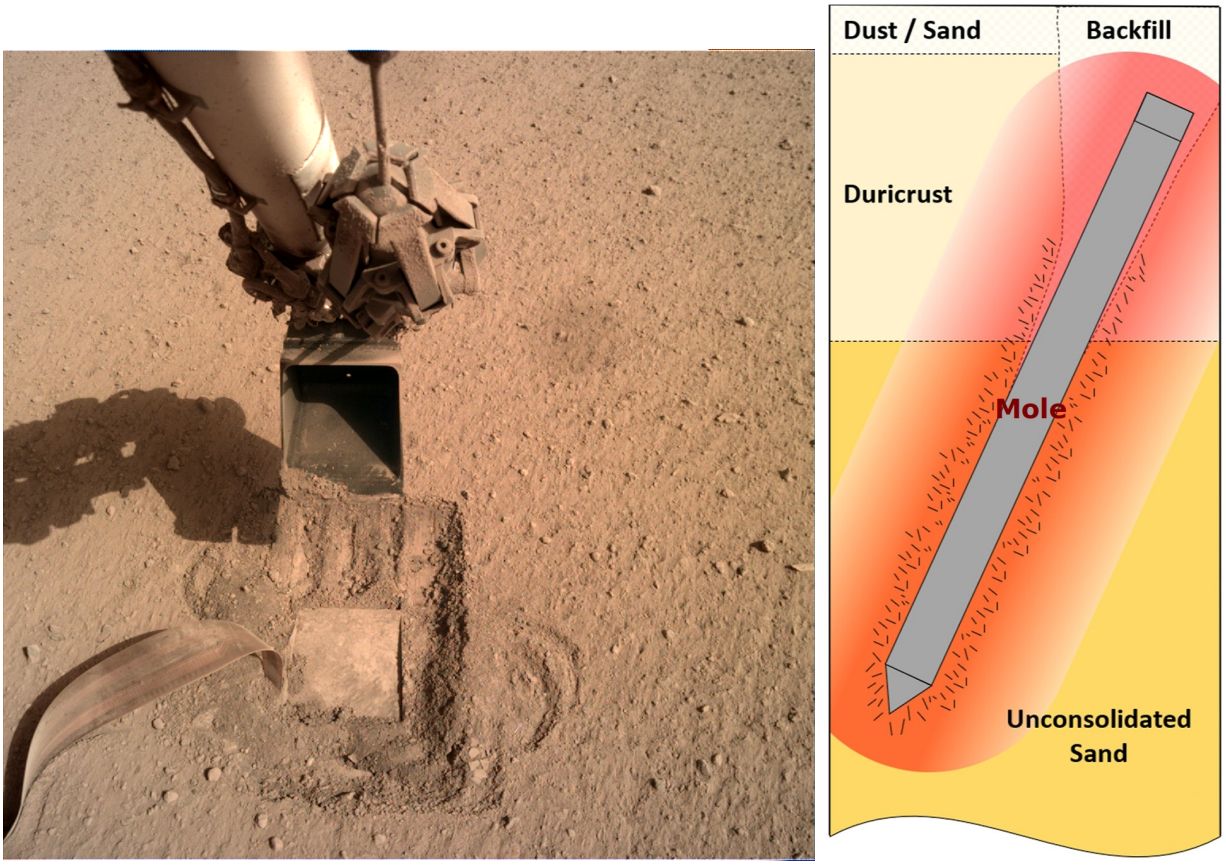

(a) (b)

Figure 2.1: (a) Final position of the mole, as imaged on Sol 775, buried in the backfilled pit with just the back cap exposed ~ 3 cm below the surrounding surface. Credit: NASA/JPL-Caltech (https://mars.nasa.gov/raw_images/890722/). (b) Schematic of mole tilt and position within the layers of the regolith. Modified from Grott et al. [26].

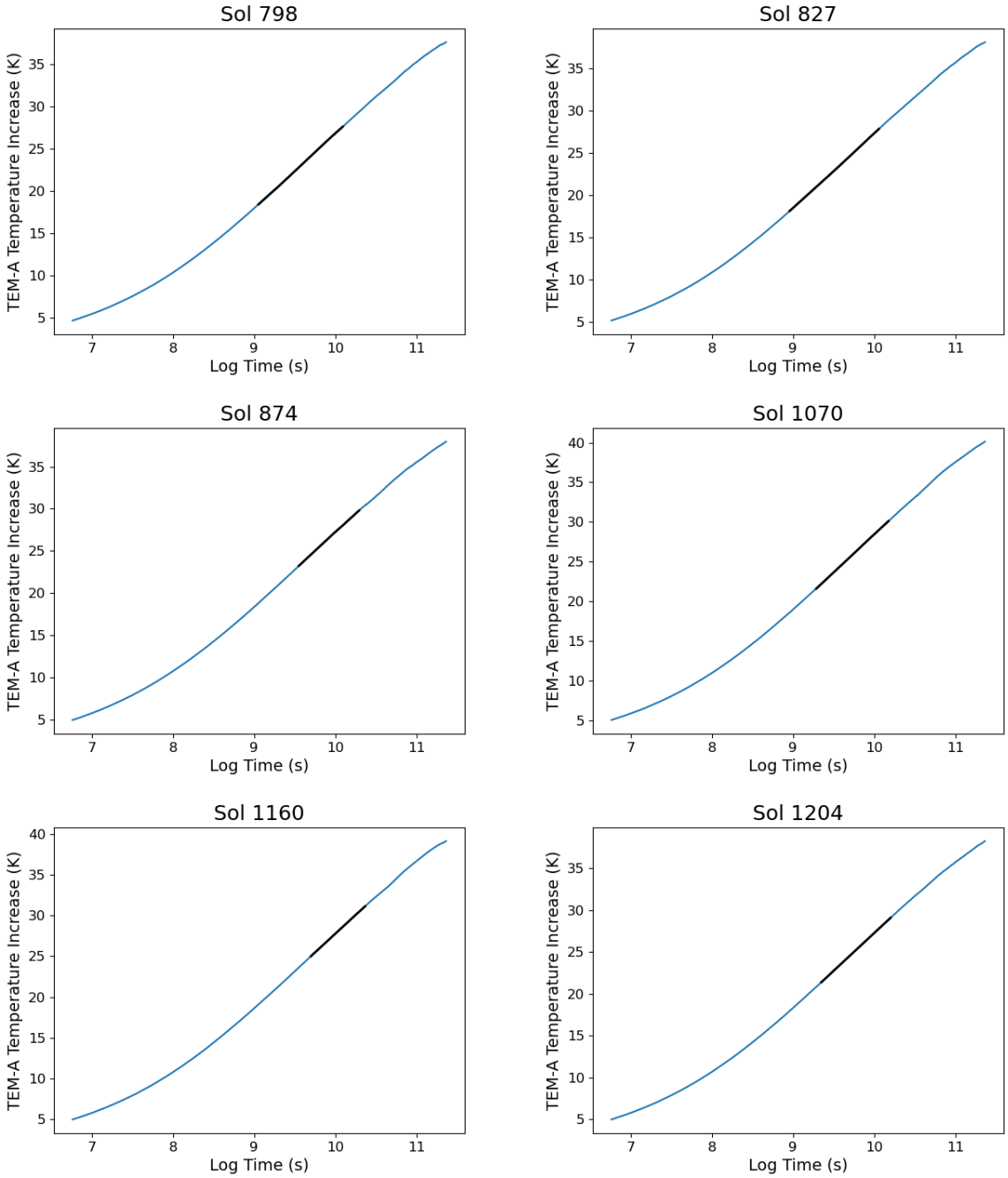

Figure 2.2: Self heating curves for all six TEM-A experiments for Grott et al. [26], plotted with a log scale for time to show the linear trend. The bold parts of the lines are the window with the highest R^2, as used to obtain the values of thermal conductivity reported in Table 2.1.

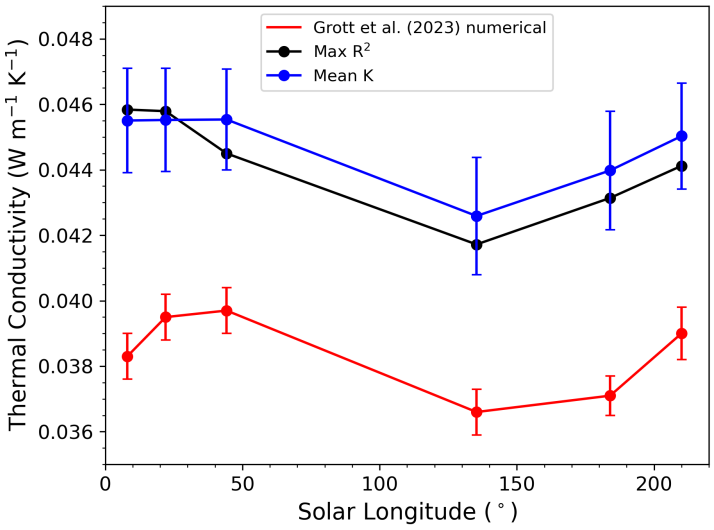

(a) a

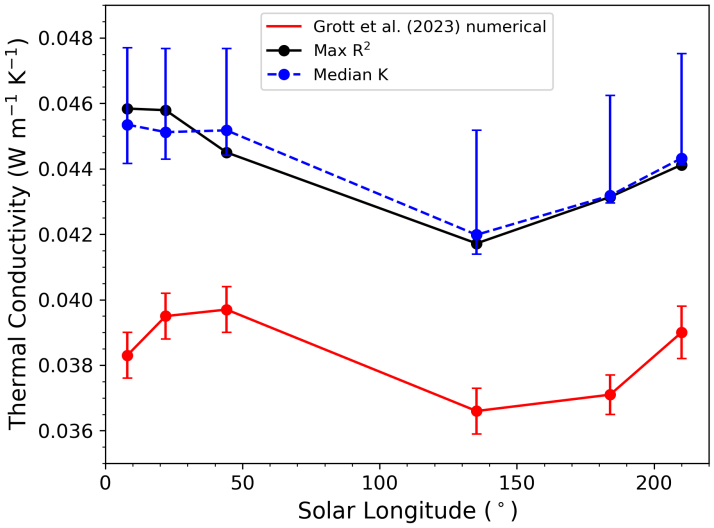

(b) b

Figure 2.3: Seasonal variation in regolith thermal conductivity (K) due to atmospheric pressure changes, as measured at the InSight landing site. My K values corresponding to the highest R^2 values, as reported in the supplement to Grott et al. [26], are in black. The numerical results of Grott et al. [26] with their 1-σ error bars are plotted in red. Plot (a) shows the mean K (solid blue line) across the range of window start times and lengths tested, with 1-σ error bars. Plot (b) is identical, except the mean is replaced by the median k value (dashed blue line), with the error bars extending between the 15.9 and 84.1 percentiles. This would correspond to 1-σ if the regression-determined K values for a given sol were normally distributed–which they are not (c.f. the histograms in Figure 2.5).

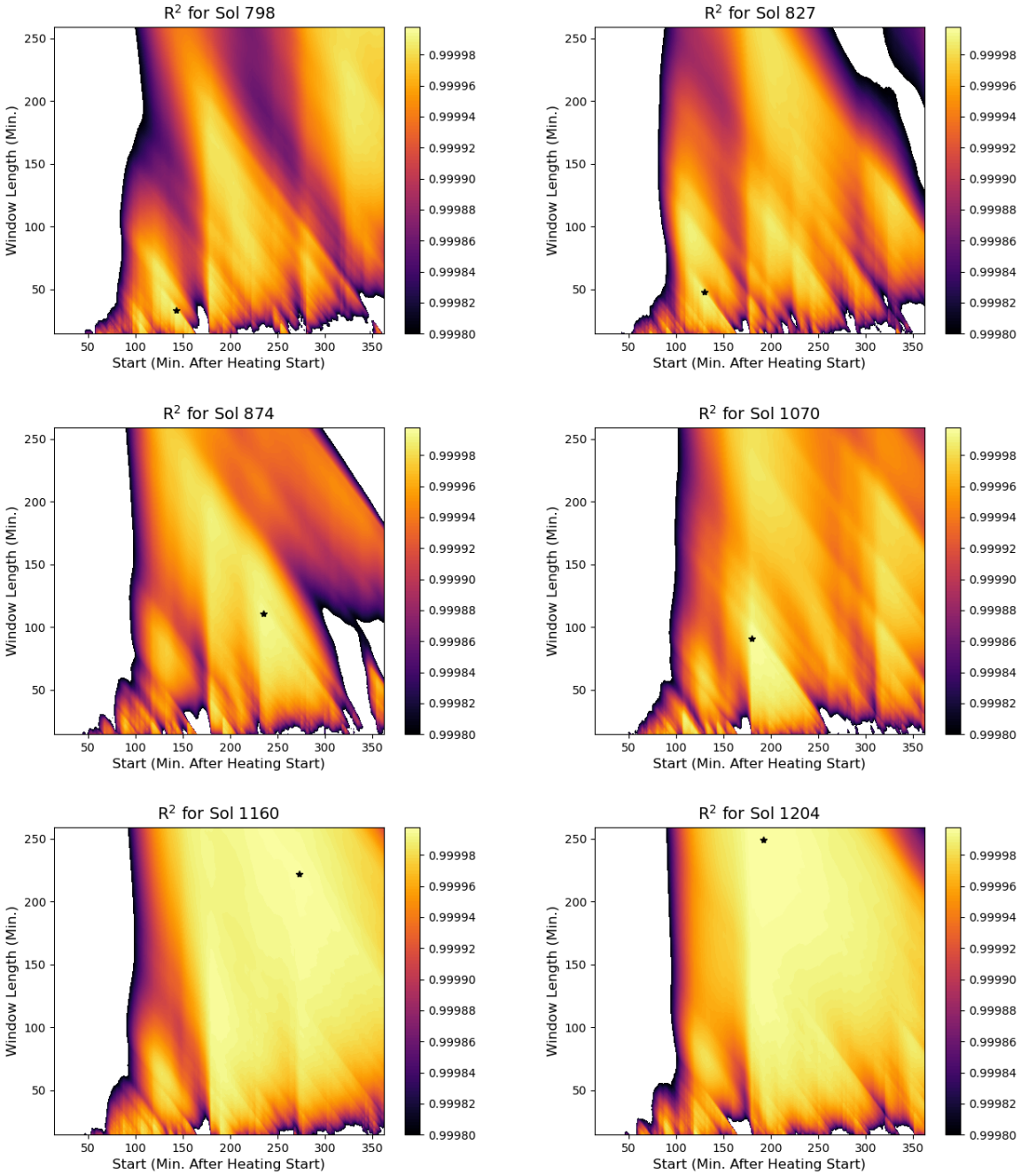

Figure 2.4: Shaded contour plots of the R^2 values greater than 0.99980, as a function of regression window length vs. start time, for each of the six active heating experiments. The points corresponding with the maximum R^2 are marked with a star. These plots indicate a very good linear fit across a wide range of those two parameters, not just where R^2 is greatest.

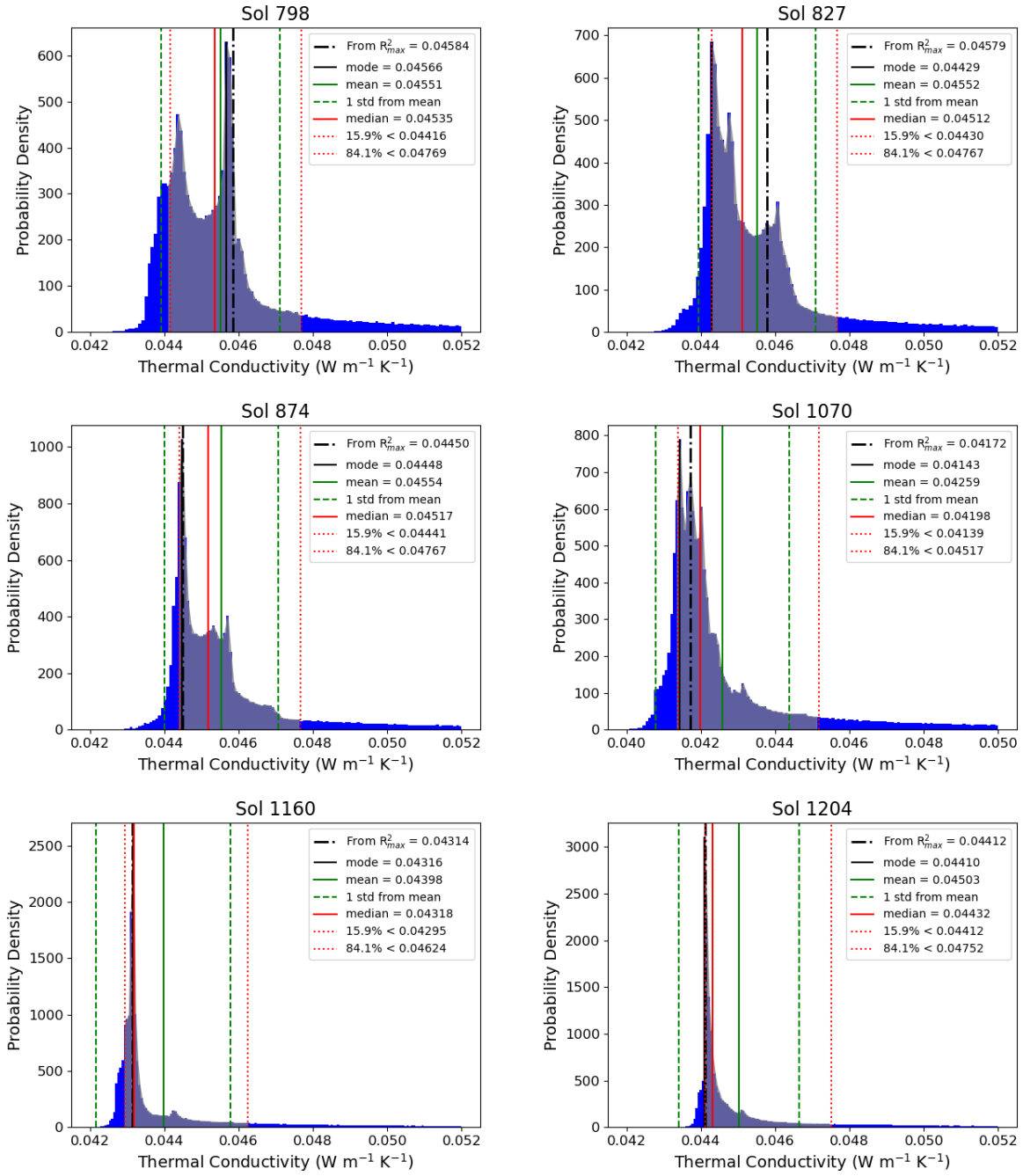

Figure 2.5: Histograms of the thermal conductivity value calculated from the regression slope, when varying the window length from 10 to 180 time steps (approximately 14–259 minutes) and varying the window start time after the beginning of active heating from 10 to 250 time steps (approximately 14–360 minutes). The R^2_{max} is the thermal conductivity value I reported in Grott et al. [26]. Also shown are the mean, median, and mode values of R, as well as the mean ±1 standard deviations. The shaded range, with vertical dotted red lines at either end, shows the region between the 15.1 and 84.9 percentiles, which would correspond to mean ±1 standard deviation if the thermal conductivities were normally distributed.

Chapter 3

Mars Mantle Convection

This chapter will be submitted to Journal of Geophysical Research: Planets. Josh Murphy and Scott King are responsible for the initial conceptualization. The CitcomS simulations, and the implementation of the melting algorithms in CitcomS, were designed and performed by Josh Murphy.

3.1 Introduction

Results from the InSight mission provide new constraints on the temperature, structure, and geodynamic evolution of the Martian interior. The InSight mission was the first to record quakes (unambiguously) and impacts on Mars [5, 24]. Using reflections of seismic waves from the core-mantle boundary of Mars together with geodetic data, Stähler et al. [86] constrained the radius of the liquid metal core to be 1830 $\pm$ 40 km with a mean core density of 5700-6300 kg/m^3–implying that there is 10 to 15 wt % S in addition to other light elements dissolved in the nickle-iron core. The core radius is at the large end of the pre-mission estimate [81] and, implies that there is no bridgmanite layer above the core-mantle boundary. The absence of a bridgmanite layer is an important constraint for mantle dynamics because a thin bridgmanite layer is one mechanism to generate degree-1 convection [28, 29, 30].

The topography and crustal thickness of Mars are characterized by the dichotomy between the northern and southern hemispheres. The northern hemisphere is dominated by low-

lands which tend to have thinner crust, while the southern hemisphere is dominated by heavily cratered highlands which tend to have a thicker crust. Using InSight seismic data, Knapmeyer-Endrun et al. [49] found two possible Moho depths, the first at (20 ± 5) km and the second at (39 ± 8) km. The thicker crust is more consistent with the surface composition, while the thinner crust would require an increasing HPE concentration with depth. The thicker crust would also allow a slightly higher bulk crustal density ($3100\,\mathrm{kg\,m^{-3}}$) when compared with the thinner crust ($<2900\,\mathrm{kg\,m^{-3}}$). Considering either model and the aforementioned gravity and topography datasets, Wieczorek et al. [104] constrain the global average Martian crustal thickness to be between 24 and 72 km, with thinner crust in the lowlands (including the InSight landing site), and thicker crust beneath the highlands and Tharsis.

Huang et al. [34] constrained the depth of a mid-mantle discontinuity to be 1,006 ± 40 km by modeling triplicated P and S waveforms. Interpreting this seismic discontinuity as the transformation of olivine to a higher-pressure polymorph (likely ringwoodite) yields a mantle potential temperature of 1,605 ± 100 K. Using a parameterized convection approach, Huang et al. [34] suggest that the mantle potential temperature was 1,720 to 1,860 K soon after formation. When combining the 1,000-depth phase transition transition with an estimated crustal thickness from Knapmeyer-Endrun et al. [49], a present-day lithospheric thickness of 400-600 km [40], and moment of inertia and love number constraints, Huang et al. [34] prefer a model with 10 to 15x crustal HPE enrichment and present-day average surface heat flow of 21 to 24 $\mathrm{mW/m^2}$, implying a relatively sluggish mantle with a reference viscosity of 10^{20}–10^{22} Pa s. The InSight-constrained geodynamic modeling of Samuel et al. [79] favor 10x crustal enrichment, and orbital gamma ray spectrometry also supports an enrichment of ∼10-15x [11, 58, 94].

In addition to the new results from InSight, geodynamic models must also be consistent with the observed volcanic history of Mars. Mars' volcanic history, as well as the present-day topography and gravity field, are dominated by the Tharsis rise, a broad dome 8000 km in diameter and 10 km high–far larger than any terrestrial igneous province–containing several large volcanoes, centered in the equatorial western hemisphere [37]. The origin of the Tharsis rise is generally ascribed to one or more long-lived mantle plumes [13, 30, 41, 53]. While most of the rise itself was emplaced by lava lows by the end of the Noachian, and the large volcanic shields in the Hesperian, the region has remained volcanically active for most of the planet's history [63, 69, 74]. According to Neukum et al. [63], there is evidence of volcanism in Tharsis as recently as 2.4 million years ago. The relatively recent volcanic and tectonic activity, and modeled long-term stability of convection in the Martian mantle indicates that mantle melting is still occurring in the present day [41, 43, 53].

The Tharsis rise straddles the boundary between the thicker crust of the southern highlands and the thinner crust of the northern lowlands [64]. The contrast between these two hemispheres (zonal degree-1 topography) is referred to as the Martian crustal dichotomy. This feature is apparent in the hypsometry (elevation frequency distribution) of Mars, which has a bimodal distribution with peaks separated by 5.5 km [3, 102]. The origin of the dichotomy is still highly uncertain. It may be of internal origin, for example the result of degree-1 mantle convection [76, 106], or from a giant impact [4, 42, 55]. A hybrid origin from degree-1 mantle convection caused by the giant impact has also been proposed [18]. Several studies have considered a causal link between the dichotomy and Tharsis [48, 98, 99, 103, 106]. King and Redmond [48] propose that Tharsis is the result of small-scale convection at the dichotomy boundary caused by the difference in crustal or lithospheric thickness.

However, there are other significant volcanic regions besides Tharsis, including the Elysium rise which is a smaller version of Tharsis but, still comparable in size to the largest igneous

provinces on Earth. Unlike Tharsis, the Elysium rise itself and its volcanic shields appear to have had less recent volcanic activity than Olympus Mons and the Tharsis Montes in Tharsis, with a steep decline after a peak ∼1 Ga [70, 90]. However, the greater Elysium region shows evidence of more recent activity to the southeast of the rise, including volcanism within the past 0.2-20 Myr in Elysium Planitia, and in particular Cerberus Fossae [7, 33, 36, 90, 100]. Geophysical evidence also supports recent and presently active tectonism, possibly driven by magma, in Cerberus Fossae, as well a possibly active mantle plume beneath Elysium Planitia [12, 88]. Between Tharsis and Elysium lies the vast lava plain of Amazonis Planitia, produced by lava flows of the late, eponymous, Amazonian Period. Other, much older, volcanic regions of significance include the Syrtis Major province, as well parts of the Southern Highlands such as Tyrrhenus Mons and Hadriacus Mons [32, 61].

Geoid anomalies provide another constraint on the dynamics of planetary interiors [27, 45, 75]. However, as Mars' gravity field and geoid are dominated by the topography of the Tharsis rise, largely built up by lava flows, removing or greatly reducing the effect of Tharsis from Mars' measured gravity field allows a much more useful comparison with our model geoids. Zuber and Smith [110] calculated the low-degree (l=2-6) coefficients for Mars without Tharsis, which we use for comparison–though this "Mars without Tharsis" geoid retains shorter wavelength features associated with Elysium, as well the large shields of Tharsis, as well as large impact basins such as Utopia and Hellas. (Spherical shell modeling cannot include or produce the topography built up by lava or excavated by impacts.)

Using the 3D spherical shell geodynamic code CitcomS [93, 108, 109], we investigate the thermal and volcanic history of Mars. We consider runs successful if they are capable of producing: present-day temperature profiles (geotherms or potential temperatures) that fall within the range inferred from InSight results [34, 40]; geoid and topography power spectra consistent the the observations after removing the effect of Tharsis [110], and sufficient melt

in the first billion years to explain the widespread volcanism with isolated pockets of melt at present day. If the models are too hot, they will produce a persistent global melt layer lasting billions of years, while if they cool too quickly, melt production will be too low and end too early to be consistent with Mars. The observation of volcanic activity within the past 100 million, and even past few million years [7, 33, 36, 63, 100], means that acceptable models should produce small amounts of melt up to, or at least near, present-day.

Elysium is comparable in size to the largest terrestrial igneous provinces. Like Tharsis it also comprises a broad rise (2400 km $\times$ 1700 km) topped by large volcanoes and shows evidence for billions of years of volcanic activity–albeit not as recently as Tharsis ([54]) ([more recent source(s)]). However, geodynamicists typically focus on Tharsis, because Elysium and its three major volcanoes, while large by Earth standards, are markedly smaller than Tharsis and its largest volcanoes. Martian volcanism has been modeled as a single long-lived plume (Harder and Christensen, 1996). The mantle convective structure in this one-plume model is represented by a sectoral degree-1 spherical harmonic, where the hemisphere containing Tharsis is dominated by upwelling from the plume and the other hemisphere is dominated by downwelling [76]. Others, including Kiefer [41], Kiefer and Li [43], Li and Kiefer [53], favor a multi-plume model for Tharsis. Instead of one very large plume, there would be a group of smaller plumes under Tharsis, each feeding one of the main volcanoes. Such plumes have been modeled as stable over billions of years and ongoing melt production at their centers would explain the continued volcanic activity over this time period, even to the present-day Li and Kiefer [53].

3.2 Methods

We model the Martian mantle using a modified version of the finite element geodynamics code CitcomS [93, 108, 109]. The solid mantle behaves as an extremely viscous fluid over long timescales, which is modeled as a creeping flow. CitcomS solves the following nondimensionalized equations for the conservation of mass, momentum, and energy, respectively:

$$\nabla \cdot \mathbf{u} = 0 \tag{3.1}$$

$$-\nabla P + \nabla \cdot \left[\eta \left(\nabla \mathbf{u} + \nabla^T \mathbf{u}\right)\right] + RaT\mathbf{e}_r = 0 \tag{3.2}$$

$$\frac{\partial T}{\partial t} + \mathbf{u} \cdot \nabla T = \nabla^2 T + Q \tag{3.3}$$

where $\mathbf{u}$ is the velocity, P is the pressure, η is the viscosity (temperature-dependent Newtonian), T is the temperature, $\mathbf{e}_r$ is the unit vector in the radial direction, and Q is an internal heat source (and/or sink). Ra is the Rayleigh number given by

$$Ra = \frac{\rho_m g \alpha \Delta T R^3}{\kappa \eta_0} \tag{3.4}$$

where ρ_m is the average mantle density, g is the gravitational acceleration, α is the coefficient of thermal expansion, ΔT is the initial super-adiabatic temperature difference across the mantle, R is the planet's radius, κ is the thermal diffusivity, and η_0 is the mantle reference viscosity. Table 3.1 shows the values we use for these and other parameters. An important note here for comparing CitcomS results with other work is that the Rayleigh number is usually defined by a layer thickness D, however CitcomS uses R for the length scale instead. For efficiency, CitcomS computations are parallelized [93]. We model incompressible flow using the Boussinesq approximation.

Table 3.1: Summary of parameters and initial conditions used in our models.

Parameter	**Value**
Mean radius	3.3895×10^6 m
Core radius	1.830×10^6 m
Mean mantle density	$3500\,\mathrm{kg\,m^{-3}}$
Gravitational acceleration (g)	$3.72\,\mathrm{m\,s^{-2}}$
Reference viscosity (η_0)	1.0×10^{21} Pa s
Activation energy (E*)	$117\,\mathrm{kJ\,mol^{-1}}$ (n=3)
	$350\,\mathrm{kJ\,mol^{-1}}$ (n=1)
Activation volume (V*)	$6.6\,\mathrm{cm^3\,mol^{-1}}$
Rayleigh number (Ra), mantle thickness*	1.4296×10^7
Thermal expansivity (α)	$2 \times 10^{-5}\,\mathrm{K^{-1}}$
Thermal diffusivity (κ)	$1 \times 10^{-6}\,\mathrm{m^2\,s^{-1}}$
Specific heat capacity (c_P)	$1.25 \times 10^3\,\mathrm{J\,kg^{-1}\,K^{-1}}$
Mantle adiabat	$0.15\,\mathrm{K\,km^{-1}}$
Surface Temperature (T_s)	220 K
Temperature difference (ΔT)	1500 K
Initial mantle temperature**	1720 K
Initial CMB temperature**	172 K (1.0 ΔT)
	1870 K (1.1 ΔT)
	2020 K (1.2 ΔT)
Crustal HPE enrichment factor	5x
	10x
	15x

* Rescaled because CitcomS uses radius instead of mantle thickess for its Ra
** Potential temperature–excludes adiabat

We have made several changes and additions to the CitcomS code. The original code keeps mantle internal heating constant through time. However, because heat production results from the decay of radioisotopes, it is more realistic to have it decrease accordingly using the calculations described by Turcotte and Schubert [97]. Crustal enrichment of radioisotopes has also been added. We have incorporated the cooling of the planet's core, which is treated based on the coupled core and mantle thermal evolution model developed by Stevenson

et al. [89] As the core cools, the heat from the core heats the mantle from below, while the core-mantle boundary (CMB) temperature decreases.

3.2.1 Melt production

The largest modification to CitcomS is the incorporation of melting calculations. Much of the work on melting in Mars' mantle [41, 43, 53, 78] was performed in 2D spherical axisymmetric geometry (or 2D Cartesian in the case of Tosi et al. [95]) rather than 3D. With the exception of Ruedas et al. [78], these also do not consider the decrease in radioisotope abundances through time or the thermodynamics of core cooling and solidification. Spherical 3D modeling incorporating decaying heating as well as crustal enrichment of radioisotopes has become more common over the past few years [72, 73, 80]. Because the melting formulation is new to CitcomS, we describe it in some detail below.

The first step in melt calculations is to calculate the equilibrium melt fraction, which for a given composition is a function of temperature and pressure. We calculate melt fraction (by mass) using the empirically derived parameterization of Katz et al. [38] for dry peridotite melting at upper mantle pressures. We convert this mass fraction to a volume fraction given the solid mantle density (herein $3500\,\mathrm{kg\,m^{-3}}$) and the presumed melt density ($3000\,\mathrm{kg\,m^{-3}}$). The melt fraction algorithm of Katz et al. [38] was developed by fitting experimental data on equilibrium melting of peridotite and is valid up to approximately 8 GPa. Katz et al. [38] has since found broad application in geodynamic mantle convection codes such as CitcomS (e.g., Citron et al. [18], Šrámek and Zhong [85]), as well as ASPECT and adaptations thereof (e.g., Dannberg and Heister [19], Ninju et al. [66, 67]). While Katz et al. [38] was originally published with terrestrial melting in mind, it has been applied to calculate melt productivity in convection models of the Martian mantle by Citron et al. [18], Kiefer and Li [43], and

Šrámek and Zhong [85]. According to Šrámek and Zhong [85] and Kiefer and Li [43], the Katz et al. [38] solidus is close to experimentally derived Mars solidi, such as those of Agee and Draper [2], Bertka and Holloway [9], Matsukage et al. [56], using inferred Martian mantle compositions. The utility of Katz et al. [38] is that it includes a solidus, liquidus, and a relatively straightforward nonlinear way to calculate melt fraction. Earlier geodynamic modeling employed simpler methods, such as Kiefer [41] linearly increasing melt fraction between the solidus and assuming the liquidus is a fixed temperature above the solidus.

We use the liquidus and lherzolite liquidus of Katz et al. [38] for dry peridotite. However, we replace their solidus with that of Duncan et al. [21]. The Katz et al. [38] solidus in degrees Celsius as a function of pressure P in GPa, 1085.7 + 132.9 P - 5.1 P^2, is higher than the Mars solidus of Duncan et al. [21], 1088 + 120.2 P – 4.877 P^2, which is 45°C cooler at 4 GPa and 85°C cooler at 8 GPa (see Figure 3.2).

Melt production computations must consider not only the portion of a region that is molten (melt fraction), but also the movement of the mantle material through the melting region. Based on equation B1 of Watson and McKenzie [101], $\dot{M}$, the instantaneous mass of melt per unit mass of mantle material produced per unit time, is the material derivative of the equilibrium melt fraction X.

$$\dot{M} = \frac{DX}{Dt} = \frac{\partial X}{\partial t} + \mathbf{u} \cdot \nabla X \tag{3.5}$$

Using the chain rule, $\dot{M}$ can be written in terms of the partial derivatives of melt fraction with respect to temperature and pressure.

$$\dot{M} = \frac{DX}{Dt} = \frac{\partial X}{\partial T}\frac{DT}{Dt} + \frac{\partial X}{\partial P}\frac{DP}{DT} = \frac{\partial X}{\partial T}\left(\frac{\partial T}{\partial t} + \mathbf{u} \cdot \nabla T\right) + \frac{\partial X}{\partial P}\left(\frac{\partial P}{\partial t} + \mathbf{u} \cdot \nabla P\right) \tag{3.6}$$

Assuming $\partial P/\partial t$ is zero and pressure is hydrostatic, then

$$\dot{M} = \frac{\partial X}{\partial T}\left(\frac{\partial T}{\partial t} + \mathbf{u}\cdot\nabla T\right) - \frac{\partial X}{\partial P}\bar{\rho} g u_r \tag{3.7}$$

where u_r is the radial component of velocity, and $\bar{\rho}$ is the radial profile of density. The volume of melt produced is calculated by integrating $\dot{M}$ over the element volumes using Gaussian quadrature.

3.2.2 Model cases

Rheology

We start by modeling a structural reference case, without the dichotomy. We ran 18 models with this reference structure, testing three values each for the initial CMB temperature and crustal HPE enrichment, and two values for the activation energy (E*). Based on Christense [16], activation energy is divided by the stress exponent n to approximate a power law rheology for olivine. Typically n is taken to be 3, but we vary the effective activation energy, corresponding to testing values of n=3 (dislocation creep) and n=1 (diffusion creep). Thus to approximate n=3, the nominal activation energy of $350\,\mathrm{kJ\,mol^{-1}}$ becomes $117\,\mathrm{kJ\,mol^{-1}}$ ("lower activation energy" cases), while for n=1, we keep the activation as $350\,\mathrm{kJ\,mol^{-1}}$ ("higher activation energy" cases).

The temperature and pressure (depth) dependent viscosity η is given, in dimensional form, by

$$\eta = A\cdot\eta_0\cdot\exp\left(\frac{E_a + PV_a}{RT} - \frac{E_a + PV_a}{R(\Delta T + T_s)}\right) \tag{3.8}$$

where η_0 is is the reference viscosity (1.0×10^{21} Pa s), E_a is the activation energy (either 117 or 350 kJ mol^{-1}), P is the pressure, V_a is the activation volume (6.6 cm^3 mol^{-1}), R is the ideal gas constant, and T is the absolute potential temperature. The pre-exponential factor A is to control the viscosity by layer. To enforce a strong (initially 100 km thick) lithosphere, from the surface to 100 km depth, A = 10. From 100 km to 1000 km depth, A = 0.1, establishing a weak asthenosphere. From 1000 km depth to the CMB, A = 10, accounting for a strong transition zone rheology.

Temperature initial condition

The initial temperature profile uses CitcomS tic_method=12, where the mantle is set to the same temperature T_m (here, ΔT = 1500K) everywhere, then cold and hot thermal boundary layers are added at the top and bottom, respectively. Small magnitude (0.01 ΔT) spherical harmonic degree 8, order 6 perturbations are added at all layers to initiate convection. The boundary layer temperatures are calculated by adjusting T_m based on 1D conductive cooling (at the top) or heating (bottom) of a half-space after a "half-space age". The top boundary layer is thus achieved by adjusting the constant temperate profile according to:

$$T(r) = T_m - (T_m - T_{surf}) \cdot \mathrm{erf}\left(\frac{R-r}{2\sqrt{(a)}}\right) \tag{3.9}$$

and similarly the bottom boundary layer is created by

$$T(r) = T_m + (T_{cmb} - T_m) \cdot \mathrm{erf}\left(\frac{r-r_{cmb}}{2\sqrt{(a)}}\right) \tag{3.10}$$

where $T(r)$ is the initial temperature at radius r, T_{surf} is the surface temperature (220 K), T_{cmb} is the initial CMB temperature, R is the radius of the planet (3389.5 km), r_{cmb} is the

radius of the CMB, and a is the conductive cooling/heating age of the half-space. For all 18 reference structure cases (both low an high activation energy), The initial error function temperature profile, with top and bottom boundary layers, is based on a half-space age of 100 Myr.

Dichotomy

We repeat the range of nine high activation energy (n=1) cases (3 crustal enrichments, 3 initial CMB temperatures) for models with a degree-1 hemispheric dichotomy structure (boundary along the equator). The initial error function temperature profile in the southern hemisphere is based on a thermal half-space age of 500 Myr. The initial temperature profile in the northern hemisphere is based on a thermal age of 100 Myr, as would result from the dichotomy-forming impact resetting the temperature profile ∼400 Myr after Mars formed. The initial southern hemisphere lithosphere is correspondingly set 100 km thicker than the northern hemisphere lithosphere by setting the viscosity in the lid to the maximum allowed value (as applied when truncating very high viscosities), which for our models is $10^5\eta_0 = 1 \times 10^{26}\,\mathrm{Pa\,s}$.

3.3 Results

Of the three parameters we varied (activation energy/stress exponent, crustal HPE enrichment, and initial CMB temperature), the results are generally most sensitive to the activation energy, and least sensitive to the CMB temperature. Therefore, the plots in the figures are grouped first by activation energy, specifically by the value of the stress exponent n that the nominal activation energy ($350\ \mathrm{kJ\,mol^{-1}}$) is divided by in order to vary the effective activation energy. Above the bottom thermal boundary layer, the mean mantle temperatures and

mean radial temperature profiles (geotherms) are not strongly influenced by the initial CMB temperature. Higher activation energy and, to a lesser degree, lower crustal enrichment and the the thicker southern lithosphere of the dichotomy cases, lead to a overall hotter mantle. However, these higher activation energies, and thus higher temperatures in the mid-lower mantle, are reached with a thicker upper thermal boundary layer. As a consequence of the higher average temperatures they produce, lower enrichment and higher activation energy lead to more melt being produced for longer, in many cases nearly to the present day. Melting occurs primarily in the middle of the heads of plumes or the linear upwellings like those in Figure 3.5 (d) and (e).

Across all 27 cases, the mean present-day surface heat flux only ranges from 12.3 $\mathrm{mW\,m^{-2}}$ (high activation energy, enrichment = 5x, initial T_{CMB} = 1720 K) to 14.1 $\mathrm{mW\,m^{-2}}$ (low activation energy, enrichment = 5x, initial T_{CMB} = 2020 K). Of note, these values are only about half of the heat fluxes modeled by Plesa et al. [71] and Plesa et al. [72]. Our mean surface heat fluxes correlate positively with initial CMB temperature, and negatively with activation energy. For high activation energy, the fluxes also increase with crustal enrichment, but curiously for low activation energy, the minimum surface heat flux occurs with 10x enrichment across all three initial CMB temperatures.

3.3.1 Mantle temperature and geotherms

Figure 3.3 (a–c) shows the mean potential temperature profiles, or geotherms, at the time corresponding to present day for all the models, in three separate plots according to the rheology (reference n=3 low activation energy, reference n=1 high activation energy, and dichotomy n=1 high activation energy). On each of these three plots, the 1605 ± 100 K mid-mantle temperature from Huang et al. [34] is marked by the vertical magenta lines, with the

minimum and maximum dashed. The range of geotherms from the models of Smrekar et al. [81] is shaded, with the lighter shading being below the mean, and the darker shading above it. All the low activation energy geotherms fall several hundred kelvins below both Huang et al. [34] and Smrekar et al. [81]. The mid-mantle temperatures for all high activation energy cases, including those with the dichotomy, plot within the range of Huang et al. [34]. The 5x and 10x enrichment cases also fall within the range of Smrekar et al. [81], as do the 15x cases at depths less than ∼750 km. Our geotherms, not unlike Huang et al. [34], are generally on the cooler side of the range of Smrekar et al. [81], although they have a somewhat different shape such that the for depths between ∼100 and ∼500 km, the high activation energy cases with 5x and 10x enrichment rise above the mean of Smrekar et al. [81].

The time evolution of the mean mantle potential temperature is likewise plotted in Figure 3.3 (d–f). The cases with lower crustal enrichment, that is those which retain more of the HPE in the mantle, heat up over the first few hundred million years as a result of this radiogenic heat. With the low activation energy rheology, this effect is only notable with the 5x enrichment, and even then very subtle. For high activation energy, this occurs with similar subtlety in the 10x cases, albeit stretched out over a longer time so that the peak temperature is later. Whereas the temperature increase with 5x enrichment is more pronounced and the peak ∼200-300 Myr later, which would be near the beginning of the Hesperian. With adding the dichotomy, the timing of the peak temperature is later still at about 3200 Ma, well into what would be the Hesperian.

3.3.2 Geoids

The power spectra (from spherical harmonic degree l=2-20) of the present-day geoids output by our models are plotted in Figure 3.4. Each subplot also shows, in blue, the power spectrum of the observed Martian geoid with the effect of Tharsis' low degree ($l \leq 6$) topography removed, as determined by Zuber and Smith [110]. In terms of matching this "Mars without Tharsis" geoid, the 5x enrichment cases, as well as the dichotomy case with 10x enrichment, perform the worst, having significantly less power at all degrees. In contrast, the low activation energy, 15x enrichment cases show a remarkably good fit to Zuber and Smith [110]. The remaining cases are mediocre in matching Mars without Tharsis. The low activation energy, 10x enrichment cases, and the dichotomy 15x enrichment case with the coolest (initially 1720K) CMB, simply fall between the worst performing cases and the Mars without Tharsis spectrum. The high activation energy 10x and 15x enrichment cases, as well as the two warmer CMB dichotomy 15x enrichment cases, match Mars without Tharsis up to l=6, but still have significantly less power than it at higher degrees.

3.3.3 3D Mantle Structure Evolution

All of the models develop long-lived plumes or plume-like linear upwellings. The cases without the dichotomy, both for low and high activation energies, tend to first develop a convection pattern dominated by degree-2, with two large antipodal plumes, but connected by a less prominent linear upwelling (Figure 3.5 (a, b)). This pattern gradually evolves into a persistent pattern dominated by a single linear upwelling that curves around much of planet–in some cases encircling it as a sinuous ring (Figure 3.5 (d, e, g, h)). When the upwelling remains discontinuous, one or both ends of the linear upwelling are warmer, with a broader head, where there is greater melting (Figure 3.5 (d, g)). The dichotomy models

behave very differently. Within a few hundred million years they develop a degree-1 structure comprising a single large plume centered on the pole of the northern hemisphere–the one with thinner lithosphere and the warmer (younger) half-space initial temperature profile. Unlike the initially imposed step in lithospheric thickness–which gradually smooths out–this degree-1 convection pattern persists through present-day; although the plume becomes less vigorous as it, like the mantle as a whole, cools.

3.3.4 Melting

The total amount of melt over time, represented as the fraction of the mantle's volume that is molten (e.g., 0.1 = 10% of the mantle is melt) plotted in Figure 3.6 (a-e). This bulk melt fraction generally follows the trend of the mean mantle temperature, peaking after a few hundred million years, and then declining over the rest of the model run. The low activation energy cases, and the high activation energy cases with 10-15x enrichment and a cooler CMB, do tend to have an additional, earlier peak within the first 100 Myr, in some cases at the initial time step. In the cases with 15x enrichment and the initial CMB temperature of 1720 K, there is only this one early peak, corresponding with the rising of plumes.

The melt fraction in all models peaks with the mantle being at least several percent melt, with the 5x enrichment cases reaching bulk melt fractions well over 10%. All melting in our models occurs within a relatively narrow range of pressures/depths (2.6-4 GPa / ∼200–300 km) in the upper mantle, and the local melt percentages here can reach in excess of 40-50% by volume. The bulk melt fraction steadily drops after the early peak so that by ∼2000 Ma in the low activation energy cases and by ∼500-1000 Ma in the high activation energy cases, there is no discernible melt on the linear scales of Figure 3.6 (a–c). But this is in part misleading; a small mount of melt remains, in many cases persisting up to or near the present

day, and this is more visible when the bulk melt fraction is plotted on a logarithmic scale as in Figure 3.6 (d–f). The overall amount of melt produced is not significantly affected by adding the dichotomy to the high activation energy cases, though it is marginally reduced.

The cases with low activation energy show much less spread in their melt production over time than the high activation energy cases when varying the enrichment and initial CMB temperature. Put another way, models with high activation energy are more sensitive to changes in the other parameters we varied. The coldest (15x enrichment) high activation energy models produce less melt through time than even the coldest low activation energy models, while the hottest (5x enrichment) high activation energy cases produce more melt than all of the low activation energy models. Each 5x and 10x enrichment case produces a melt volume within or above the nominal volume of the Tharsis rise (lighter gray shading in Figure 3.6, as does the low activation energy 15x enrichment case with the hottest (initially 2020 K) CMB. Yet, only the single warmest case of all 27 cases–the high activation energy reference case model with 5x enrichment and the hottest (initially 2020 K) CMB–produces enough melt for Tharsis when accounting for limited extraction of mantle melt to the surface (darker shading in Figure 3.6).

Even on the logarithmic scale, the time of last melting is not clear from Figure 3.6, because the latest bulk melt fraction is more than 10 orders of magnitude lower than the peak. The precise model time and corresponding age of last melt production for each model case is listed in Table 3.2. Many cases are still producing melt at the end of the run, at present-day, and in others melting has only cut off within the past few hundred million years. These tend to be the lower enrichment cases. In all of the reference 15x enrichment cases, melting shuts off well over 1 Ga. Melt continues for longer in the dichotomy 15x enrichment cases, even up to present day in the case of the hottest (initially 2020 K) CMB. Still not clear from either Figure 3.6 or Table 3.2 is that several models, mostly 10x enrichment cases, see melt

production stop and restart one or more times before finally ending, or reaching present-day with melt present. These last trickles of melting are very small and localized.

3.4 Discussion

Of the three parameters varied (rheology, crustal HPE enrichment, and initial CMB temperature), the results are most sensitive to the activation energy. The results are least sensitive to the initial CMB temperature. Higher activation energies, and thus higher temperatures in the mid-lower mantle, result in a cooler and thicker lid, but also an overall hotter mantle. Corresponding with the higher average temperatures, lower enrichment and higher activation energy lead to more melt being produced for longer. The cases with a hotter CMB, and a cooler mantle due to lower concentrations of HPEs (higher crustal enrichment) are more influenced by bottom heating. In these cases, more vigorous plumes that rise at the beginning of the model run contribute more directly to the melting.

The results summarized and color coded in Figure 3.7 show whether each of our 27 model cases fits our constraints for (1) geotherms consistent with InSight results, (2) recent production of melt, (3) sufficient melt to produce Tharsis, and (4) matching the Mars without Tharsis geoid. Blue indicates the constraint was satisfied, and red that it was decisively not satisfied. Purple indicates an inconclusive or intermediate result that we consider to partially satisfy the constraint. (See 3.7 caption for precisely what the colors mean.) Figure 3.7 depicts somewhat of a dilemma as to which models are the best overall. With regard to geotherms and melting, we find the high activation energy (n=1) cases with 5-10x enrichment to be more consistent with our expectations for Mars than the low activation energy

Table 3.2: Model time and age of last melt production. The reference cases are taken to start at 4.5 Ga, while Dichotomy cases are taken start 400 Myr later, at 4.1 Ga.

Rheology	**Enrichment**	$\mathbf{T}_{CMB}$	**Model time**	**Age BP**
Reference n=3	5x	1.0ΔT	4500 Myr	0 Ma
Reference n=3	5x	1.1ΔT	4483 Myr	17 Ma
Reference n=3	5x	1.2ΔT	4500 Myr	0 Ma
Reference n=3	10x	1.0ΔT	3154 Myr	1346 Ma
Reference n=3	10x	1.1ΔT	3615 Myr	884 Ma
Reference n=3	10x	1.2ΔT	4142 Myr	358 Ma
Reference n=3	15x	1.0ΔT	2105 Myr	2395 Ma
Reference n=3	15x	1.1ΔT	3129 Myr	1371 Ma
Reference n=3	15x	1.2ΔT	2560 Myr	1940 Ma
Reference n=1	5x	1.0ΔT	4500 Myr	0 Ma
Reference n=1	5x	1.1ΔT	4500 Myr	0 Ma
Reference n=1	5x	1.2ΔT	4500 Myr	0 Ma
Reference n=1	10x	1.0ΔT	3756 Myr	744 Ma
Reference n=1	10x	1.1ΔT	4500 Myr	0 Ma
Reference n=1	10x	1.2ΔT	4354 Myr	146 Ma
Reference n=1	15x	1.0ΔT	2080 Myr	2420 Ma
Reference n=1	15x	1.1ΔT	3785 Myr	715 Ma
Reference n=1	15x	1.2ΔT	4229 Myr	271 Ma
Dichotomy n=1	5x	1.0ΔT	4100 Myr	0 Ma
Dichotomy n=1	5x	1.1ΔT	4100 Myr	0 Ma
Dichotomy n=1	5x	1.2ΔT	4100 Myr	0 Ma
Dichotomy n=1	10x	1.0ΔT	4100 Myr	0 Ma
Dichotomy n=1	10x	1.1ΔT	4100 Myr	0 Ma
Dichotomy n=1	10x	1.2ΔT	4100 Myr	0 Ma
Dichotomy n=1	15x	1.0ΔT	3028 Myr	1072 Ma
Dichotomy n=1	15x	1.1ΔT	3210 Myr	890 Ma
Dichotomy n=1	15x	1.2ΔT	4100 Myr	0 Ma

cases. In contrast, the geoids of the low activation energy (n=3), 15x enrichment cases are the best fit to Mars without Tharsis.

Many of our models produce a small amount of melt up to or near present-day, with some cases having small amounts of melting stopping and restarting. This is consistent with small, localized pulses of volcanism on Mars within the past few million to ∼100 million years. It should be noted that our models have limited resolution, for example ∼25 km vertical resolution, and still lower in the lateral direction over most of the mantle, including the 200-300 km melting depths. Therefore, it is possible that were these same parameters and initial conditions run at a significantly higher resolution–which would take an infeasible amount of computing time and power–melting could continue for a little longer, and would not stop and restart.

Producing sufficient melt for Tharsis while also producing a geoid power spectrum that is consistent with present-day Mars (without the volcanically constructed topography of Tharsis) is very difficult, and none of our cases do that well. It is even difficult just to produce enough melt to account for the enormous volume of Tharsis, while also accounting for the fact that only a small fraction of melt produced in the mantle erupts on the surface. As depicted in Figure 3.7, only our single hottest case (high activation energy, 5x enrichment, 2020 K initial CMB temperature) does this–and then only barely. This singular case still does not do so quickly enough to allow for emplacement of the Tharsis rise by the late Noachian, and it also produces a geoid inconsistent with out constraint. The majority of cases–and every case with 5-10x enrichment–produce at least a Tharsis-equivalent melt volume within the mantle, but this could only account for Tharsis if an unreasonably high percentage of that melt were erupted onto the surface. Even the two low activation energy, 15x enrichment cases that do this much and reproduce the expected geoid power spectrum have unacceptably cold geotherms and stopped producing melt well over 1 Ga.

We find the thermal structure results from models with high activation energy to be more consistent with present day Mars. The model cases (high activation energy and 5x enrichment) that perform the best in terms of total melt production and maintaining some melt to present-day–and thus in terms of temperature–are some of the worst performing in terms of matching the expected geoid. The three best performing cases (low activation energy and 15x enrichment) for reproducing the expected geoid are not only the worst performing with regard to melting, but result in present-day mantle temperatures hundreds of degrees colder than inferred from the results of InSight and previous modeling. It is, however, remarkable that despite the cold mean geotherms, the 5x enrichment cases with this low activation energy rheology are able to locally produce small volumes of melt up to or near present-day. The large discrepancy in geotherms does lead us to broadly reject the low activation energy rheology, so much so that this was not considered when modeling the dichotomy–but the better fitting geoid remains an interesting question.

With regard to crustal HPE enrichment, and rather unsurprisingly, Figure 3.7 also reflects how the melting results favor lower crustal enrichment, which is somewhat at odds with the body of work favoring 10-15x enrichment–as well as the the geoid power spectra of our models. Nevertheless, most of the 10x cases with high activation energy produce melt up to or near present-day, and up to about l=6 the geoid is a good fit with Mars without Tharsis. The 10x enrichment cases do produce significantly less melt overall, and early on, compared to the 5x cases. But even the 5x enrichment cases cannot produce enough melt, at least not quickly enough, to account for Tharsis without extremely efficient melt extraction. In case of either 5x or 10x enrichment some change or additional factor must be considered to account for all of the melt erupted to form Tharsis and other major volcanic regions.

The present day geotherms from the low activation energy cases are hundreds of degrees too cold to be consistent with what has been inferred for Mars, therefore we generally prefer

the models with the higher activation energy. Nevertheless, the models with low activation energy and 15x enrichment provide the best-fitting geoid to observations. The power spectra for the 10x and 15x enrichment, high activation energy cases do still match well with the Mars without Tharsis geoid up to l=6–8. Only at higher degrees is there significantly less power in the geoid for these cases compared to Mars without Tharsis, and the low activation energy 15x enrichment cases.

We do not consider in our modeling initial conditions arising from a magma ocean overturn [22, 23]. One might speculate that this would stabilize the mantle with regard to convection for some period of time, allowing the mantle to heat up. The interaction of the two effects of (1) cooling the mantle due to the overturn, and (2) the subsequent heating of the mantle due to stabilizing the mantle against convection, make it difficult to predict the impact of this condition without further analysis. That is beyond the scope of this work.

3.4.1 Effects of adding the dichotomy

Because of the large mismatch in geotherms with the low activation energy cases, and the associated difficulty in generating sufficient melt, we only ran the dichotomy cases with high activation energy. To first order, the geotherms of the dichotomy cases are very close to those of the corresponding cases without the dichotomy. In the long term, the mantle temperature is much more sensitive to crustal enrichment than it is to the initially thicker southern lithosphere and warmer northern hemisphere mantle.

Recall that the initial temperature profile is also different with the dichotomy cases. The start time is taken to be 4100 Ma instead of 4500 Ma as in the reference cases. To account for this difference in time, we initialize the southern hemisphere with an error function temperature profile corresponding to an age of 400 Ma (versus 100 Ma for the reference

case). The northern hemisphere initial condition is kept as a profile corresponding to an age of 100 Ma, consistent with a younger lithosphere and a large injection of heat from the putative large impactor responsible for the dichotomy (Andrews-Hanna et al. [4], Kiefer [42], Marinova et al. [55]).

The geoid power spectra produced by the dichotomy are an even poorer match to Mars without Tharsis than the reference high activation energy cases. The fit improves with increasing enrichment, so with higher enrichments of $\geq$20%, one may extrapolate that the fit would be more reasonable, but such enrichment levels are not supported by any other work, or the rest of our results. Including the hemispheric dichotomy for the high activation energy cases as we did makes the geoid fit even wore than the reference high activation energy cases, and it marginally decreases the cumulative melt production. However, the initially thicker southern lithosphere does make it easier to maintain a small amount of melt close to present-day, and this is not wholly attributable to the later start time with the same initial temperature profile in the northern hemisphere.

3.5 Conclusions

Overall, we find that our results from the high activation energy rheology reference cases (i.e., without the dichotomy), 5-10x crustal enrichment, and initial CMB temperature of 1870-2020 K (i.e., greater than the initial mid-mantle temperature) are most consistent with the data we have for Mars. The present-day geotherms from our model cases with the high activation energy are consistent with Huang et al. [34] in supporting a present-day mantle cooler than most pre-mission estimates by Smrekar et al. [81]. A 10x crustal enrichment factor would also be consistent with the modeling of Samuel et al. [79] and the lower end of the range inferred by Huang et al. [34]. Furthermore, 10x enrichment agrees well with

the orbital gamma ray spectrometry data that indicate ∼50% of Mars' HPE are contained within its crust [11, 58, 94]. Modifying the radial viscosity structure of these 5-10x enrichment models may resolve the inconsistency with Zuber and Smith [110] of our preferred cases. To be sure, up to l = 6, the 10x enrichment geoids for the high activation energy reference structure are in good agreement with Zuber and Smith [110].

It is challenging to reconcile such a cool mantle at present with the amount of melting required throughout–and particularly early on in–Martian history. It is nevertheless reassuring that our models, and thus a mantle as cool as Huang et al. [34] find for present-day Mars, are still capable of producing small, localized amounts of melt, as the evidence of recent volcanism [7, 33, 36, 63, 90, 100] necessitates, and the ongoing tectonic activity in Elysium observed by InSight [12, 44, 68, 87] suggests. Melt production is very sensitive to the temperature, or more precisely the portion of the mantle that is above the solidus. Therefore more melt in the late pre-Noachian to early Hesperian, as is necessary to produce the Tharsis and Elysium rises, requires a hotter mantle and/or a lower solidus. A hotter mantle would have to cool more quickly in order to still reach the cool observed geotherms. The faster cooling of a hotter mantle may be facilitated by the consequently more vigorous convection, and considering the effect of compressible convection and, in particular, the latent heat of melting. Alternatively, or in addition to this, including the effect of water or CO_2 could depress the solidus enough to significantly increase melt production at a given temperature.

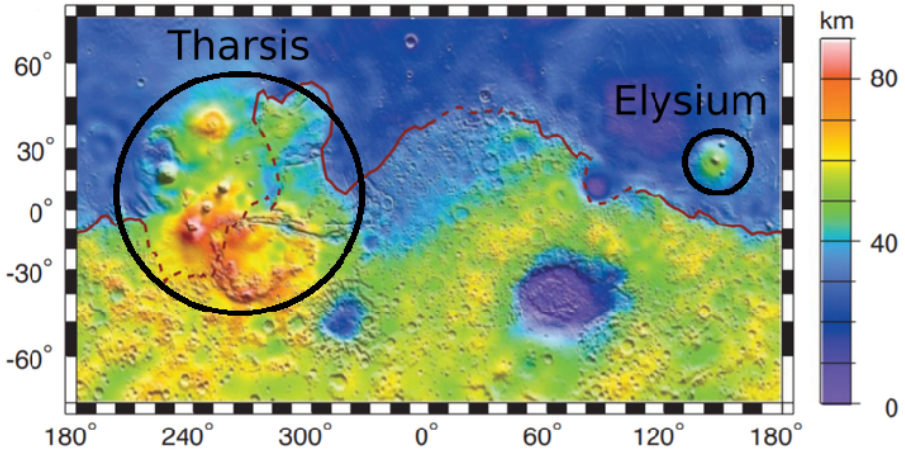

Figure 3.1: Crustal thickness map adapted from Zuber et al. [111]. The locations and approximate extent of Tharsis and Elysium are marked. The red line marks the dichotomy boundary. The line is dashed where the boundary is uncertain, in particular beneath Tharsis.

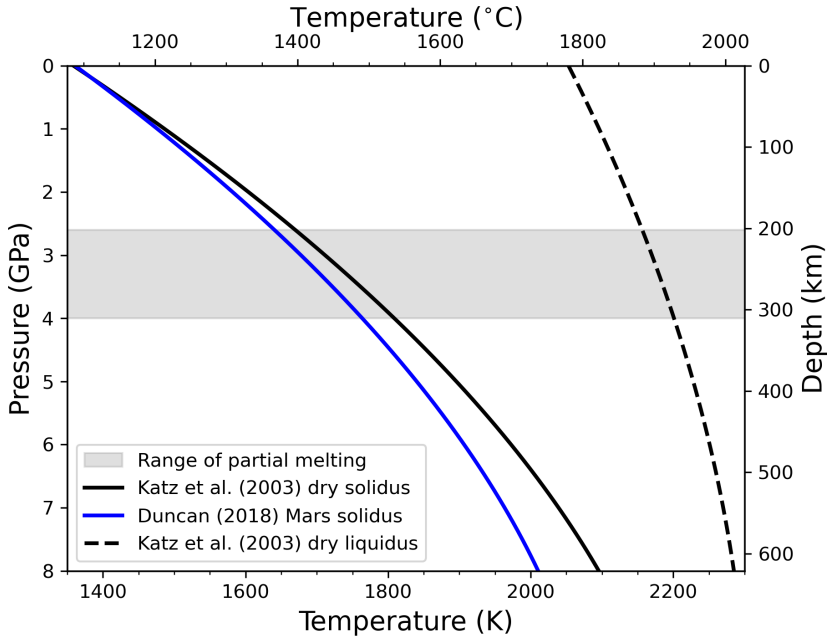

Figure 3.2: Comparison of the Katz et al. [38] solidus for dry peridotite with the Mars solidus of Duncan et al. [21] over the applicable depth range of Katz et al. [38]. The liquidus of Katz et al. [38] is also plotted. Melting in our models is confined to a narrow range of pressures between 2.6 and 4 GPa, or approximately 200–300 km depth.

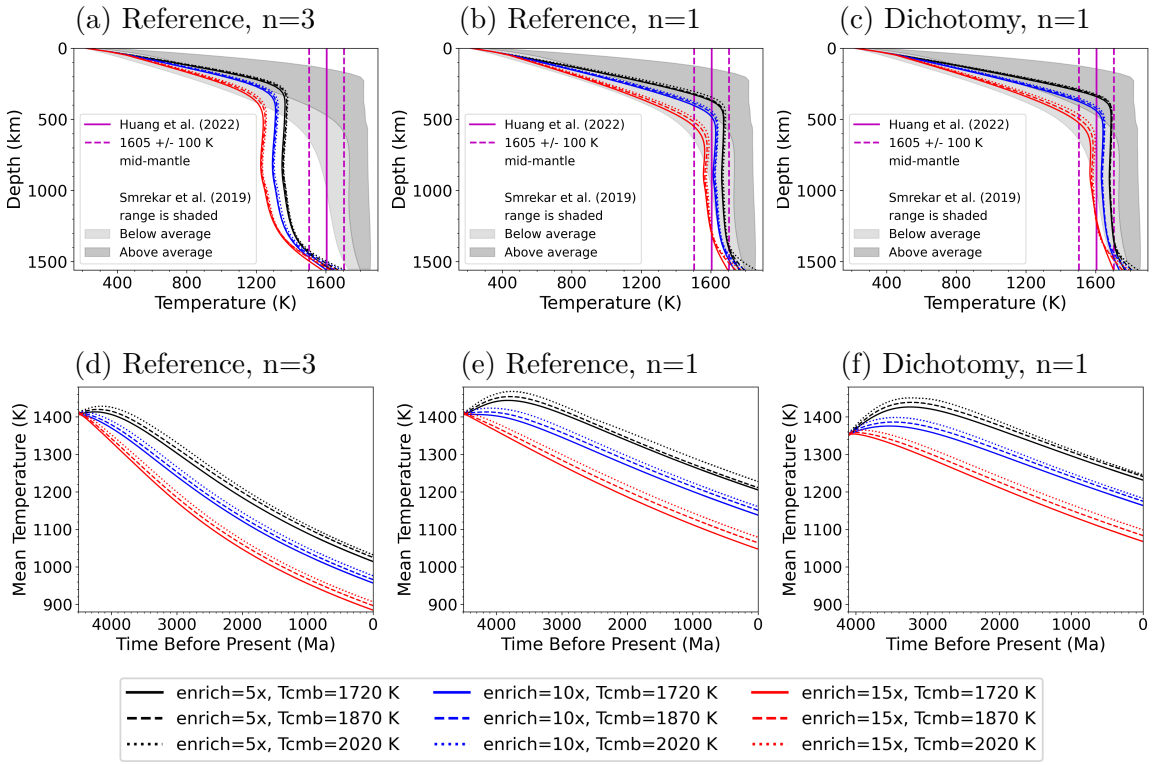

Figure 3.3: a-c: Present-day geotherms, including the InSight derived mid-mantle temperature estimate of 1605 ± 100 K by Huang et al. [34] (vertical magenta lines), as well as the range of possible geotherms from Smrekar et al. [81] (shaded).

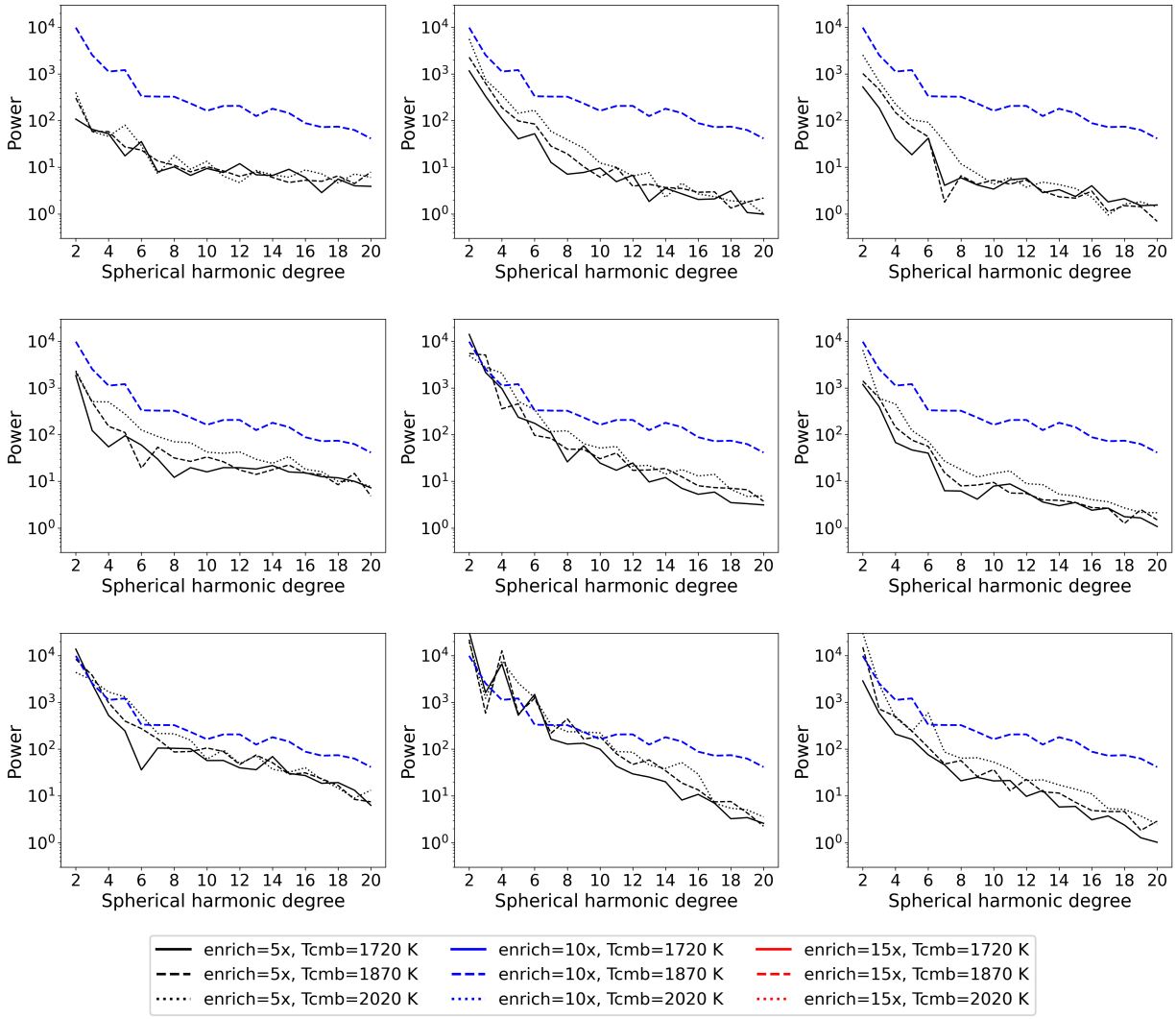

Figure 3.4: Geoid power spectra compared to Mars without Tharsis coefficients from Zuber and Smith (1997). Begins at l=2.

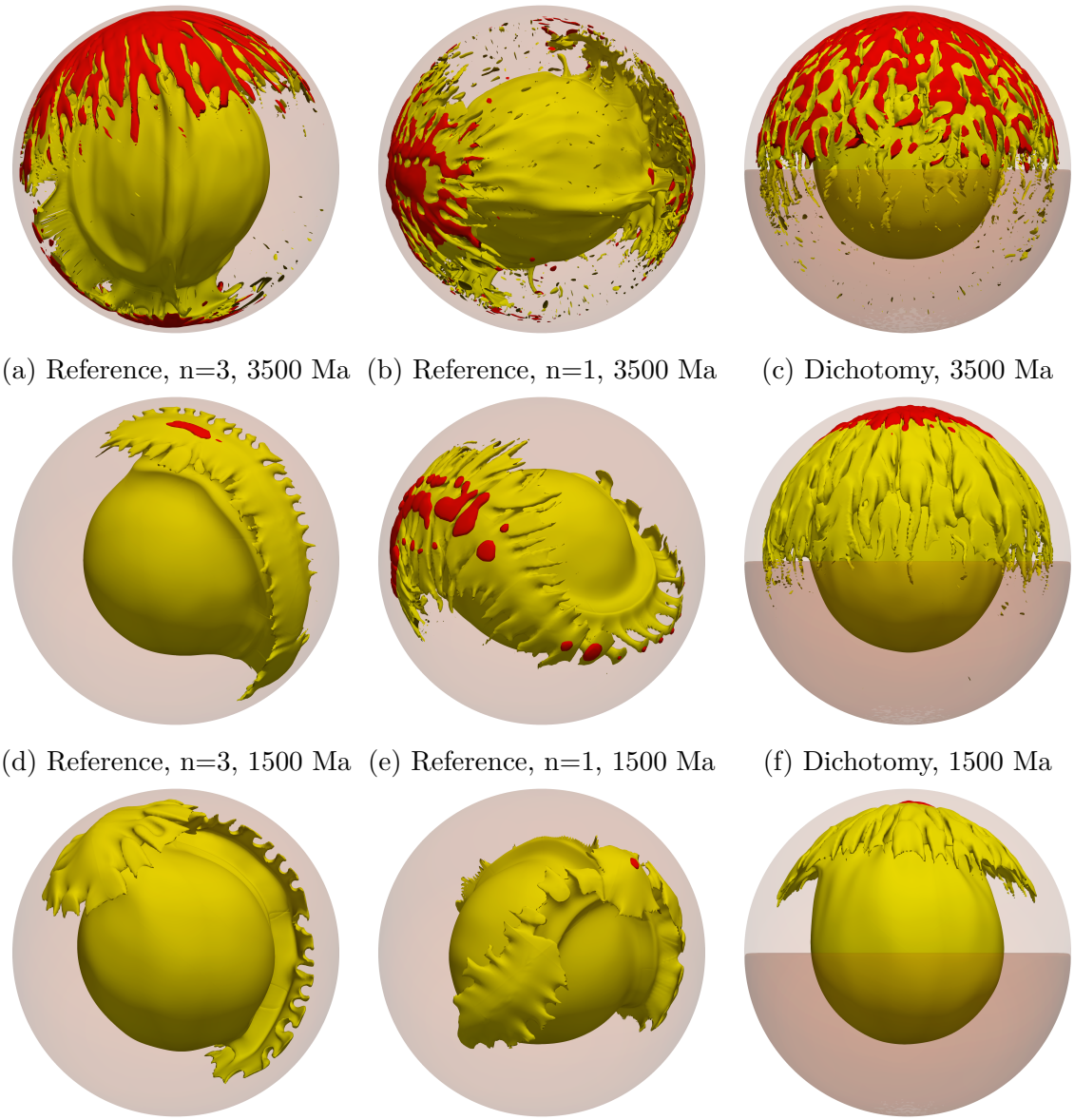

(a) Reference, n=3, 3500 Ma (b) Reference, n=1, 3500 Ma (c) Dichotomy, 3500 Ma

(d) Reference, n=3, 1500 Ma (e) Reference, n=1, 1500 Ma (f) Dichotomy, 1500 Ma

(g) Reference, n=3, Present (h) Reference, n=1, Present (i) Dichotomy, Present

Figure 3.5: 3D plots of selected model cases with potential temperature (yellow) and melt (red) isosurfaces for all three (reference n=3, reference n=1, and dichotomy n=1) cases with 10x enrichment and initial T_{CMB} of 1.1 ΔT = 1870 K. The isotherms and melt fractions plotted for each case are: (a) T = 1650 K, melt fraction = 10%; (b) T = 1770 K, melt fraction = 25%; (c) T = 1755 K, melt fraction = 25%; (d) T = 1500 K, melt fraction = 0.01%; (e) T = 1710 K, melt fraction = 0.1%; (f) T = 1710 K, melt fraction = 1%; (g) T = 1380 K, no melt present; (h) T = 1680 K, melt fraction = 0.01%; and (i) T = 1680 K, melt fraction = 1%. The southern hemisphere, with the initially thicker lithosphere, is darker in all dichotomy plots (c, f, i). For the remaining plots, north is approximately up, but some rotation has been done to better show the thermal structure and melt.

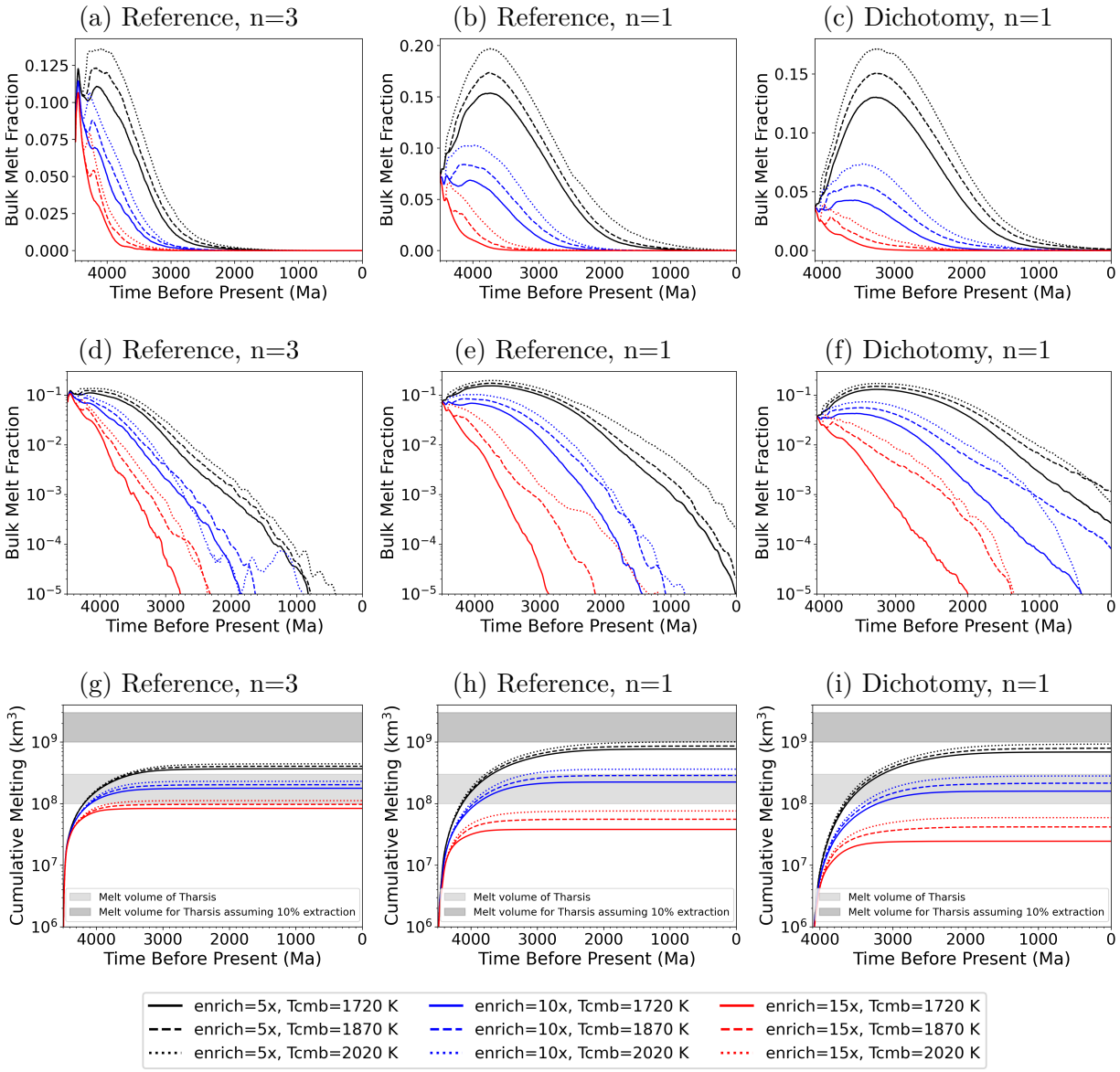

Figure 3.6: Melt and melt production over time. The bulk melt fraction is the fraction of the total mantle (out of 1.0) that is molten at a given time. This is shown here both on a linear and logarithmic scale. Cumulative melt is the integral of the mantle melt production rate over time. On the cumulative melt plots (g–i), approximate amount of melt ($1–33 \times 10^8$ km^3) required to produce Tharsis is shaded in lighter gray. However, only a fraction of the melt (here assumed to be 10%) produced in the mantle is extracted to and erupted on the surface. The darker gray shading on these same plots is the required melt volume multiplied by ten ($1–3 \times 10^9$ km^3) to account for this.

Model Rheology	Crustal HPE Enrichment	CMB T_0	Acceptable Geotherm	Melt at Present-Day	Enough Melt for Tharsis	Acceptable Geoid Power Spectrum
Uniform Low Activation Energy	5x	1720 K				
		1870 K				
		2020 K				
	10x	1720 K				
		1870 K				
		2020 K				
	15x	1720 K				
		1870 K				
		2020 K				
Uniform High Activation Energy	5x	1720 K				
		1870 K				
		2020 K				
	10x	1720 K				
		1870 K				
		2020 K				
	15x	1720 K				
		1870 K				
		2020 K				
Dichotomy High Activation Energy	5x	1720 K				
		1870 K				
		2020 K				
	10x	1720 K				
		1870 K				
		2020 K				
	15x	1720 K				
		1870 K				
		2020 K				

Figure 3.7: Color-coded summary of all 27 model cases and whether each one meet our constraints for geotherms, melt, and the geoid. Red indicates the constraint is not met. Blue indicates the constraint is met: geotherm consistent with Huang et al. [34]; melt at present-day; sufficient cumulative melt production to produce Tharsis (accounting for 10% melt extraction); or a geoid that agrees with the "Mars without Tharsis" geoid of Zuber and Smith [110]. Purple indicates an intermediate result: no melt at present, but within the past 200 Myr; sufficient melt for Tharsis allowing >10% melt extraction; or a geoid that either agrees with Zuber and Smith [110] only in the lowest degrees ($l \leq 6$) or falls between the red and blue geoids.

Chapter 4

The Mantle Melting Algorithm

In this chapter I explain in greater detail the methods and development of the melting calculations I have added to CitcomS and applied in Chapter 3, and the rationale behind them. I conclude with my most recent work on testing the effect of compressible convection on mantle temperatures and melt production. That will be the basis for a second mantle convection paper, focused on the melting methodology and the effects of compressible convection on melt production in the Martian mantle.

4.1 Introduction

In order to use geodynamic models to better answer questions about the volcanic history of Mars and the origin of Tharsis, and further constrain the parameters that effect melt production, it is essential to be able to calculate melt production with these geodynamic codes. CitcomS is a well-established and thoroughly benchmarked geodynamic code, but does not include melting. Therefore a prerequisite for my research was to implement a melting algorithm in CitcomS.

Full incorporation of melting calculations in 3D spherical geodynamic codes is relatively new, and still rare for Mars. Early geodynamic modeling of melt production in the Martian mantle was performed by Kiefer [41] in 2D axisymmetric geometry. Kiefer [41] calculated the melt fraction as a linear function of the difference between the dry solidus of Bertka and

Holloway [9] and a hypothetical liquidus at a fixed 200 K above the solidus. More recently, geodynamicists have come to rely on the experimentally derived parameterized melting model of Katz et al. [38] to more realistically calculate the melt fraction as a function of temperature and pressure, and this is incorporated into the standard version of ASPECT. This is not only true for modeling Earth's peridotite upper mantle, for which composition Katz et al. [38] was actually derived, but for Mars as well (e.g., Šrámek and Zhong [85]–3D spherical, and Kiefer and Li [43]–2D axisymmetric). Šrámek and Zhong [85] and Kiefer and Li [43] find that the solidus of Katz et al. [38] solidus is consistent with then solidi for Mars available at the time ([2, 9, 56]. But the more recent Mars solidus of Duncan et al. [21] is tens of degrees cooler in the depths where melting occurs in my models, and I find this to significantly impact the amount of melt generated.

Melt production can to some extent be estimated via this method by post-processing the temperature and velocity data, and this is how I initially tested melting with my first Mars models. But this approach has a number of drawbacks. While the direct melt-reducing effect of the temperature drop from the latent heat of melting can be approximated by reducing the post-processed temperatures as Kiefer [41] does, this is not ideal, and does not permit the latent heat of melting (or freezing) to be included in the solution of the energy equation. Even if one is not considering latent heating, the melting calculations being an integral part of the code allow the melt to be dealt with dynamically. For example, melt can be advected through the mantle, or a portion of it can be extracted (that is, removed from future calculations as if it erupted), or compositional changes such as the depletion of fertile mantle rock can be addressed. There is also the practical problem that post-processing is wholly reliant on the data that is output every x time steps, or y million years. My models take on the order of 100,000 time steps to complete, and outputting every 100 Myr produces well over 20 gigabytes of data for each individual run. Even if post-processed melt production

were otherwise as accurate as possible, this is very coarse temporal resolution, and would miss rapid changes or small intermittent amounts of melting, as happen near the beginning and end, respectively, of my models in Chapter 3. Post-processing melting at every time step, or even every few time steps, of these 3D models would take up far too much data and time to be feasible.

That said, figuring out how to properly include latent heat of melting (or freezing) into the energy equation within CitcomS, so that the program does not crash or get stuck, has proved to be a great challenge. It is in part for that reason that the models in Chapter 3 do not actually consider latent heat of melting. But as these models are of incompressible flow using the Boussinesq approximation, which does not consider viscous or adiabatic heating, or the latent heat of solid phase transitions, including latent heat of melting would be inconsistent. The proper treatment of latent heat of melting, as with other sources of latent heat, requires compressibility, or at least an extended Boussinesq approximation (EBA).

4.2 Melt Fraction

The first step in melt calculations is to calculate the equilibrium melt fraction, which for a given composition is a function of temperature and pressure. (Physical realism notwithstanding, it doesn't matter for the melt production algorithm how this is calculated–though ideally the function is analytically differentiable.) I calculate melt fraction (by mass) using the empirically derived parameterization of Katz et al. [38] for peridotite melting at terrestrial upper mantle pressures. The melt fraction algorithm of Katz et al. [38] was developed by fitting experimental data on equilibrium melting of peridotite and is valid up to approximately 8 GPa. Katz et al. [38] includes a formulation for hydrous melting; however, I am currently only considering dry melting.

Katz et al. [38] has since found broad application in geodynamic mantle convection codes such as CitcomS (e.g., Citron et al. [18], Šrámek and Zhong [85]), as well as ASPECT and adaptations thereof (e.g., Dannberg and Heister [19], Ninju et al. [66, 67]). While Katz et al. [38] was originally published with terrestrial melting in mind, it has been applied to calculate melt productivity in convection models of the Martian mantle, e.g. by Kiefer and Li [43], Šrámek and Zhong [85] and Citron et al. [18]. The utility of Katz et al. [38] is that it includes a solidus, liquidus, and a relatively straightforward nonlinear way to calculate melt fraction. Earlier geodynamic modeling employed simpler methods, such as the linear method of Kiefer [41], increasing the melt fraction at a fixed amount per degree above the solidus to an assumed liquidus that parallels the solidus.

In the Katz et al. [38] formulation, the equilibrium melt fraction X (by mass) is a function of pressure P (in GPa) and temperature T (herein I use kelvins). The parameter (A_1, A_2, etc.) values are summarized in Table 4.1, and except for the solidus–and the conversion from ° to K–are taken from Katz et al. [38]. The solidus T_s, hypothetical "lherzolite liquidus" T_{liq}^{lh}, and liquidus T_{liq} are parameterized as quadratic functions of P.

$$T_s(P) = A_1 + A_2 P + A_3 P^2 \tag{4.1}$$

$$T_{liq}^{lherz}(P) = B_1 + B_2 P + B_3 P^2 \tag{4.2}$$

$$T_{liq}(P) = C_1 + C_2 P + C_3 P^2 \tag{4.3}$$

Table 4.1: Summary of melt fraction parameterization parameters. See text for explanation of their use. The solidus parameters A_1, A_2, and A_3 are for the portion of the Duncan et al. [21] solidus up to 10 GPa. All other values are those of Katz et al. [38] for dry peridotite. Note that the A_1, B_1, and C_1 terms have been converted from °C in their respective publications to kelvins, in order to remain consistent with my use of absolute temperature for melting.

Function	**Parameter**	**Value**	**Units**
$T_{sol}(P)$	A_1	1361.15	K
	A_2	120.2	K GPa^{-1}
	A_3	-4.877	K GPa^{-2}
$T^{lh}_{liq}(P)$	B_1	1748.15	K
	B_2	80.0	K GPa^{-1}
	B_3	-3.2	K GPa^{-2}
$T_{liq}(P)$	C_1	2053.15	K
	C_2	45.0	K GPa^{-1}
	C_3	-2.0	K GPa^{-2}
X(T,P)	β	1.5	dimensionless
$X_{cpx-out}$	M_{cpx}	0.15	dimensionless
	r_0	0.50	dimensionless
	r_1	0.08	GPa^{-1}

The specific parameters of the dry peridotite solidus of Katz et al. [38], such that T_s = 1358.85 + 132.9P - 5.1P^2, is higher than the Duncan et al. [21] Mars solidus at corresponding pressures (T_s = 1361.15 + 120.2 P – 4.877 P^2): for example, by 45 K at 4 GPa (see Figure 4.1). (The Duncan et al. [21] solidus is a piece-wise quadratic fit to the results of high pressure experiments done on the simplified Dreibus and Wanke [20] composition of Bertka and Fei [8]. The relevant segment is the first one, valid at pressures up to 10 GPa.) Therefore, in order to be more consistent with Mars, I use the Duncan et al. [21] solidus in place of the Katz et al. [38] dry peridotite solidus. Unsurprisingly, this slightly increases the amount of melting, and allows melt production to continue for longer with the Martian mantle. We do not have a similar liquidus for Mars, so I retain that of Katz et al. [38].

The lherzolite liquidus is used to account for the exhaustion of clinopyroxene (cpx) in the solid phase, that is the point at which all cpx goes into the melt, or starts crystallizing from it. This occurs once the melt fraction reaches a value $X_{cpx-out}$ given by

$$X_{cpx-out}(P) = \frac{M_{cpx}}{R_{cpx}(P)} \tag{4.4}$$

where M_{cpx} is the modal fraction of cpx in the solid, and R_{cpx} is the melting reaction coefficient of cpx, which is empirically fit as a linear function of pressure

$$R_{cpx} = r_0 + r_1 P \tag{4.5}$$

Up to the exhaustion of clinopyroxene, the melt fraction X_{cpx} is calculated, using the solidus and the lherzolite liquidus temperatures, as

$$X_{cpx}(T, P) = \left(\frac{T - T_{sol}(P)}{T^{lh}_{liq}(P) - T_{sol}(P)} \right)^{\beta} \tag{4.6}$$

From this it follows that, at a given P, there is a temperature of clinopyroxene exhaution $T_{cpx-out}$ such that

$$T_{cpx-out}(P) = T_{sol}(P) + X_{cpx-out}(P)^{1/\beta} \cdot \left(T^{lh}_{liq}(P) - T_{sol}(P) \right) \tag{4.7}$$

At temperatures above $T_{cpx-out}$ where orthopyroxene (opx)–and/or in theory olivine–are the main phases being melted (or crystallized), the melt fraction, now X_{opx} , is calculated using the actual liquidus temperature and $T_{cpx-out}$ as

$$X_{opx}(T,P) = X_{cpx-out}(P) + (1 - X_{cpx-out}(P)) \left(\frac{T - T_{cpx-out}(P)}{T_{liq}(P) - T_{cpx-out}(P)} \right)^{\beta} \tag{4.8}$$

The melt fraction by mass obtained from this modified Katz et al. [38] method is then converted to a fraction by volume according to the equation

$$X_{vol} = \frac{\rho_s}{\rho_m \left(\frac{1}{X_{mass}} - 1 \right) + \rho_s} \tag{4.9}$$

where X_{vol} is the melt fraction by volume, X_{mass} is the melt fraction by mass, ρ_s is the solid mantle density ($3500\,\mathrm{kg\,m^{-3}}$ for my Boussinesq models), and rho_m is the melt density ($3000\,\mathrm{kg\,m^{-3}}$). From here on in this text, the melt fraction X used shall be the volume fraction, unless otherwise noted.

4.3 Melt Production

Melt production computations must consider not only the portion of a region that is molten (melt fraction) at a given time (which I get from Equations 4.6, 4.8, and 4.9), but also the movement of the mantle material through the melting region. Based on equation B1 in the second appendix of Watson and McKenzie [101], $\dot{M}$, the instantaneous amount of melt per unit of mantle material produced per unit time, is the material derivative of the equilibrium melt fraction X.

$$\dot{M} = \frac{DX}{Dt} = \frac{\partial X}{\partial t} + \mathbf{u} \cdot \nabla X \tag{4.10}$$

Using the chain rule, $\dot{M}$ can be written in terms of the partial derivatives of the melt fraction with respect to temperature and pressure. This is why having an analytically differentiable melt fraction parameterization is very helpful.

$$\dot{M} = \frac{DX}{Dt} = \frac{\partial X}{\partial T}\frac{DT}{Dt} + \frac{\partial X}{\partial P}\frac{DP}{DT} = \frac{\partial X}{\partial T}\left(\frac{\partial T}{\partial t} + \mathbf{u}\cdot\nabla T\right) + \frac{\partial X}{\partial P}\left(\frac{\partial P}{\partial t} + \mathbf{u}\cdot\nabla P\right) \tag{4.11}$$

Assuming $\partial P/\partial t$ is zero, this becomes

$$\dot{M} = \frac{\partial X}{\partial T}\left(\frac{\partial T}{\partial t} + \mathbf{u}\cdot\nabla T\right) + \frac{\partial X}{\partial P}\mathbf{u}\cdot\nabla P \tag{4.12}$$

Further assuming that pressure is hydrostatic, then

$$\dot{M} = \frac{\partial X}{\partial T}\left(\frac{\partial T}{\partial t} + \mathbf{u}\cdot\nabla T\right) - \frac{\partial X}{\partial P}\bar{\rho}g u_r \tag{4.13}$$

where u_r is the radial component of velocity, $\bar{\rho}$ is the radial profile of density (a constant and uniform $3500\,\mathrm{kg\,m^{-3}}$ for my models in Chapter 3), and g is the magnitude of gravitational acceleration. The volume of melt produced is calculated by integrating $\dot{M}$ over the element volumes using Gaussian quadrature (through calling a function that is part of the standard CitcomS code).

Any geodynamic code will already compute the term $\frac{\partial T}{\partial t} + \mathbf{u}\cdot\nabla T$ for the energy equation, but we still need to compute the partial derivatives $\frac{\partial X}{\partial T}$ and $\frac{\partial X}{\partial P}$. The Katz et al. [38] parameterization makes this analytical and straightforward in principal–if somewhat convoluted in regard to the algebra and number of terms, particularly for melt fractions above the ex-

haustion of clinopyroxene. Fortunately, the expanded forms of these partial derivatives can be found in Appendix C of Dannberg and Heister [19].

For melt fractions below the exhaustion of clinopyroxene, these derivatives are

$$\frac{\partial X_{cpx}(T,P)}{\partial T} = \beta \left(\frac{T - T_{sol}(P)}{T^{lh}_{liq}(P) - T_{sol}(P)} \right)^{\beta-1} \times \frac{1}{T^{lh}_{liq}(P) - T_{sol}(P)} \tag{4.14}$$

and

$$\begin{aligned} \frac{\partial X_{cpx}(T,P)}{\partial P} = \beta & \left(\frac{T - T_{sol}(P)}{T^{lh}_{liq}(P) - T_{sol}(P)} \right)^{\beta-1} \\ & \times \left(\frac{\partial T^{lh}_{liq}(P)}{\partial P} \left(T_{sol}(P) - T \right) + \frac{\partial T_{sol}(P)}{\partial P} \left(T - T^{lh}_{liq}(P) \right) \right) \\ & \times \frac{1}{\left(T^{lh}_{liq}(P) - T_{sol}(P) \right)^2} \end{aligned} \tag{4.15}$$

Above the exhaustion of clinopyroxene, these derivatives are

$$\begin{aligned} \frac{\partial X_{opx}(T,P)}{\partial T} = \beta(1 - X_{cpx-out}) & \left(\frac{T - T_{cpx-out}(P)}{T_{liq}(P) - T_{cpx-out}(P)} \right)^{\beta-1} \\ & \times \frac{1}{T_{liq}(P) - T_{cpx-out}(P)} \end{aligned} \tag{4.16}$$

and

$$\frac{\partial X_{cpx}(T,P)}{\partial P} = \frac{dX_{cpx-out}(P)}{dP}\left[1-\left(\frac{T-T_{cpx-out}(P)}{T_{liq}(P)-T_{cpx-out}(P)}\right)^{\beta}\right] + \beta(1-X_{cpx-out})\left(\frac{T-T_{cpx-out}(P)}{T_{liq}(P)-T_{cpx-out}(P)}\right)^{\beta-1} \times \frac{\frac{dF_{cpx-out}}{dP}(T_{cpx-out}-T_{liq}) + \left(\frac{dT_{liq}}{dP}+\frac{dT_{cpx-out}}{dP}\right)(T_{cpx-out}-T)}{\left(T^{lh}_{liq}(P)-T_{sol}(P)\right)^2} \tag{4.17}$$

4.4 Latent Heat

With specific enthalpy of fusion $\Delta H_{melt} = T\Delta S_m$, entropy of fusion ΔS_m, and equilibrium melt fraction X, the latent heating rate Q_{melt} per unit volume due to melting (or crystallization) is

$$Q_{melt} = \bar{\rho}\Delta H_m \dot{M} \tag{4.18}$$

Therefore

$$Q_{melt} = \bar{\rho}\Delta H_m \frac{\partial X}{\partial T}\frac{DT}{Dt} - \bar{\rho}\Delta H_m \frac{\partial X}{\partial P}\bar{\rho} g u_r \tag{4.19}$$

The energy equation used by CitcomS, but with the added term Q_{melt} is

$$\begin{aligned}\bar{\rho}c_p\frac{DT}{Dt}\left(1+2\Gamma(1-\Gamma)\frac{\gamma_{ph}^2}{d_{ph}}\frac{Rb}{Ra}Di(T+T_0)\right) &= \bar{\rho}c_p\kappa\nabla^2 T \\ &- \bar{\rho}\alpha g u_r Di(T+T_0)\left(1+2\Gamma(1-\Gamma)\frac{\gamma_{ph}}{d_{ph}}\frac{Rb}{Ra}\right) \\ &+ \frac{Di}{Ra} + \bar{\rho}H + Q_{melt}\end{aligned} \tag{4.20}$$

where c_P is the specific heat capacity, and the terms involving the dissipation number Di or the phase function Γ are part of the latent heat of the solid-solid phase transitions (e.g., olivine to wadsleyite) in compressible convection, which are explained in more detail in Christensen and Yuen [17]. The phase function Γ is the fraction (between 0 and 1) of the heavier solid phase; γ_{ph} is the Clapeyron slope of the solid phase change; d_{ph} is the depth of the phase change; Rb is the chemical Rayleigh number; and T_0 is the surface temperature.

$$Rb = Ra\frac{\delta\rho_{ph}}{\rho_0\alpha_0\Delta T} \tag{4.21}$$

where $\delta\rho_{ph}$ (part of Rb) is the density change associated with the phase transition.

$$Di = \frac{\alpha_0 g R_0}{c_P} \tag{4.22}$$

$$\Gamma = \frac{1}{2}\left(1+tanh\left(\frac{\pi}{\bar{\rho}g w_{ph}}\right)\right) \tag{4.23}$$

$$\pi = \bar{\rho}g(1-r-d_{ph}) - \gamma_{ph}(T-T_{ph}) \tag{4.24}$$

where r is the radial coordinate and T_{ph} is the temperature of the phase change.

At first, it appeared incorporating latent heat into the energy equation residual in the code could be done by calculating Q_{melt} and adding it to the RHS, as is done with radiogenic heating $\bar{\rho}H$. However, this never worked in practice, and the code always crashed as significant melting or crystallization occured. This tends to happen as heads of rising plumes reach the base of the lithosphere. The failures generally occurred between 100 and 1000 Myr into the model run.

A major problem was that the temperature derivative (for which we are calculating the residual) is part of Q_{melt} So, instead we want to isolate the DT/Dt term on the left hand side, analogous to how CitcomS already handles the latent heat of solid-solid phase transitions when doing compressible flow. First, we substitute Q_{melt} with its expanded form in equation (4.19).

$$\begin{aligned}\bar{\rho}c_p\frac{DT}{Dt}\left(1+2\Gamma(1-\Gamma)\frac{\gamma_{ph}^2}{d_{ph}}\frac{Rb}{Ra}Di(T+T_0)\right) &= \bar{\rho}c_p\kappa\nabla^2 T \\ &- \bar{\rho}\alpha g u_r Di(T+T_0)\left(1+2\Gamma(1-\Gamma)\frac{\gamma_{ph}}{d_{ph}}\frac{Rb}{Ra}\right) \\ &+ \frac{Di}{Ra} + \bar{\rho}H \\ &+ \bar{\rho}\Delta H_m\frac{\partial X}{\partial T}\frac{DT}{Dt} - \bar{\rho}\Delta H_m\frac{\partial X}{\partial P}\bar{\rho}g u_r\end{aligned} \tag{4.25}$$

The temperature portion of Q_{melt} (i.e., $\bar{\rho}\Delta H_m(\partial X/\partial T)(DT/Dt)$) can join the temperature portion of the transition zone latent heating on the left hand side, leaving the pressure portion $-\bar{\rho}\Delta H_m\frac{\partial X}{\partial P}\bar{\rho}g u_r$ on the RHS.

$$\begin{aligned}\bar{\rho}c_p\frac{DT}{Dt}\left(1+2\Gamma(1-\Gamma)\frac{\gamma_{ph}^2}{d_{ph}}\frac{Rb}{Ra}Di(T+T_0)-\left(\frac{1}{c_p}\Delta H_m\frac{\partial X}{\partial T}\right)\right) &= \bar{\rho}c_p\kappa\nabla^2 T \\ -\bar{\rho}\alpha g u_r Di(T+T_0)\left(1+2\Gamma(1-\Gamma)\frac{\gamma_{ph}}{d_{ph}}\frac{Rb}{Ra}\right) & \\ +\frac{Di}{Ra}\ +\bar{\rho}H-\bar{\rho}\Delta H_m\frac{\partial X}{\partial P}\bar{\rho}g u_r & \end{aligned} \tag{4.26}$$

Then, dividing both sides through by the part of the left hand side in parentheses gives

$$\begin{aligned}\bar{\rho}c_p\frac{DT}{Dt} = & \frac{\bar{\rho}c_p\kappa\nabla^2 T}{\left(1+2\Gamma(1-\Gamma)\frac{\gamma^2}{d_{ph}}\frac{Rb}{Ra}Di(T+T_0)-\left(\frac{1}{c_p}\Delta H_m\frac{\partial X}{\partial T}\right)\right)} \\ & -\frac{\bar{\rho}\alpha g u_r Di(T+T_0)\left(1+2\Gamma(1-\Gamma)\frac{\gamma}{d_{ph}}\frac{Rb}{Ra}\right)}{\left(1+2\Gamma(1-\Gamma)\frac{\gamma^2}{d_{ph}}\frac{Rb}{Ra}Di(T+T_0)-\left(\frac{1}{c_p}\Delta H_m\frac{\partial X}{\partial T}\right)\right)} \\ & +\frac{\frac{Di}{Ra}\ +\bar{\rho}H}{\left(1+2\Gamma(1-\Gamma)\frac{\gamma^2}{d_{ph}}\frac{Rb}{Ra}Di(T+T_0)-\left(\frac{1}{c_p}\Delta H_m\frac{\partial X}{\partial T}\right)\right)} \\ & +\frac{\bar{\rho}\Delta H_m\frac{\partial X}{\partial P}\frac{DP}{Dt}}{\left(1+2\Gamma(1-\Gamma)\frac{\gamma^2}{d_{ph}}\frac{Rb}{Ra}Di(T+T_0)-\left(\frac{1}{c_p}\Delta H_m\frac{\partial X}{\partial T}\right)\right)}\end{aligned} \tag{4.27}$$

Assuming incompressible flow (Boussinesq approximation), and in effect ignoring the solid phase transitions, this would simplify to

$$\bar{\rho}c_p\frac{DT}{Dt} = \frac{\bar{\rho}c_p\kappa\nabla^2 T+\bar{\rho}H-\bar{\rho}^2\Delta H_m\frac{\partial X}{\partial P}g u_r}{1-\frac{1}{c_p}\Delta H_m\frac{\partial X}{\partial T}} \tag{4.28}$$

where the portion of latent heating contributed by the temperature derivative of the melt fraction is in the denominator, and the pressure derivative portion is in the numerator.

However, this simplification is not technically correct, as consideration of any latent heat requires considering compressible flow, rather than a purely Boussinesq approximation. Therefore, it is acceptable, even technically appropriate, that given the models in Chapter 3 use the Boussinesq approximation, they do not consider latent heat of melting. That is irrespective of the question of whether or not switching to fully compressible flow, or somewhat more simply an extended Boussinesq approximation, (either of which would allow for the consideration of latent heat of melting) would affect the results of Chapter 3.

4.5 Extended Boussinesq Approximation Models

4.5.1 Methods

All models in Chapter 3 consider incompressible flow, or more precisely the Boussinesq approximation, where the energy equation is like Equation 4.28, but with $\Delta H_m = 0$.

$$\bar{\rho} c_p \frac{DT}{Dt} = \bar{\rho} c_p \kappa \nabla^2 T + \bar{\rho} H \tag{4.29}$$

Under the extended Boussinesq approximation (EBA), we consider terms in the energy equation with the dissipation number Di, the dimensionless number given by.

$$Di = \frac{\alpha g L}{c_P} \tag{4.30}$$

where α is the thermal expansivity, g is the gravitational acceleration, L is the length scale, and c_P is the heat capacity. L is typically taken to be the mantle thickness, but like with the Rayleigh number, CitcomS uses the planetary radius as the length scale. In effect, the energy

equation again becomes that given by Equation 4.28, and we can consider the effects of latent heating. (If Di is taken to be zero, the energy equation simplifies back to the Boussinesq energy equation.) For Earth, calculated according to Equation 4.30, Di is between 0.25 and 0.8 [47], or 0.56–1.8 if rescaled according to CitcomS. For Mars, using the values in Chapter 3 Table 3.1 (α=2 $\times$ 10^{-5}, g=3.72 m s^{-2}, c_P=1250 J kg^{-1} K), Di is lower, and would be 0.09 according to the traditional mantle thickness L (1559 km.), and 0.2 using the CitcomS radial (3389.5 km) scaling. Therefore, compressibility should have a smaller effect in the Martian mantle than in Earth's.

To begin testing the effect of compressibility on temperature and melting within a Mars-like mantle, I ran models with four different Di: 0.0, 0.1, 0.25, and 0.5. Di=0.0 is a Boussinesq control case; the other three values are the actual EBA cases. These models use the same parameters as the models in Chapter 3, specifically those with low activation energy and an initial CMB temperature of 1.0 $\times$ ΔT = 1720 K. The difference is that these new models don't include crustal enrichment, and don't necessarily use the decaying heating. (This configuration was selected to minimize additional code development, while still minimizing the run time.) While the cases with Di>0 do consider compressible heating (viscous and adiabatic heating, and the latent heat of solid phase transitions) I have not yet included the latent heat of melting (or freezing).

First, I ran the four different Di cases with a constant non-dimensional radiogenic heating of Q=25, equivalent to 4.09 $\times$ 10^{-12} J kg^{-1}), which is close to the present-day value for Mars based on Dreibus and Wanke [20], if crustal enrichment is not considered. Next, I repeated these four cases, except with decaying heating as in Chapter 3, that is with the initial value based on the back-projected Dreibus and Wanke [20] composition. For these cases, the initial radiogenic Q is 144 (2.36 $\times$ 10^{-11} J kg^{-1}), and only reaches near 25 close to present-day. While lower activation energy and CMB temperature models run faster than

the otherwise equivalent models with high activation energy or a warmer CMB, the lack of crustal enrichment in these cases leads to more mantle heating, and so these models are still quite slow to run. As a result, I do not yet have the full runs to present-day for these four cases. The currently available results only go out 1.6-1.7 Gyr instead of the full 4.5 Gyr.

4.5.2 Preliminary Results

The results to date are summed up in the plots of Figure 4.2. For the radiogenic Q=25 set of models, varying Di has at most a modest effect on the mantle temperature. Of note, while increasing Di leads to a slightly warmer, more slowly cooling mantle as a whole, it has the opposite effect on the upper mantle temperature, particularly in the "melting zone" at 200-300 km depth. This small decrease in temperature has a significant impact on melt production, with cumulative melt for Di=0.5 approximately an order of magnitude less than for Di=0.0. In stark contrast, the effect of increasing Di on temperature and melt for the decaying heating (initially Q=144) cases is negligible, at least so far as they have reached. The curves plot indistinguishably atop one another.

4.5.3 Discussion and Initial Conclusions

For the decaying radiogenic heating cases, the radiogenic heating starts out much higher than for the Q=25 cases, and would only reach that low level near present-day. Consequently, overall heating in the decaying Q cases is more dominated by radiogenic heating, as opposed to compressible heating. When Q is low, the magnitude of the overall heating is lower, and the effects of relatively small differences in compressible heating show up.

The decaying radiogenic heating results so far cover the time period when Tharsis should form. Thus, I do not expect switching to compressible convection should, by itself, have

a major effect on the ability to produce Tharsis. It should also be noted again that, for expediency, the low activation energy was used. The higher activation energy cases, which I found in Chapter 3 to produce temperatures and melting more consistent with Mars, cool more slowly. Therefore, the impact of a higher Di on melt may be smaller when I run with higher activation energy. Another point is that Mars' Di is relatively low, and as calculated for CitcomS (Di=0.2) would fall roughly midway between the Di=0.1 and 0.25 curves, rather than the extreme of Di=0.5. As the models approach present-day, the radiogenic heat will decrease such that compressible effect may become more influential. The compressible upper mantle will eventually cool more quickly than the incompressible case, and this could have significant impacts on late stage melting. Nevertheless, as the results of Chapter 3 show, it is actually not difficult to produce very small amounts of melt in the cool Martian mantle of today (as shown by our high activation energy cases consistent with Huang et al. [34]), and this is even possible for some of the significantly colder geotherms produced by our low activation energy cases. So a modest acceleration of mantle cooling in the late Amazonian as a result of compressible effects should not be a concern. Indeed, if a hotter early mantle is needed to produce Tharsis, as my work in Chapter 3 suggests, this late cooling should be helpful in still matching the present geotherm constraint from Huang et al. [34], as well as in explaining the rapid decline in volcanic activity in the Amazonian.

One caveat to the initial conclusion that compressible convection should not significantly impact early melt production is that these initial compressible/EBA models do not consider crustal HPE enrichment. Crustal enrichment reduces the radiogenic heating with the mantle and, as the results of Chapter 3 show, leads to less overall heating, faster cooling, and a great deal less melt. This impact will be most significant for the 15x enrichment cases, which for a 50 km thick crust, start out with radiogenic heating approximately 0.24 times the no enrichment case, or Q=35. For 10x and 5x enrichment–which are more favorable for meeting

the melting constraints–this factor increases to 0.51 (Q=73) and 0.78 (Q=112), respectively, so the effect of compressible heating on early melt (if any) should be subdued in cases of low to moderate crustal enrichment. Second, the effect of latent heat of melting remains to be tested. If I consider, as in Chapter 3, that only $\sim 10\%$ of the melt in the mantle is extracted, most of the rest must in the long term freeze and release its latent heat of fusion into the mantle, so the overall cooling contribution of latent heat of melting may be much lower than the total melt production suggests. Third, I have yet to test fully compressible convection, and there exists the potential for this to have a more significant impact. Yet, the results so far with the EBA suggest that the negative effects on matching Mars' melting history are limited, and slightly faster cooling from compressible convection in an initially hotter mantle than modeled in Chapter 3 may even be helpful in finding a model that can both produce Tharsis early on and satisfy InSight constraints for the present-day mantle temperature.

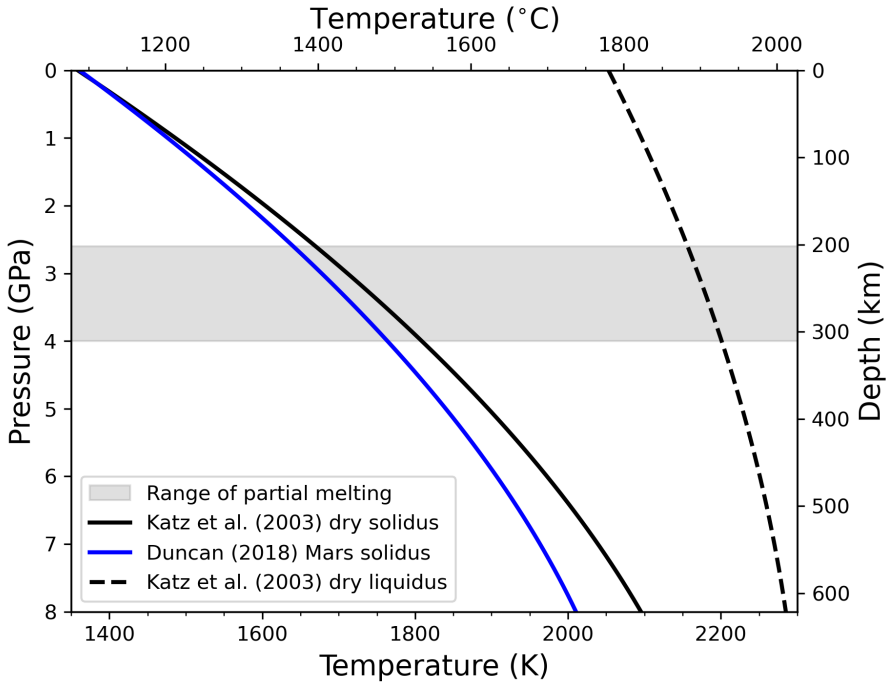

Figure 4.1: Comparison of the Katz et al. [38] dry solidus with the Duncan et al. [21] solidus, which are both parameterized with respect to pressure (in GPa). Approximate corresponding depths and the Katz et al. [38] liquidus are also included.

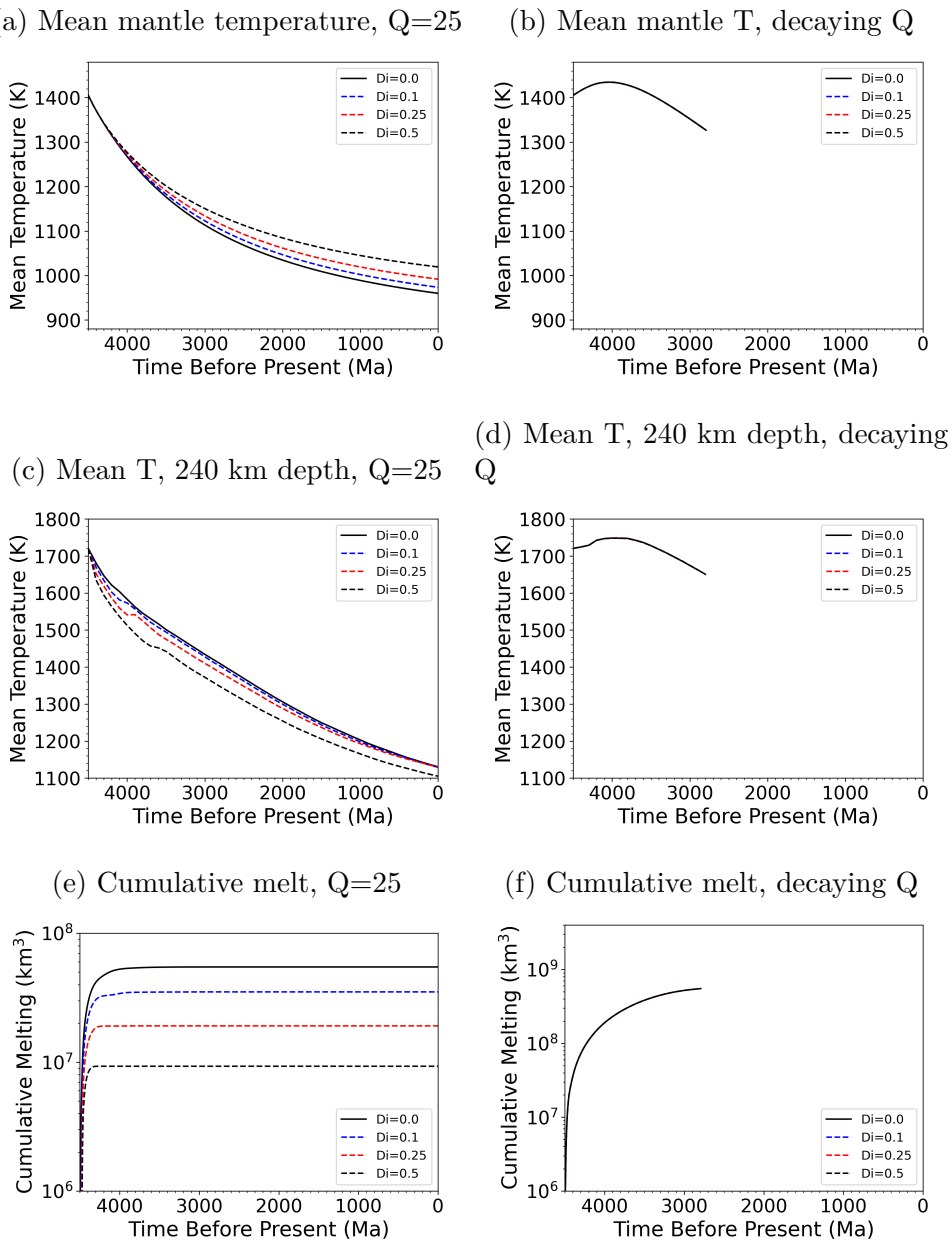

Figure 4.2: Comparisons of temperature and cumulative melt production, varying the disputation number (Di), for the Boussinesq approximation (Di=0.0) and extended Boussinesq approximation (EBA) models. The plots in the left column are for a constant non-dimensional radiogenic heating of Q=25 (4.09×10^{-12} J kg^{-1}), which is close to the present-day value. The plots in the right column use the decaying heating based on the back-projected Dreibus and Wanke [20] composition, the same as the models in Chapter 3: initial Q=144 (2.36×10^{-11} J kg^{-1}). 240 km depth is near the middle of the melting depth range (e.g., Figure 4.1). For the decaying, higher radiogenic heating models, varying Di has a negligible effect on temperature and melt, and the four curves are indistinct.

Chapter 5

Looking Forward

The most immediate avenue of further research for me will be completing the compressible convection and latent heat modeling. As I infer at the end of Chapter 4, a hotter initial condition in combination with slightly faster cooling of an HPE-depleted mantle with compressible convection. Concurrent with this work and as I suggest in the conclusions of Chapter 3, I can try adjusting the radial viscosity models for the high activation energy, 10x enrichment cases to see if this can bring the geoid more in line with Zuber and Smith [110]. Within the code, I haven't actually done anything with the melt other than assume a fraction of it gets extracted, so this another area to explore. With the melting fully working, there is room to consider applying the melting calculations to other rocky bodies such as Venus or the Moon, tweaking the solidi and liquidi as appropriate.

NASA and ESA are working on the actual return mission, while NASA's Mars 2020 rover (Perseverance) collects and caches the samples. (At the time of writing, expected budget overruns and and politics are making the mission's future more uncertain.) The most recent Planetary Science and Astrobiology Decadal Survey identified Mars Sample Return as a priority. While not necessarily as immediately relevant to geodynamics as InSight, direct laboratory access to Mars samples (other than SNC meteorites) would revolutionize the study of Mars. The volcanic rock samples collected by Perseverance could provide new and useful insights into Mars' interior composition and geodynamic history. The return to the Moon with Artemis and associated missions, both crewed and uncrewed, and the eventual

landing of humans on Mars, should further expand the reach of geophysical methods to study other worlds. (How relatively simple setting up a heat flow probe might be with–yes, the really hard part of–actual people on the ground!)

Implementing the cooling core boundary condition using the old 1D model of core cooling got me thinking about the complexities of fluid dynamics, heat flow, and melting/freezing in the core, and not just the mantle. These layers are but parts of the whole planet, and processes in one affect the other. Ideally, future advances in computing and knowledge of the physic sand chemistry of planetary interiors will allow the creation of fully integrated models of planets, or at least Earth, that consider all of the layers coupled together.

Thinking more broadly about applying geodynamic modeling and geophysics in general, the new data gleaned by missions like InSight, and to some extent almost any planetary mission, are quite useful for constraining models of planetary interiors. Yet, at least for Mars and Earth, the amount of data and the body of modeling done can at times feel over constraining. Other planetary bodies such as Venus or the outer planet moons would offer a change of pace and allow some more space for new modeling and speculation. There will be many opportunities to investigate other, less-studied planetary bodies in our solar system. Psyche will soon be launching to visit its namesake metallic asteroid–perhaps the home of extinct metallic volcanoes. In a little over a year, Europa Clipper will be heading to Jupiter and many informative flybys of its own namesake icy moon. The Dragonfly helicopter will follow Clipper to the outer solar system, and land and fly on Saturn's large moon Titan, carrying on the pioneering geophysical legacy of InSight with the first seismometer on a body other than Earth, the Moon, or Mars. VERITAS and EnVision should–eventually–orbit Venus and greatly broaden and deepen the state of knowledge of that largely hidden planet. Going even further abroad in space, I would by no means be the first to consider exoplanets, but

this would offer a fresher, if more theoretical, direction in geodynamics. Super-Earths in particular are notable for being a common type of planet absent from our own solar system.

Returning once again to the InSight mission, it was a privilege and rewarding experience to be able to attend the science team meetings, learn about the inner workings of planetary science missions from the science team perspective, share my research, and meet and interact with other scientists on the team. I hope that in the future I have the opportunity to join and contribute to one or more of the missions mentioned above or some future, as yet to be proposed or selected, mission.

Appendices

Appendix A

A More Realistic Dichotomy

Another major addition I made to CitcomS is the ability to include a dichotomy in crustal or lithospheric thickness. In the modeling in Chapter 3, I only use a simple hemispheric, equatorial dichotomy boundary. However, there is also not the option to define an arbitrary dichotomy using spherical harmonic coefficients, which can be read in from a file. This dichotomy is defined rheologically, with the viscosity of the portion of the spherical shell (up to a specified depth, or step thickness) assigned to the southern highlands being set to the maximum value. Alternatively, the dichotomy depth can be variable, determined by the same spherical harmonic coefficients. This allows arbitrary dichotomy cases to be considered, including a simple degree-1 dichotomy with the boundary at the equator and a more realistic dichotomy boundary derived from shape and gravity measurements.

The method of Andrews-Hanna et al. [4], from Banerdt [6], is employed to recover the pre-Tharsis dichotomy boundary. The model of Banerdt [6], as illustrated in Figure A.1, assumes total crustal thickness can be divided into a uniform crustal plate thickness, topography, and an isostatic root. Some of the topography is supported by flexure and some by isostacy. Given assumptions for the values of the mantle density, crustal density, and the thickness and elastic properties of the lithosphere, a linear matrix equation can be set up to solve for the unknown isostatic root thickness and flexural displacement. Root thickness, flexural displacement, and topography are represented as spherical harmonic coefficients. A a matrix equation is solved for each coefficients in order to produce a spatially varying flexure and

isostatic root thickness based (in part) on the spatially varying topography. This method was used by Andrews-Hanna et al. [4] to derive the pre-Tharsis crustal thickness by assuming that the very early forming crustal dichotomy is supported primarily by isostacy, while the Tharsis rise is supported primarily by flexure. The region of positive isostatic root thickness would therefore coincide with the southern highlands. An example of my pre-Tharsis dichotomy, to spherical harmonic degree 40, is shown in Figure A.2.

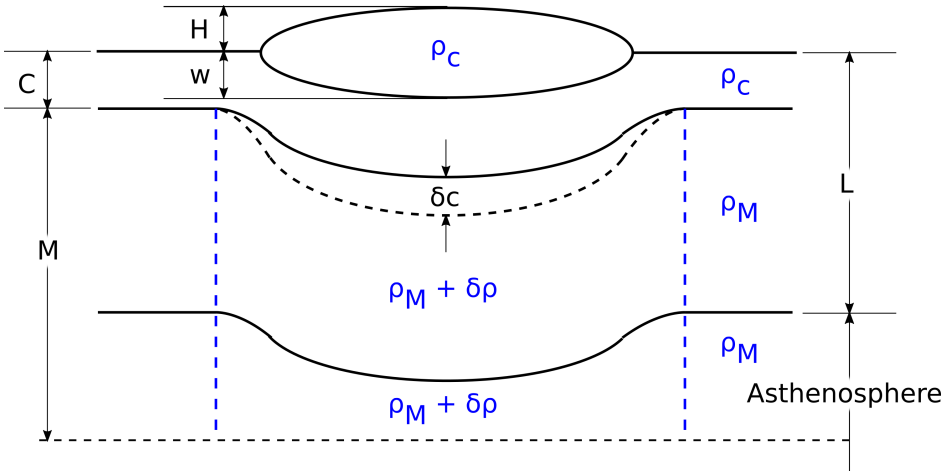

Figure A.1: Schematic based on the one in Banerdt [6]), where ρ_c is crustal density, δc is the isostatic root thickness, w is the downward displacement due to flexure, C is the uniform crustal plate thickness, ρ_m is mantle density, $\delta\rho$ is the mantle density anomaly, M is the thickness of mantle density anomaly, H is the surface topography, and L is the elastic lithosphere thickness. H, w, $\delta\rho$ and δc are represented by spherical harmonic coefficients, so they can vary across the planet.

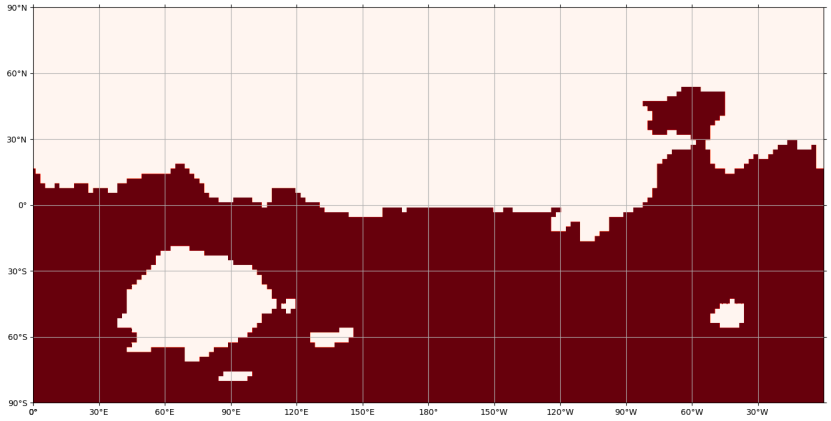

Figure A.2: Pre-Tharsis dichotomy to spherical harmonic degree 40, using the method of Andrews-Hanna et al. [4] and Banerdt [6]. Tharsis would be centered around 100°W near the equator. The northward extension of the southern highlands east of Tharsis, around 60°W, is Tempe Terra. The large "hole" in the southern highlands in the lower left (75°E, 45°S) is associated with the Hellas basin, and the smaller one in the lower right (40°W, 50°S) is the Argyre basin. Both of these are large and ancient impact basins.

Bibliography

[1] Milton Abramowitz and Irene A. Stegun. *Handbook of Mathematical Functions with Formulas, Graphs, and Mathematical Tables*. Dover, New York City, ninth dover printing, tenth gpo printing edition, 1964.

[2] C. B. Agee and D. S. Draper. Experimental constraints on the origin of Martian meteorites and the composition of the Martian mantle. *Earth and Planet. Sci. Lett.*, 224:415–429, 2004. doi:https://doi.org/10.1016/j.epsl.2004.05.022.

[3] O. Aharonson, M.T. Zuber, and D.H. Rothman. Statistics of Mars' topography from the Mars Orbiter Laser Altimeter: Slopes, correlations, and physical models. *J. Geophys. Res.*, 106:23723–23735, 2001. doi:https://doi.org/10.1029/2000JE001403.

[4] J.C. Andrews-Hanna, M.T. Zuber, and W.B. Banerdt. The Borealis basin and the origin of the martian crustal dichotomy. *Nature Lett.*, 453(26):1212–1215, 2008. doi:https://doi.org/10.1038/nature07011.

[5] W. B. Banerdt, S. E. Smrekar, D. Banfield, D. Giardini, M. Golombek, C. L. Johnson, P. Lognonné, A. Spiga, T. Spohn, C. Perrin, et al. Initial results from the InSight mission on Mars. *Nature Geosciences*, 13:183–189, 2020. doi:https://doi.org/10.1038/s41561-020-0544-y.

[6] W.B. Banerdt. Support of Long-Wavelength Loads on Venus and Implications for Internal Structure. *J. Geophys. Res.*, 91(B1):403–419, 1986. doi:https://doi.org/10.1029/JB091iB01p00403.

[7] D. C. Berman and W. K. Hartmann. Recent fluvial, volcanic, and tectonic activity on the Cerberus plains of Mars. *Icarus*, 159(1):1–17, 2002. doi:https://doi.org/10.1006/icar.2002.6920.

[8] C. M. Bertka and Y. Fei. Mineralogy of the Martian interior up to core-mantle boundary pressures. *Journal of Geophysical Research: Solid Earth*, 102(B3):5251–5264, 1997. doi:https://doi.org/10.1029/96jb03270.

[9] C. M. Bertka and J. R. Holloway. Anhydrous partial melting of an iron-rich mantle I: subsolidus phase assemblages and partial melting phase relations at 10 to 30 kbar. *Contributions to Mineralogy and Petrology*, 115:313–322, 1994. doi:https://doi.org/10.1007/BF00310770.

[10] D. D. Bogard and P. Johnson. Martian Gases in an Antarctic Meteorite? *Science*, 221 (4611):651–654, 1983. doi:https://doi.org/10.1126/science.221.4611.651.

[11] W. V. Boynton, G. J. Taylor, L. G. Evans, R. C. Reedy, R. Starr, D. M. Janes, K. E. Kerry, D. M. Drake, K. J. Kim, R. M. S. Williams, M. K. Crombie, J. M. Dohm, V. Baker, A. E. Metzger, S. Karunatillake, J. M. Keller, H. E. Newsom, J. R. Arnold, J. Brückner, P. A. J. Englert, O. Gasnault, A. L. Sprague, I. Mitrofanov, S. W. Squyres, J. I. Trombka, L. d'Uston, H. Wänke, and D. K. Hamara. Concentration of h, si, cl, k, fe, and th in the low- and mid-latitude regions of mars. *Journal of Geophysical Research*, 112(E12), 2007. doi:https://doi.org/10.1029/2007je002887.

[12] A. Broquet and J. C. Andrews-Hanna. Geophysical evidence for an active mantle plume underneath Elysium Planitia on Mars. *Nature Astronomy*, pages 1–10, 2022. doi:https://doi.org/10.1038/s41550-022-01836-3.

[13] M. H. Carr. Volcanism on Mars. *J. Geophys. Res.*, 78:4049–4062, 1973. doi:https://doi.org/10.1029/JB078i020p04049.

[14] M. H. Carr and J. W. Head. Geologic history of Mars. *Earth and Planetary Science Letters*, 294(3-4):185–203, 2010. doi:https://doi.org/10.1016/j.epsl.2009.06.042.

[15] H.S. Carslaw and J.C. Jaeger. *Conduction of Heat in Solids*, chapter 13. Oxford at the Clarendon Press, London, second edition, 1959.

[16] U. Christense. Convection in a variable-viscosity fluid: Newtonian versus power-law rheology. *Earth and Planet. Sci. Lett.*, 64:153–162, 1983. doi:https://doi.org/10.1016/0012-821X(83)90060-2.

[17] U. R. Christensen and D. A. Yuen. The interaction of a subducting lithospheric slab with a chemical or phase boundary. *Journal of Geophysical Research: Solid Earth*, 89 (B6):4389–4402, June 1984. doi:https://doi.org/10.1029/jb089ib06p04389.

[18] R. I. Citron, M. Manga, and E. Tan. A hybrid origin of the Martian crustal dichotomy: Degree-1 convection antipodal to a giant impact. *Earth and Planet. Sci. Lett.*, 491: 58–66, 2018. doi:https://doi.org/10.1016/j.epsl.2018.03.031.

[19] J. Dannberg and T. Heister. Compressible magma/mantle dynamics: 3-D, adaptive simulations in ASPECT. *Geophysical Journal International*, 207(3):1343–1366, 2016. doi:https://doi.org/10.1093/gji/ggw329.

[20] G. Dreibus and H. Wanke. Mars, a Volatile-Rich Planet. *Meteoritics*, 20(2):367–381, 1985.

[21] M. S. Duncan, N. C. Schmerr, C. M. Bertka, and Y. Fei. Extending the solidus for a model iron-rich Martian mantle composition to 25 GPa. *Geophysical Research Letters*, 45(19):10,211–10,220, 2018. doi:https://doi.org/10.1029/2018GL078182.

[22] L. T. Elkins-Tanton. Possible formation of ancient crust on mars through magma ocean processes. *Journal of Geophysical Research*, 110(E12), 2005. doi:https://doi.org/10.1029/2005je002480.

[23] L. T. Elkins-Tanton, E. M. Parmentier, and P. C. Hess. Magma ocean fractional crystallization and cumulate overturn in terrestrial planets: Implications for Mars. *Meteoritics & Planetary Science*, 38(12):1753–1771, 2003. doi:https://doi.org/10.1111/j.1945-5100.2003.tb00013.x.

[24] D. Giardini, P. Lognonné, W. B. Banerdt, W. T. Pike, U. Christensen, S. Ceylan, J. F. Clinton, M. van Driel, S. C. Stähler, M. Böse, et al. The seismicity of Mars. *Nature Geoscience*, 13(3):205–212, 2020. doi:https://doi.org/10.1038/s41561-020-0539-8.

[25] M. Grott, T. Spohn, J. Knollenberg, C. Krause, T. L. Hudson, S. Piqueux, N. Müller, M. Golombek, C. Vrettos, E. Marteau, S. Nagihara, P. Morgan, J. P. Murphy, m. Siegler, S. D. King, S. E. Smrekar, and W. B. Banerdt. Thermal conductivity of the Martian soil at the InSight landing site From HP3 active heating experiments. *J. Geophys. Res. Planets*, 126, 2021. doi:https://doi.org/10.1029/2021JE006861.

[26] M. Grott, S. Piquex, T. Spohn, J. Knollenberg, C. Krause, T. L. Hudson, F. Forget, L. Lange, N. Müller, M. Golombek, S. Nagihara, P. Morgan, J. P. Murphy, m. Siegler, S. D. ing, D. Banfield, S. E. Smrekar, and W. B. Banerdt. Seasonal variations of soil thermal conductivity at the InSight landing site. *Geophys. Res. Lett.*, 50, 2023. doi:https://doi.org/10.1029/2023GL102975.

[27] B. H. Hager, R. W. Clayton, M. A. Richards, R. P. Comer, and A. M. Dziewoński. Lower mantle heterogeneity, dynamic topography and the geoid. *Nature*, 313:541–545, 1985.

[28] H. Harder. Phase transitions and the three-dimensional planform of thermal convection in the Martian mantle. *Journal of Geophysical Research: Planets*, 103(E7):16775–16797, July 1998. doi:https://doi.org/10.1029/98je01543.

[29] H. Harder. Mantle convection and the dynamic geoid of Mars. *Geophys. Res. Lett.*, 27 (3):301–304, 2000. doi:https://doi.org/10.1029/2022JE007298.

[30] H. Harer and U. R. Christensen. A one-plume model of Martian mantle convection. *Nature*, 380:507–509, 1996.

[31] T. Heister, J. Dannberg, R. Gassmöller, and W. Bangerth. High accuracy mantle convection simulation through modern numerical methods – II: realistic models and problems. *Geophysical Journal International*, 210(2):833–851, May 2017. doi:https://doi.org/10.1093/gji/ggx195.

[32] H. Hiesinger and J. W. Head III. The Syrtis Major volcanic province, Mars: Synthesis from Mars global surveyor data. *Journal of Geophysical Research: Planets*, 109(E1), 2004. doi:https://doi.org/10.1029/2003JE002143.

[33] D. G. Horvath, P. Moitra, C. W. Hamilton, R. A. Craddock, and J. C. Andrews-Hanna. Evidence for geologically recent explosive volcanism in Elysium Planitia, Mars. *Icarus*, 365, 2021. doi:https://doi.org/10.1016/j.icarus.2021.114499.

[34] Q. Huang, N. C. Schmerr, S. D. King, D. Kim, A. Rivoldini, A.-C. Plesa, H. Samuel, R. R. Maguire, F. Karakostas, V. Lekić, et al. Seismic detection of a deep mantle discontinuity within Mars by InSight. *Proc. Natl. Acad. Sci. U.S.A.*, 119(42), 2022. doi:https://doi.org/10.1073/pnas.2204474119.

[35] J. C. E. Irving, V. Lekić, C. Durán, M. Drilleau, D. Kim, A. Rivoldini, A. Khan, H. Samuel, D. Antonangeli, W. B. Banerdt, C. Beghein, E. Bozdağ, S. Ceylan,

C. Charalambous, J. Clinton, P. Davis, R. Garcia, D. Giardini, A. C. Horleston, Q. Huang, K. J. Hurst, T. Kawamura, S. D. King, M. Knapmeyer, J. Li, P. Lognonné, R. Maguire, M. P. Panning, A.-C. Plesa, M. Schimmel, N. C. Schmerr, S. C. Stähler, E. Stutzmann, and Z. Xu. First observations of core-transiting seismic phases on Mars. *Proceedings of the National Academy of Sciences*, 120(18), 2023. doi:https://doi.org/10.1073/pnas.2217090120.

[36] W. L. Jaeger, L. P. Keszthelyi, J. A. Skinner Jr., M. P. Milazzo, A. S. McEwen, T. N. Titus, M. R. Rosiek, D. M. Galuszka, E. Howington-Kraus, R. L. Kirk, et al. Emplacement of the youngest flood lava on Mars: A short, turbulent story. *Icarus*, 205(1):230–243, 2010. doi:https://doi.org/10.1016/j.icarus.2009.09.011.

[37] P. Janle and E. Erkul. Gravity studies of the Tharsis area on Mars. *Earth, Moon, Planets*, 53:217–232, 1990. doi:https://doi.org/10.1007/BF00055948.

[38] R. F. Katz, M. Spiegelman, and C. H. Langmuir. A new parameterization of hydrous mantle melting. *Geochemistry, Geophysics, Geosystems*, 4(9), 2003. doi:https://doi.org/10.1029/2002GC000433.

[39] L. H. Kellogg and S. D. King. The effect of temperature dependent viscosity on the structure of new plumes in the mantle: Results of a finite element model in a spherical, axisymmetric shell. *Earth and Planetary Science Letters*, 148(1-2):13–26, April 1997. doi:https://doi.org/10.1016/s0012-821x(97)00025-3.

[40] A. Khan, S. Ceylan, M. van Driel, D. Giardini, P. Lognonné, H. Samuel, N. C. Schmerr, S. C. Stähler, A. C. Duran, Q. Huang, et al. Upper mantle structure of Mars from InSight seismic data. *Science*, 373(6553):434–438, 2021. doi:https://doi.org/10.1126/science.abf2966.

[41] W. S. Kiefer. Melting in the martian mantle: Shergottite formation and implications for present-day mantle convection on Mars. *Meteorit. Planet. Sci.*, 39(12):1815–1832, 2003.

[42] W. S. Kiefer. Forming the martian great divide. *Nature*, 453:1191–1192, 2008. doi:https://doi.org/10.1038/4531191a.

[43] W. S. Kiefer and Q. Li. Water undersaturated mantle plume volcanism on present-day Mars. *Meteorit. Planet. Sci.*, 51(11), 2016. doi:https://doi.org/10.1111/maps.12720.

[44] W. S. Kiefer, M. B. Weller, M. S. Duncan, and J. Filiberto. Mantle plume magmatism in Elysium Planitia as constrained by InSight seismic observations. In *Lunar and Planetary Science Conference*, number 2341 in 54, The Woodlands, TX, USA, March 2023.

[45] S. D. King. Pattern of lobate scarps on Mercury's surface reproduced by a model of mantle convection. *Nature Geoscience*, 1(4):229–232, 2008. doi:https://doi.org/10.1038/ngeo152.

[46] S. D. King, A. R., and B. H. Hager. Conman: vectorizing a finite element code for incompressible two-dimensional convection in the Earth's mantle. *Physics of the Earth and Planetary Interiors*, 59(3):195–207, 1990. doi:https://doi.org/10.1016/0031-9201(90)90225-m.

[47] S. D. King, C. Lee, P. E. van Keken, W. Leng, S. Zhong, E. Tan, N. Tosi, and M. C. Kameyama. A community benchmark for 2-D Cartesian compressible convection in the Earth's mantle. *Geophysical Journal International*, 180(1):73–87, 2010. doi:https://doi.org/10.1111/j.1365-246x.2009.04413.x.

[48] S.D. King and H.L. Redmond. The crustal dichotomy and edge-driven convection: A mechanism for Tharsis Rise volcanism. In *Lunar and Planetary Science Conference*, number 1960 in XXXVI, The Woodlands, TX, USA, March 2005. URL https://www.lpi.usra.edu/meetings/lpsc2005/pdf/1960.pdf.

[49] B. Knapmeyer-Endrun, M. P. Panning, F. Bissig, R. Joshi, A. Khan, D. Kim, V. Lekić, B. Tauzin, S. Tharimena, M. Plasman, et al. Thickness and structure of the martian crust from insight seismic data. *Science*, 373(6553):438–443, 2021. doi:https://doi.org/10.1126/science.abf8966.

[50] M. Kronbichler, T. Heister, and W. Bangerth. High accuracy mantle convection simulation through modern numerical methods. *Geophysical Journal International*, 191 (1):12–29, August 2012. doi:https://doi.org/10.1111/j.1365-246x.2012.05609.x.

[51] I. Lehman. P'. *Bureau Central Séismologique International Strasbourg: Publications du Bureau Central Scientifiques*, 14:87–115, 1936.

[52] R. D. Lehman. The Constitution of the Interior of the Earth as Revealed by Earthquakes. *Quarterly Journal of the Geological Society of London*, 62:456–472, 1906.

[53] Q. Li and W. S. Kiefer. Mantle convection and magma production on present-day Mars: Effects of temperature-dependent rheology. *Geophys. Res. Lett.*, 34(L16203), 2007. doi:https://doi.org/10.1029/2007GL030544.

[54] Michael C. Malin. Comparison of volcanic features of Elysium (Mars) and Tibesti (Earth). *GSA Bulletin*, 88(7):908–919, 1977. doi:https://doi.org/10.1130/0016-7606(1977)88<908:COVFOE>2.0.CO;2.

[55] M. M. Marinova, O. Aharonson, and E. Asphaug. Mega-impact formation of the Mars hemispheric dichotomy. *Nature*, 119:1216–1219, 2008. doi:https://doi.org/10.1038/nature07070.

[56] K. N. Matsukage, Y. Nagayo, M. L. Whittaker, E. Takahashi, and T. Kawasaki. Melting of the Martian mantle from 1.0 to 4.5 GPa. *Journal of Mineralogical and Petrological Sciences*, 108:201–214, 2013. doi:https://doi.org/10.2465/jmps.120820.

[57] D. McKenzie and M. J. Bickle. The Volume and Composition of Melt Generated by Extension of the Lithosphere. *Journal of Petrology*, 29(3):625–679, 1988. doi:https://doi.org/10.1093/petrology/29.3.625.

[58] S. M. McLennan. Crustal heat production and the thermal evolution of mars. *Geophysical Research Letters*, 28(21):4019–4022, 2001. doi:https://doi.org/10.1029/2001gl013743.

[59] A. Mittelholz, C. L. Johnson, J. M. Feinberg, B. Langlais, and R. J. Phillips. Timing of the martian dynamo: New constraints for a core field 4.5 and 3.7 Ga ago. *Science Advances*, 6(18), 2020. doi:https://doi.org/10.1126/sciadv.aba0513.

[60] A. Mohorovičić. Potres od 8. X. 1909 [Earthquake of 8 October 1909]. *Godišnje izvješče Zagrebačkog Meteorološkog Opservatorija: za godinu 1909 [Annual report of the Zagreb Meteorological Observatory: for the year 1909]*, pages 1–56, 1909.

[61] P. Mouginis-Mark, J. Zimbelman, D. Crown, L. Wilson, and T. Gregg. Martian volcanism: Current state of knowledge and known unknowns. *Geochemistry*, 82, 2022. doi:https://doi.org/10.1016/j.chemer.2022.125886.

[62] E. Mulyukova and D. Bercovici. Mantle convection in terrestrial planets. 2020. doi:https://doi.org/10.1093/acrefore/9780190647926.013.109.

[63] G. Neukum, R. Jaumann, H. Hoffmann, E. Hauber, J.W. Head, Basilevsky A.T., B.A. Ivanov, S.C. Werner, S. van Gasselt, J.B. Murray, and the HRSC Investigator Team. Recent and episodic volcanic and glacial activity on Mars revealed by the High Resolution Stereo Camera. *Nature*, 432:971–979, 2004. doi:https://doi.org/10.1038/nature03231.

[64] G.A. Neumann, M.T. Zuber, M.A. Wieczorek, P.J. McGovern, F.G. Lemoine, and D.E. Smith. Crustal structure of Mars from gravity and topography. *J. Geophys. Res.*, 109(E08002), 2004. doi:https://doi.org/10.1029/2004JE002262.

[65] F. Nimmo and D. J. Stevenson. Influence of early plate tectonics on the thermal evolution and magnetic field of Mars. *Journal of Geophysical Research: Planets*, 105 (E5):11969–11979, 2000. doi:https://doi.org/10.1029/1999je001216.

[66] E. A. Ninju, D. S. Stamps, K. Neumiller, and J. Gallager. Lithospheric control of melt generation beneath the rungwe volcanic province, east africa: Implications for a plume source. *J. Geophys. Res. Planets*, 126(e2020JB020728), 2021. doi:https://doi.org/10.1029/2020JB020728.

[67] E. A. Ninju, D. S. Stamps, E. A. Atekwana, T. O. Rooney, and T. A. Rajaonarison. Instantaneous 3d tomography-based convection beneath the rungwe volcanic province, east africa: implications for melt generation. *Geophysical Journal International*, 235 (1), 2023. doi:https://doi.org/10.1093/gji/ggad219.

[68] C. Perrin, A. Jacob, A. Lucas, R. Myhill, E. Hauber, A. Batov, T. Gudkova, S. Rodriguez, P. Lognonné, J. Stevanović, M. Drilleau, and N. Fuji. Geometry and Segmentation of Cerberus Fossae, Mars: Implications for Marsquake Properties. *Journal of Geophysical Research: Planets*, 127(1), 2022. doi:https://doi.org/10.1029/2021je007118.

[69] R.J. Phillips, M.T. Zuber, S.C. Solomon, M.P. Golombek, B.M. Jakosky, W.B. Banerdt, D.E. Smith, R.M.E. Williams, B.M. Hynek, O. Aharonson, and S.A. Hauck II. Ancient geodynamics and global-scale hydrology on Mars. *Science*, 291:2587–2591, 2001. doi:https://doi.org/10.1126/science.1058701.

[70] T. Platz, G. G. Michael, and G. Neukum. Confident thickness estimates for planetary surface deposits from concealed crater populations. *Earth and Planet. Sci. Lett.*, 293: 388–395, 2010. doi:https://doi.org/10.1016/j.epsl.2010.03.012.

[71] A.-C. Plesa, N. Tosi, M. Grott, , and D. Breuer. Thermal evolution and Urey ratio of Mars. *J. Gephys. Res. Planets*, 120:995–1010, 2015. doi:https://doi.org/10.1002/2014JE004748.

[72] A.-C. Plesa, M. Grott, N. Tosi, D. Breuer, T. Spohn, and M.A. Wieczorek. How large are present-day heat flux variations across the surface of Mars? *J. Gephys. Res. Planets*, 121:2386–2403, 2016. doi:https://doi:10.1002/2016JE005126.

[73] A.-C. Plesa, M. Knapmeyer, M.P. Golombek, D. Breuer, M. Grott, T. Kawamura, P. Lognonne, N. Tosi, and R.C. Weber. Present-day Mars' seismicity predicted From 3-D thermal evolution models of interior dynamics. *Geophys. Res. Lett.*, 45:2580–2589, 2018. doi:https://doi.org/10.1002/2017GL076124.

[74] J.A. Richardson, J.A. Wilson, C.B. Connor, J.E. Bleacher, and K. Kiyosugi. Recurrence rate and magma effusion rate for the latest volcanism on Arsia Mons, Mars. *Earth Planet. Sci. Lett.*, 458:170–178, 2017. doi:https://doi.org/10.1016/j.epsl.2016.10.040.

[75] J. H. Roberts and S. Zhong. Plume-induced topography and geoid anomalies and their implications for the Tharsis rise on Mars. *J. Geophys. Res. Planets*, 109(E03009), 2004. doi:https://doi.org/10.1029/2003JE002226.

[76] J. H. Roberts and S. Zhong. Degree-1 convection in the Martian mantle and the origin of the hemispheric dichotomy. *J. Geophys. Res. Planets*, 111(E06013), 2006. doi:https://doi.org/10.1029/2005JE002668.

[77] J. H. Roberts and S. Zhong. The cause for the north–south orientation of the crustal dichotomy and the equatorial location of Tharsis on Mars. *Icarus*, 190(1):24–31, September 2007. doi:https://doi.org/10.1016/j.icarus.2007.03.002.

[78] T. Ruedas, P. J. Tackley, and S. C. Solomon. Thermal and compositional evolution of the martian mantle: Effects of water. *Physics of the Earth and Planetary Interiors*, 220:50–72, 2013. doi:https://doi.org/10.1016/j.pepi.2013.04.006.

[79] H. Samuel, M. D. Ballmer, S. Padovan, N. Tosi, A. Rivoldini, and A.-C. Plesa. The thermo-chemical evolution of Mars with a strongly stratified mantle. *J. Geophys. Res. Planets*, 126, 2021. doi:https://doi.org/10.1029/2020JE006613.

[80] P. Sekhar and S. D. King. 3D spherical models of Martian mantle convection constrained by melting history. *Earth Planet. Sci. Lett.*, 388:27–37, 2014. doi:https://doi.org/10.1016/j.epsl.2013.11.047.

[81] S. E. Smrekar, P. Lognonné, T. Spohn, W. B. Banerdt, D. Breuer, et al. Pre-mission InSights on the Interior of Mars. *Space Science Reviews*, 215(1):1–72, 2019. doi:https://doi.org/10.1007/s11214-018-0563-9.

[82] T. Spohn, M. Grott, S. E. Smrekar, J. Knollenberg, T. L. Hudson, C. Krause, N. Müller, J. Jänchen, A. Börner, T. Wipperman, O. Krömer, R. Lichtenheldt, L. Wisniewski, M. Grygorczuk, J. Fittock, S. Rheershemius, T. Spröwitz, E. Kopp, I. Walter, A. C. Plesa, D. Breuer, P. Morgan, and W. B. Banerdt. The Heat Flow and Physical Properties Package (HP^3) for the InSight mission. *Space Sci. Rev.*, 214, 2018. doi:https://doi.org/10.1007/s11214-018-0531-4.

[83] T. Spohn, T. L. Hudson, L. Witte, T. Wippermann, L. Wisniewski, B. Kedziora, C. Vrettos, R. D. Lorenz, M. Golombek, R. Lichtenheldt, M. Grott, J. Knollenberg, C. Krause, C. Fantinati, S. Nagihara, and J. Grygorczuk. The InSight-HP3 mole on Mars: Lessons learned from attempts to penetrate to depth in the martian soil. *Advances in Space Research*, 69, 2022. doi:https://doi.org/10.1016/j.asr.2022.02.009.

[84] T. Spohn, T.L. Hudson, E. Marteau, M. Golombek, M. Grott, T. Wippermann, K.S. Ali, C. Schmelzbach, S. Kedar, A. Hurst, K. amd Trebi-Ollennu, V. Ansan, J. Garvin, J. Knollenberg, N. Müller, S. Piqueux, R. Lichtenheldt, C. Krause, C. Fantinati, N. Brinkman, D. Sollberger, P. Delage, C. Vrettos, S. Reershemius, L. Wisniewski, J. Grygorczuk, J. Robertsson, P. Edme, F. Andersson, O. Krömer, D. Lognonné, Giardini, S.E. Smrekar, and W.B. Banerdt. The InSight HP3 penetrator (mole) on Mars: Soil properties derived from the penetration attempts and related activities. *Space Sci. Rev.*, 218(72), 2022. doi:https://doi.org/10.1007/s11214-022-00941-z.

[85] O. Šrámek and S. Zhong. Martian crustal dichotomy and Tharsis formation by partial melting coupled to early plume migration. *Journal of Geophysical Research: Planets*, 117(E1), 2012. doi:https://doi.org/10.1029/2011JE003867.

[86] S. C. Stähler, A. Khan, W. B. Banerdt, P. Lognonné, D. Giardini, S. Ceylan, M. Drilleau, A. C. Duran, R. F. Garcia, Q. Huang, et al. Seismic detection of the martian core. *Science*, 373(6553):443–448, 2021. doi:https://doi.org/10.1126/science.abi7730.

[87] S. C. Stähler, A. Mittelholz, C. Perrin, T. Kawamura, D. Kim, M. Knapmeyer, G. Zenhäusern, J. Clinton, D. Giardini, P. Lognonné, and W. B. Banerdt. Tectonics of Cerberus Fossae unveiled by marsquakes. *Nature Astronomy*, 6(12):1376–1386, 2022. doi:https://doi.org/10.1038/s41550-022-01803-y.

[88] S. C Stähler, A. Mittelholz, C. Perrin, T. Kawamura, D. Kim, M. Knapmeyer, G. Zenhäusern, J. Clinton, D. Giardini, P. Lognonné, et al. Tectonics of Cerberus Fossae unveiled by marsquakes. *Nature Astronomy*, 6(12):1376–1386, 2022. doi:https://doi.org/10.1038/s41550-022-01803-y.

[89] D. J. Stevenson, T. Spohn, and G. Schubert. Magnetism and thermal evolution of the terrestrial planets. *Icarus*, 54(3):466–489, 1983. doi:https://doi.org/10.1016/0019-1035(83)90241-5.

[90] D. Susko, S. Karunatillake, G. Kodikara, J. R. Skok, J. Wray, J. Heldmann, A. Cousin, and T. Judice. A record of igneous evolution in Elysium, a major martian volcanic province. *Scientific Reports*, 7(1), 2017. doi:https://doi.org/10.1038/srep43177.

[91] P. J. Tackley. Modelling compressible mantle convection with large viscosity contrasts in a three-dimensional spherical shell using the yin-yang grid. *Physics of the Earth and Planetary Interiors*, 171(1-4):7–18, 2008. doi:https://doi.org/10.1016/j.pepi.2008.08.005.

[92] E. Takahashi. Melting of a dry peridotite KLB-1 up to 14 GPa: Implications on the origin of peridotitic upper mantle. *Journal of Geophysical Research*, 91(B9):9367, 1986. doi:https://doi.org/10.1029/JB091iB09p09367.

[93] E. Tan, E. Choi, P. Thoutireddy, M. Gurnis, and M. Aivazis. GeoFramework: Coupling multiple models of mantle convection within a computational framework. *Geochem. Geophys. Geosyst.*, 7(Q06001), 2006. doi:https://doi.org/10.1029/2005GC001155.

[94] G. J. Taylor, W. Boynton, J. Brückner, H. Wänke, G. Dreibus, K. Kerry, J. Keller, R. Reedy, L. Evans, R. Starr, S. Squyres, S. Karunatillake, O. Gasnault, S. Maurice, C. d'Uston, P. Englert, J. Dohm, V. Baker, D. Hamara, D. Janes, A. Sprague,

K. Kim, and D. Drake. Bulk composition and early differentiation of mars. *Journal of Geophysical Research*, 112(E3), 2006. doi:https://doi.org/10.1029/2005je002645.

[95] N. Tosi, A.-C. Plesa, and D. Breuer. Overturn and evolution of a crystallized magma ocean: A numerical parameter study for Mars. *J. Geophys. Res. Planets*, 118:1512–1528, 2013. doi:https://doi.org/10.1002/jgre.20109.

[96] A. H. Treiman, J. D. Gleason, and D. D. Bogard. The SNC meteorites are from Mars. *Planetary and Space Science*, 48:1213–1230, 2000. doi:https://doi.org/10.1016/S0032-0633(00)00105-7.

[97] D. L. Turcotte and G. Schubert. *Geodynamics*. Cambridge University Press, Cambridge, UK, 2014. doi:https://doi.org/10.1017/CBO9780511843877.

[98] O. Srámek and S. Zhong. Martian crustal dichotomy and Tharsis formation by partial melting coupled to early plume migration. *J. Geophys. Res.*, 117(E01005), 2012. doi:https://doi.org/10.1029/2011JE003867.

[99] P. van Thienen, A. Rivoldini, T. Van Hoolst, and P. Lognonné. A top-down origin for martian mantle plumes. *Icarus*, 2006. doi:https://doi:10.1016/j.icarus.2006.06.008.

[100] J. Vaucher, D. Baratoux, N. Mangold, P. Pinet, K. Kurita, and M. Grégoire. The volcanic history of central Elysium Planitia: Implications for martian magmatism. *Icarus*, 204(2):418–442, 2009. doi:https://doi.org/10.1016/j.icarus.2009.06.032.

[101] S. Watson and D. McKenzie. Melt generation by plumes: a study of Hawaiian volcanism. *Journal of Petrology*, 32(3):501–537, 1991. doi:https://doi.org/10.1093/petrology/32.3.501.

[102] T.R. Watters and G.S. Schubert. Hemispheres apart: The crustal dichotomy on Mars. *Annu. Rev. Earth Planet. Sci.*, 35:621–652, 2007. doi:https://doi:10.1146/annurev.earth.35.031306.140220.

[103] M. J. Wenzel, M. Manga, and A. M. Jellinek. Tharsis as a consequence of Mars' dichotomy and layered mantle. *Geophys. Res. Lett.*, 31(L04702), 2004. doi:https://doi.org/10.1029/2003GL019306.

[104] M. A. Wieczorek, A. Broquet, S. M. McLennan, A. Rivoldini, M. Golombek, D. Antonangeli, C. Beghein, D. Giardini, T. Gudkova, S. Gyalay, et al. InSight constraints on the global character of the Martian crust. *J. Geophys. Res. Planets*, 127, 2022. doi:https://doi.org/10.1029/2022JE007298.

[105] J. Yan, M. D. Ballmer, and P. J. Tackley. The evolution and distribution of recycled oceanic crust in the Earth's mantle: Insight from geodynamic models. *Earth and Planetary Science Letters*, 537, 2020. doi:https://doi.org/10.1016/j.epsl.2020.116171.

[106] S. Zhong. Migration of Tharsis volcanism on Mars caused by differential rotation of the lithosphere. *Nature Geoscience*, 2:19–23, 2009. doi:https://doi.org/10.1038/NGEO392.

[107] S. Zhong and M. T Zuber. Degree-1 mantle convection and the crustal dichotomy on Mars. *Earth and Planetary Science Letters*, 189(1-2):75–84, June 2001. doi:https://doi.org/10.1016/s0012-821x(01)00345-4.

[108] S. Zhong, M. T. Zuber, L. Moresi, and M. Gurnis. Role of temperature-dependent viscosity and surface plates in spherical shell models of mantle convection. *J. Geophys. Res.*, 105(B5):11,063–11,082, 2000. doi:https://doi.org/10.1111/maps.12720.

[109] S. Zhong, A. McNamara, E. Tan, L. Moresi, and M. Gurnis. A benchmark study on mantle convection in a 3-D spherical shell using CitcomS. *Geochem. Geophys. Geosyst.*, 9(10), 2008. doi:https://doi.org/10.1029/2008GC002048.

[110] M.T. Zuber and D.E. Smith. Mars without Tharsis. *J. Geophys. Res.*, 102(E12): 28,673–28,685, 1997. doi:https://doi.org/10.1029/97JE02527.

[111] M.T. Zuber, S.C. Solomon, R.J. Phillips, D.E. Smith, G.L. Tyler, O. Aharonson, G. Balmino, W.B. Banerdt, J.W. Head, C.L. Johnson, F.G. Lemoine, P.J. McGovern, G.A. Neumann, D.D. Rowlands, and S. Zhong. Internal structure and early thermal evolution of Mars from Mars Global Surveyor topography and gravity. *Science*, 287 (1788), 2000. doi:https://doi.org/10.1126/science.287.5459.1788.